DISSERTATION

THEORY AND MITIGATION OF ELECTRON BACK-BOMBARDMENT IN THERMIONIC CATHODE RADIO FREQUENCY GUNS

Submitted by

Jonathan Paul Edelen

Department of Electrical and Computer Engineering

In partial fulfillment of the requirements

For the Degree of Doctor of Philosophy

Colorado State University

Fort Collins, Colorado

Summer 2015

Doctoral Committee:

Advisor: Stephen Milton
Co-Advisor: Sandra Biedron

Branislav Notaros
Thomas Johnson

ABSTRACT

THEORY AND MITIGATION OF ELECTRON BACK-BOMBARDMENT IN THERMIONIC CATHODE RADIO FREQUENCY GUNS

Photocathode RF guns are currently the standard for high- power, low-emittance beam generation in free-electron lasers. These devices require the use of high-power lasers (which are bulky and expensive to operate) and high-quantum-efficiency cathodes (which have limited lifetimes requiring frequent replacement). The use of RF-gated thermionic cathodes enables operation without a large drive laser and with long lifetimes. One major limitation of RF-gated thermionic cathodes is that electrons emitted late in the RF period will not gain enough energy to exit the gun before being accelerated back towards the cathode by the change in sign of the RF field. These electrons deposit their kinetic energy on the cathode surface in the form of heat, limiting the ability to control the output current from the cathode. This dissertation is aimed at understanding the fundamental design factors that drive the back-bombardment process and at exploring novel techniques to reduce its impact on a high-current system. This begins with the development of analytic models that predict the back-bombardment process in single-cell guns. These models are compared with simulation and with a measurement taken at a specific facility. This is followed by the development of analytic models that predict the effects of space-charge on back-bombardment. These models are compared with simulations. This is followed by an analysis of how the addition of multiple cells will impact the back-bombardment process. Finally, a two-frequency gun is studied for its ability to mitigate the back-bombardment process. This dissertation provides new insight on how the back-bombardment process scales as a

function of the beam parameters and how space-charge affects this process. Additionally this dissertation shows how a second frequency can be used to mitigate the back-bombardment effect.

ACKNOWLEDGEMENTS

It is pure happenstance that brought me to the Accelerator Physics program being developed at CSU. This opportunity has opened doors for me that wouldn't have been otherwise available and has given me the chance to grow as a researcher. I want to thank Sandra Biedron and Stephen Milton for providing me with this opportunity.

I also want to thank John Harris and John Lewellen for your continued support and detailed technical feedback on my work throughout my time at CSU. I look forward to many years of continued collaboration on gun design and beam dynamics. I also want to thank Bruce Carlsten for the exchange of ideas and, perhaps even more importantly, for helping me to decode the nuances of PARMELA.

I would like to give a special thanks to all of my friends and family for their support, especially my parents Bonnie and Paul, my brother Mike, Jesse and Carol Parker, Chris Hall, and many more that are far too numerous to mention here.

Finally, I want to give a very heartfelt thanks to my wife, Auralee. Throughout my graduate education you have helped me grow as an individual and as a researcher. From helping me with my writing to attempting to train an engineer in modern physics, your assistance has been invaluable. Perhaps most of all, I am deeply grateful for the emotional support that you have given me throughout my time at CSU. There is no doubt that without your help I would not have had the same experience with graduate school.

TABLE OF CONTENTS

ABSTRACT II

ACKNOWLEDGEMENTS IV

1. INTRODUCTION 1
1.1 BACKGROUND 3
1.2 OVERVIEW OF WORK 6

2. BACK-BOMBARDMENT IN SINGLE-CELL GUNS 10
2.1 SIMULATION STUDIES OF A SHORT GAP GUN 10
2.2 A FIRST PRINCIPLES ANALYSIS OF SINGLE-CELL GUNS 17
2.2.1 Derivation of the analytic model 17
2.2.2 Comparison with simulations 23
2.3 REFINEMENT OF THE CONSTANT VELOCITY ASSUMPTION 26
2.3.1 Derivation of the model with arbitrary constant velocity 26
2.3.2 Calculating the effective velocity 28
2.3.3 Comparison with simulations 31
2.4 REFINEMENT OF THE TEMPORAL FIELD PROFILE 33
2.4.1 Sinusoidal analysis with speed of light velocity 34
2.4.2 Analysis of sinusoidal field with arbitrary constant velocity 38
2.5 COMPARISON ANALYSIS OF MODELS 43
2.5.1 Comparison of back-bombardment prediction 43
2.5.2 Comparison of time domain prediction 47
2.5.3 Comparison to measurement 51

3. SPACE-CHARGE EFFECTS ON BACK-BOMBARDMENT IN SINGLE-CELL GUNS 53
3.1 SIMULATION OF SPACE-CHARGE EFFECTS IN A SHORT GAP GUN 53
3.2 A MODEL FOR SPACE-CHARGE BEHAVIOR 63
3.2.1 Longitudinal space-charge effects 63
3.2.2 Transverse space-charge effects 65
3.2.3 Space-charge effects on back-bombardment 68
3.3 COMPARISON WITH SIMULATIONS 71

4. BACK-BOMBARDMENT IN MULTI-CELL GUNS 74
4.1 BACK-BOMBARDMENT POWER IN N-CELL, ZERO-MODE GUNS 75
4.1.1 Heuristic discussion of back-bombardment in zero-mode guns 75
4.1.2 1-D simulations of back-bombardment in n-cell zero-mode guns 76
4.1.3 2.5-D simulations of back-bombardment in n-cell zero-mode guns 81
4.2 BACK-BOMBARDMENT POWER IN N-CELL PI-MODE GUNS 83
4.2.1 1-D Simulations of back-bombardment in n-cell pi-mode guns 83
4.2.2 2.5-D simulations of back-bombardment in n-cell pi-mode guns 86
4.3 BACK-BOMBARDMENT IN INDEPENDENTLY PHASED 2-CELL GUNS 87
4.3.1 1-D Simulations of back-bombardment in 2-cell guns 88

5. A BACK-BOMBARDMENT MITIGATION TECHNIQUE 97
5.1 TWO-FREQUENCY GUN FOR BACK-BOMBARDMENT MITIGATION 97

5.2 BACK-BOMBARDMENT MITIGATION SIMULATIONS 106
6. CONCLUSIONS 110
REFERENCES 114

1. Introduction

High-average-power free-electron laser (FEL) facilities for the science and engineering community require the production of high-average-current, low-emittance, electron beams. FLASH [1] and the European XFEL [2] use superconducting linear accelerators to provide flexibility in the temporal pulse structure, allowing for high repetition-rate micro-pulses in a 1-ms macro-pulse at 50 Hz. However, these systems do not provide true CW MHz operation. The use of superconducting accelerators at The LCLS-II at SLAC [3] aims at developing a FEL with a repetition rate of nearly 1 MHz. Such a light source fills the gap between storage ring sources with 1 ns pulse separation, 1 nJ energy per pulse, and X-ray laser with ms pulse separation and 1 mJ energy per pulse. The LUNEX5 project (free electron Laser Using a New accelerator for the Exploitation of X-ray radiation of 5th generation) [4] working towards a similar aim as LCLS-II but at a smaller scale, uses superconducting accelerators and solid-state modulators to achieve a high duty cycle and eventually will be upgraded to full CW operation.

Beams for these facilities are predominately created by photocathode radio frequency (RF) guns. Unfortunately, photocathode RF guns require high-average-power drive lasers, which tend to be large, expensive, and operationally labor intensive. Additionally, these guns require the use of high-quantum-efficiency cathodes that typically have a limited lifetime (hours to days) and require frequent replacement and/or rejuvenation [5, 6]. These issues could be avoided by using thermionic cathodes that are robust and long-lived [7]. The current emitted from a thermionic cathode depends on its temperature, which cannot be rapidly changed due to the cathode's finite thermal mass. Therefore, emission from these cathodes is often gated using a control grid [8, 9, 10]. However, these grids tend to degrade the transverse beam emittance especially at high

current, and furthermore they cannot be gated at picosecond timescales. Techniques for laser gating where a laser pulse is used to heat the surface of the cathode and produce thermionic emission have also been investigated [11, 12]. For high current this technique becomes impractical, as the surface cooling time of the cathode will be longer than that of a single RF period. There are regimes where a un-gridded thermionic cathode RF gun system can be used. In these cases gating of the beam is directly accomplished by the RF field in the gun, and emission will occur when there is not a surface field preventing it, corresponding to half of the RF period. One down side to this approach is that the beam often requires further compression, for instance by an alpha magnet, before being injected into the accelerator [13], and this potentially has significant impact on the beam emittance. The use of un-gated thermionic cathodes does, however, allow for the unobstructed increase in beam current without degradation of the transverse emittance from control grids, without the use of high power drive lasers, and with consistent reliable emission from long-lasting thermionic emitters.

A major problem with thermionic sources in rf guns is back-bombardment. Some electrons that are emitted late relative to the RF phase will not gain enough energy to leave the cavity, and when the electric field reverses they will be decelerated and then accelerated back towards the cathode. These electrons deposit their kinetic energy onto the cathode surface in the form of heat. Figure 1 shows conceptually how this process occurs.

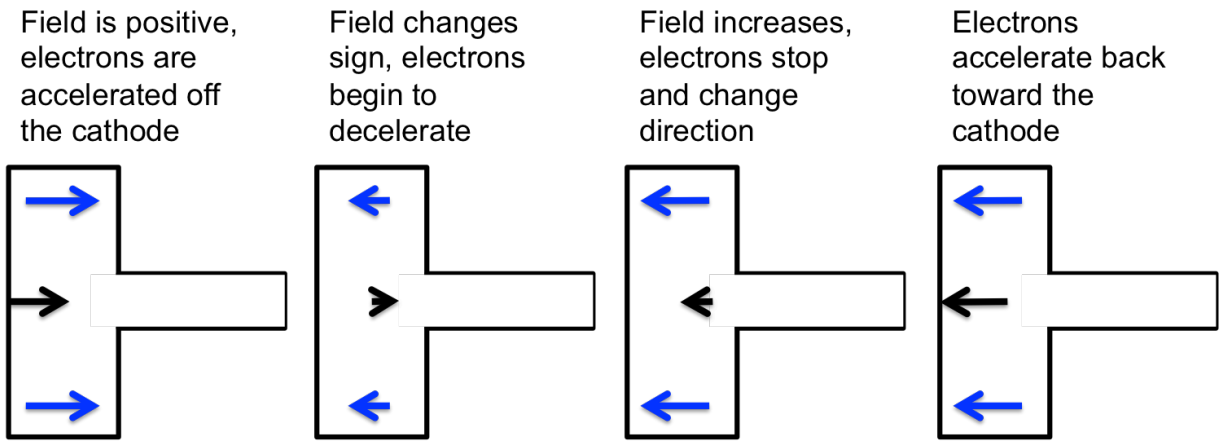

Figure 1: Conceptual diagram of the back-bombardment process. The RF fields are given in blue and the beam path is given in black

Such back-bombardment is undesirable because it introduces an additional source term to the cathode temperature that can negatively affect the ability to regulate the cathode emission [14, 15, 16]. This typically results in a steady increase in the beam current on the macro-pulse, and additionally the transient beam-loading effect of the back-bombarded beam results in energy spread issues over the macro-pulse [17, 18, 19]. These effects have serious implications for machine performance. Furthermore, it is possible for the cathode to enter a run-away condition where the back-bombarded power increases the temperature until either the cathode is damaged or the interlock systems are triggered; therefore, it is desirable to understand what fundamental factors govern the back-bombardment process and what methods can be used to mitigate this effect while still operating an un-gated thermionic RF gun.

1.1 Background

In general there is a significant gap in the engineering understanding of the back-bombardment process. Here engineering understanding describes the ability to show, quantitatively which design parameters will either increase or decrease the back-bombardment power. This allows the gun parameters to be optimized based on a set of operating parameters before running particle

beam simulations or introducing back-bombardment mitigation techniques. Additionally, an analytical model of the back-bombardment can be used to predict the temperature increase of the cathode surface and thus determine the contribution to the emission current. Analytical models are also helpful in studying novel techniques for back-bombardment mitigation without the need for multi-particle simulation as these tend to be iterative and could be computationally intensive for large optimization problems.

Work has been done by C.B. McKee et al. [14] to simulate how much cathode heating occurs due to back-bombardment for a particular gun design, and similar studies have been done experimentally to indirectly measure the cathode heating and apply different cathode configurations to reduce this heating [15,16]. As mentioned previously, some work has also been done to evaluate the impact of transient beam-loading due to the back-bombarded beam [17], and how to compensate the resulting energy spread through cavity detuning [18]. These efforts all analyze what happens as a result of the back-bombarded beam and some initial mitigation techniques, but they don't assess from a design standpoint how the gun variables can be used to reduce the base-line level of back-bombardment, nor do they make theoretical predictions on the cathode temperature increase or the ability to mitigate the back-bombardment process. Some work has been done in simulation to characterize the back-bombardment as a function of gun parameters [20], but it does not provide a well-defined theory or exact scaling laws for this process.

The most common mitigation technique employs a magnetic dipole across the cathode that is used to deflect the backward propagating beam away from the cathode surface [21, 15, 16, 22,

23, 24, 25, 26, 27, 28]. This technique does work relatively well; however, it provides complications for the output beam if the magnet cannot be switched on and off fast enough. In another configuration the use of a ring cathode instead of a traditional solid cathode reduces the area that sees back-bombarded particles and consequently reduces the thermal impact on the cathode [21]. In multi-cell guns, reducing the length of the second cell can reduce the energy of electrons that are back-bombarded from this cell. While this does not have any impact on particles that don't make it out of the first cell, structures such as a ½+½ +1 cell rf gun, can be tuned to have less back-bombardment power than the comparable 2½ cell gun [29, 30]. This is along the same lines of employing a two ½-cell structure to reduce the back-bombardment power as compared with the more classical 1½ cell gun [31]. While these are common methods and they have been shown to reduce the power by up to half, this reduction is not necessarily sufficient for high current applications.

The use of a more exotic cathode material to decrease the impact of the back-bombarded electrons has also been proposed [32]. This concept is built on the principle that the temperature increase in the cathode is directly related to the stopping distance of the particular cathode material. A material with a longer stopping distance will have less energy absorbed at the surface and therefore helps to dissipate some of the back-bombarded beam energy. The use of laser pulses has also been proposed to disperse the heat in the cathode due to the back-bombardment power and therefore reduce the unwanted increase in current [33].

There is a very clear gap in the work on thermionic cathode RF guns, as none of the techniques for back-bombardment mitigation are really scalable to high currents and high average powers.

Additionally there is a lack of theoretical understanding on what design parameters drive the back-bombardment power. Scaling laws would be very helpful in the initial design process and could in principle be used to make predictions for how a particular mitigation technique might perform.

1.2 Overview of Work

This dissertation addresses the need for understanding back-bombardment and develops a new technique for back-bombardment mitigation. To accomplish this four areas of work are explored.

- If suitable approximations are made to the equations of motion then simple analytic models can be derived to predict how back-bombardment power varies as a function of the design parameters in single-cell guns. This model should be able to achieve better than order of magnitude accuracy when comparing the numerical result with simulation. More importantly it should be able to provide insight into the parameter space of how, and to what degree, variations of relevant parameters impact the back-bombardment levels.
- Space-charge forces impact back-bombardment through both the longitudinal field generated by the image charges and the transverse field generated by the beam itself. The longitudinal space-charge effect impacts the back-bombardment power through the virtual cathode effect [34], and by canceling out the effective accelerating field. The transverse space-charge forces defocus the beam and cause some of the back-bombarded particles to deposit their energy on the cavity walls instead of the cathode thereby decreasing the effective area of the back-bombarded beam. The impact of these two effects can be predicted through the use of simple analytic tools and studied through simulation.

- The addition if more accelerating cells will not impact the particles that do not make it out of the first cell and therefore adding additional cells almost always increases the back-bombardment power. However, there are configurations where a multi-cell gun will not further increase the back-bombardment power from its single-cell counterpart. Multi-cell guns will be studied in order to identify these configurations.
- Back-bombardment can be mitigated through a change in the temporal field profile by the introduction of a second RF frequency.

Each of these areas corresponds to a line of inquiry that is somewhat independent of the others; however, together they represent a targeted effort in advancing the state of the art in both the understanding of back-bombardment physics and how to mitigate its impact.

A single-cell RF gun represents the simplest configuration under which back-bombardment occurs and therefore represents our first line of study. Theory and simulation are used to develop an understanding of this process, followed by a comparison with existing test data to validate the models. At the completion of the line of study, a refined model that has been benchmarked against both simulation and experiment will be presented. This is accomplished via performing the following specific tasks:

- Perform an initial study of back-bombardment effects in a short-gap gun via simulation.
- Develop analytical model for back-bombardment in single-cell guns.
- Compare initial analytic model to simulation results.
- Refine the model to account for more realistic physics in the gun and compare with simulations.
- Compare results with existing measurements that have been taken at facilities.

Following the development of analytic models without the inclusion of space-charge forces, the impact of higher beam-currents on back-bombardment is introduced. This work builds an intuitive understanding of the space-charge effects through simple analytic models that describe the major underlying physics involved with space-charge effects. Due to the complexity of space-charge forces, simulation is necessary to determine the precise impacts on a particular gun design; however, simple analytic models can provide insight into how space-charge effects the back-bombardment process. To study the back-bombardment physics with the inclusion of space-charge forces the following topics tasks will be completed.

- Run initial study on the space-charge effects on back-bombardment through simulation.
- Develop analytic model to predict the behavior of longitudinal space-charge effects.
- Develop analytic model to predict the behavior of transverse space-charge effects.
- Compare analytic model to simulation results.

After studying single-cell guns, adding additional cells introduces further complexity that more closely resembles a realistic setting. Many real-world applications of RF guns use more than one cell to further accelerate the beam. It is important to understand how this additional level of complexity impacts the back-bombardment process. This line of study will revolve primarily on simulation as analytic models become much less tractable with multi-cell guns. Because particles that do not make it out of the first cell are not impacted by the addition of a second cell the goal of studying multi-cell guns is to determine if an operating point exists that will not increase the back-bombardment power from its single-cell counterpart. In order to confirm this the following studies will be performed.

- Multi-cell cavities operating in the zero-mode are studied using 1-D and 2.5-D simulation. Note that the zero-mode case represents a mode of operation that is not used.

However, it is analyzed in this dissertation as it represents the only case where the increase in back-bombardment power due to the addition of multiple cells can be estimated. Additionally it represents the simplest configuration from a conceptual standpoint and therefore provides a starting point for further discussions on multi-cell guns.

- Multi-cell cavities operating in the pi-mode are studied using 1-D and 2.5-D simulation.
- Two-cell guns with independently powered cells are studied using 1-D simulations.

Finally, after a comprehensive study of how back-bombardment changes depending on the gun configuration and the beam parameters, an analysis of how adding a harmonic frequency for mitigating back-bombardment is performed. A number of techniques already exist to mitigate back-bombardment as was discussed previously; however, this technique seeks to improve on the existing methods to further reduce the impact of back-bombardment. This will be studied by analyzing a gun that is powered by two frequencies that are phased independently and have different field strengths.

This work provides a comprehensive analysis of how back-bombardment varies over a wide range of both beam design and gun design parameters and presents a novel technique for mitigating the effects. Thermionic cathodes represent reliable electron sources as long as their output current can be properly controlled. This dissertation provides the analysis necessary to help better engineer these guns.

2. Back-bombardment in Single-cell guns

Single-cell guns represent the simplest configuration for an initial study of the back-bombardment process. The analysis begins with a simulation-based study of a particular single-cell gun that was designed to operate in a two-frequency mode for back-bombardment mitigation. For the study performed in this chapter the two-frequency gun will be powered with only the fundamental frequency. After using the simulation study to develop intuition of the process, analytical models are derived by making the necessary simplifications to obtain closed form solutions for the back-bombardment power as a function of the design parameters. These results are then compared with simulations to verify the analytic model. Following this initial development a few refinements are made to the model by reducing the number of simplifications but maintaining a theory that can be solved analytically. These refinements are also compared to simulation. Comparing the different variations of the model with simulation results shows which technique produces the best results in all situations. This model was then used to predict the back-bombardment power that was measured and published in the literature [16]. In this chapter all studies are in the regime where space-charge fields are small compared to the external fields and can therefore be neglected. The effects of space-charge on back bombardment is addressed separately in Chapter 3.

2.1 Simulation studies of a short gap gun

The simulations presented in this dissertation were all performed using SPIFFE [35]. SPIFFE is a 2.5-D particle-in-cell, electromagnetic field solver. The code solves for electromagnetic fields and forces in cylindrical coordinates over a finite grid determined by the simulation input file. The code uses axial symmetry, which means that there is no azimuthal information of the particle

trajectories, or of the fields. While there is no positional information about the particles in the azimuthal direction, the particles are allowed to rotate about the axis. Because of this symmetry condition the particles are treated as a ring.

For the studies presented in this section the field was excited using an antenna. The cavity was allowed to ring up before the cathode was turned on. The antenna method was not used for all simulations as computationally it becomes cumbersome to include this level of detail when running many simulations. Therefore a field map was used for many cases, these situations will be delineated in the text. The cathode is treated as a full thermionic emitter and will emit whenever there is not a surface field preventing acceleration. It is important to note here that although the cathode was turned on and off in simulation instantaneously, in reality the cathode's finite thermal mass requires a finite turn-on/turn-off time.

In this section, the two-frequency gun is simulated operating in single-frequency mode. This was done to characterize the baseline levels of back-bombardment in the gun and how these levels vary as a function of some of the gun parameters. Figure 2 gives a cross-section view of this geometry.

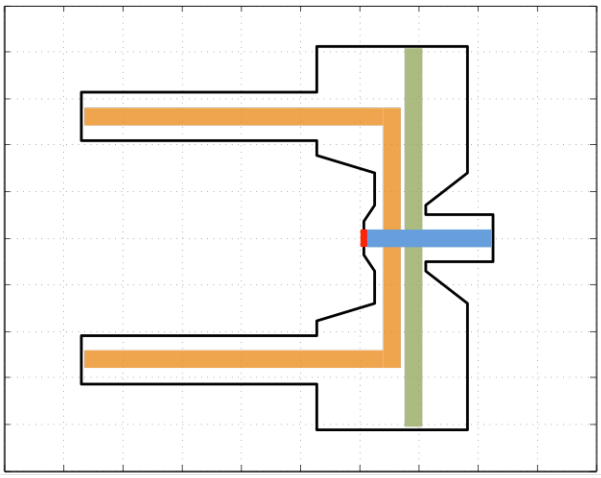

Figure 2: Cross section view of the geometry used in initial simulation studies of back-bombardment. The orange line represents the length that determines the fundamental frequency. The green line represents the length that determines the harmonic frequency. The cathode is shown in red and the nominal beam path is outlined in blue [34].

For this simulation study the operating frequency was varied from 100kHz to 10GHz. Some facilities have RF guns operating as high as ~8GHz, therefore this range represents the full range of operational gun frequencies. In order to maintain a consistent geometry relative to the variation in RF frequency, a uniform scaling (Equation 1) was applied to the geometry to vary the operating frequency of the cavity.

(1)

$$G_{scaled}(r,z) = G_{initial}(r,z)\frac{f_{initial}}{f_{scaled}}$$

Here $G_{scaled}(r,z)$ is the scaled geometry function at the desired frequency, $G_{initial}(r,z)$ is the initial geometry function, $f_{initial}$ is the known resonant frequency of the initial geometry computed using SUPERFISH [36], and f_{scaled} is the desired resonant frequency for $G_{scaled}(r,z)$. To ensure accurate tuning, the mesh size for one cavity geometry was systematically reduced until the resonant frequency was unchanged from run to run. This mesh interval was then scaled with frequency to maintain a constant relative resolution for each gun

geometry. Each geometry was then individually tuned to meet a tolerance of $f_{scaled} \pm 100\ kHz$. This was done to satisfy that the cavities were operating close to the desired resonant frequency when excited with an antenna. For 100MHz this corresponds to 0.1% error in the frequency while for 10GHz this is an even better tolerance.

The other parameter that was varied for this scan was the bunch-charge emitted per RF period. For a constant frequency, this corresponds to an increase in the beam-current. Similarly for a constant bunch-charge per RF period a change in the RF frequency also corresponds to a change in the beam current.

The peak field for these simulations was set to a constant 10MV/m for the whole scan. This was done to see the effect of the back-bombardment power on the gap length independent of the peak field. As the frequency increases the gap-length will decrease which corresponds to a decrease in the total effective acceleration in the gun, gap voltage. This field value was chosen as it will not induce break-down at low range of the simulation scan. For simulations excited by an antenna, the peak field on axis was verified to be 10 MV/m in each case, indicating that the antennas were properly powering the cavities. Along with the spatial resolution the temporal resolution was also scaled with frequency while the number of macro particles was kept constant. For each simulation, the time-averaged back-bombardment power is computed by measuring the total energy of the particles deposited on the cathode during one RF period, and dividing by the RF period. Figure 3 shows the back-bombardment power as a function of bunch-charge for constant frequency (left) and as a function of gap-voltage (right).

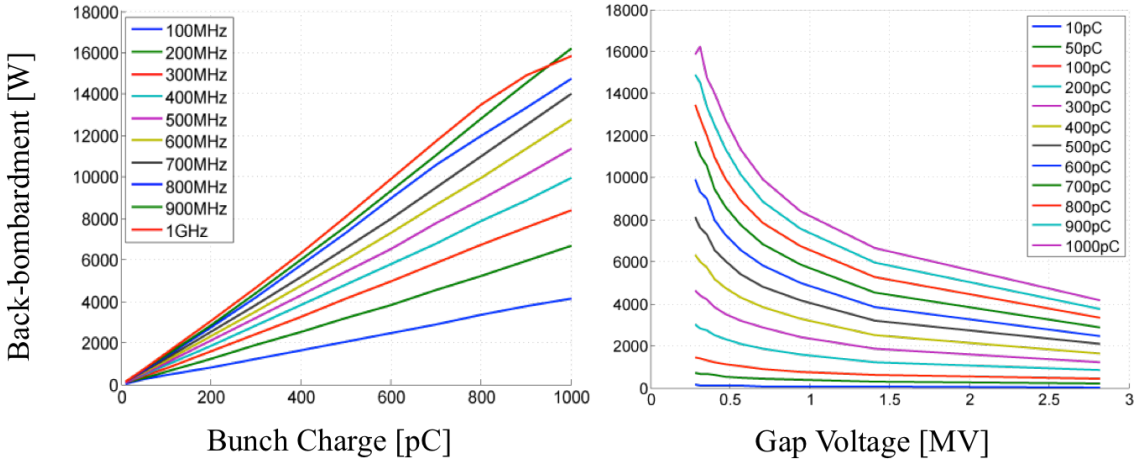

Figure 3: Variation in the back-bombardment power as a function of bunch charge for a peak field of 10MV/m (left) and gap voltage (right). Note that for a constant RF frequency, a change in the emitted charge per RF period corresponds to a change in the beam current. Here keeping a constant peak field and varying the operating frequency, as explained above, was used to vary the gap voltage [34].

This shows that for a constant frequency (left), the back-bombardment power is linear with bunch charge, and for a constant bunch charge there is an inverse relationship of the back-bombardment power with gap-voltage. Again the bunch-charge refers to the amount of charge emitted from the cathode per RF period. Therefore as the bunch charge is increased for a constant operating frequency, the beam current is being increased. It is expected that this will result with a subsequent increase in the back-bombardment power. The more current emitted from the cathode per RF period, the more current will return to the cathode through the back-bombardment process, and therefore the power will increase. The variation with voltage is a little subtler and will be discussed in more detail with the analytical model however study of the relationships shown in Figure 3 gives some initial insight about what we can expect. Analysis of the curves on the right side of Figure 3 showed that the relationship of the back-bombardment power to the gap voltage (for these particular simulation studies) was not exactly a simple $P \propto 1/V_{gap}$ relationship but more of a $P \propto 1/(1 + V_{gap})$. However, the back-bombardment power is inversely proportional to the relativistic energy γ, which is related to the gap voltage by

Equation 2. The gap voltage (V), along with the particle's launch phase and the gun's transit time factor (T) determines the energy gained by that particle in crossing the gap. For an optimal launch phase, the maximum value for the relativistic factor (γ) attained by the particle is,

(2)

$$\gamma_{max} = \frac{qTV}{m_0 c^2} + 1$$

This gives the proportionality shown by Equation 3.

(3)

$$P \propto \frac{Q}{\gamma_{max}}$$

The direct relationship to the bunch-charge emitted per RF period is again more of a relationship to the beam current than the charge. This will be discussed more in later sections however for this study the bunch charge was used as the parameter of choice for discussion. Fitting the simulation data from Figure 3 to Equation 3 produced a proportionality constant of 24.25×10^{12} with an $R^2 = 0.9955$. Here R^2 is defined by Equation 4:

(4)

$$R^2 = 1 - \frac{SS_{res}}{SS_{tot}}$$

Here SS_{res} and SS_{tot} are the sum of the squares of the residuals and the total sum of the squares respectively. This shows that for the gun design in Figure 2 the back-bombardment power is directly proportional to the bunch-charge emitted per RF period (related to the beam current) and inversely proportional to the γ_{max} of the gun. By substituting Equation 2 into Equation 3, and substituting the peak gap voltage as a function of frequency, the relationship of back-bombardment power to the operating frequency for this simulation study is given by Equation 5

(5)

$$P \propto \frac{10fQm_0c}{qTE_0 + 10fm_0c}$$

Equation 5 was then used to predict the back-bombardment power over a select number of frequencies and bunch charges, shown in Figure 4.

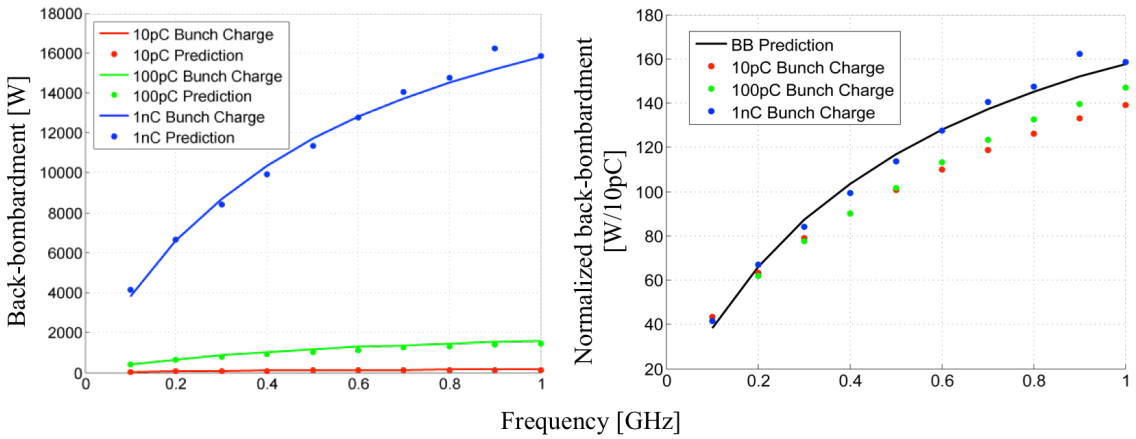

Figure 4: Comparison of empirical model with simulation data for three bunch charges over the whole frequency range. Left shows the back-bombardment power as a function of frequency for three values of bunch charge compared with the empirical model on an absolute scale while the right side shows the three simulation runs with the corresponding empirical model on a normalized scale [34].

This shows that the empirical model predicts the trends with these two parameters and is reasonably accurate at predicting the power levels. On the normalized scale the empirical model does not do as well at predicting the trend for low bunch-charge. This is likely because the high bunch-charge results have higher back-bombardment power levels that will dominate the curve fitting process. While the empirical model gives initial insight into how back-bombardment varies as a function of the chosen parameters, these parameters have not been fully generalized to any single-cell gun design.

2.2 A first principles analysis of single-cell guns

In order to study the back-bombardment process in more general terms, a first-principles model is developed using approximations that allow for closed form solutions to the back-bombardment power as a function of the gun parameters. This analytic model is then compared with simulation results for both a pillbox cavity field profile and for the field profile produced by the gun design analyzed in the previous section.

2.2.1 Derivation of the analytic model

The analytic model is derived using approximations that allow for exact solutions of the back-bombarded particles' kinetic energy, while maintaining the two fundamental properties of the gun that create back-bombardment: 1) the field changing sign and 2) the reversal of the electrons' velocities. These properties are incorporated using the field profile given by Figure 5, and the velocity profile given by Equation 6. While Equation 6 is not a true representation of the electron velocities in a RF gap, it does serve as a reasonable starting point for the simplified analytic theory.

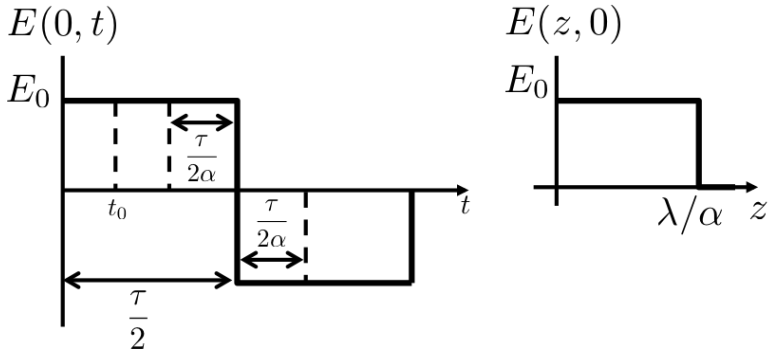

Figure 5: Temporal (left) and spatial (right) field profiles used to derive the simplified analytic model.

Here t_0 represents the particle emission time, τ is the RF period, E_0 is the peak field, and $1/\alpha$ is the relative gap length.

(6)

$$v_z(t) = \begin{cases} c & \int_{t_0}^{t} E(t)dt > 0 \ (particles\ moving\ toward\ the\ exit) \\ 0 & \int_{t_0}^{t} E(t)dt = 0 \ (particles\ at\ rest) \\ -c & \int_{t_0}^{t} E(t)dt < 0 \ (particles\ moving\ toward\ the\ cathode) \end{cases}$$

These approximations can be used to study back-bombardment power by determining the boundary between particles that exit the gun and particles that return to the cathode. This is accomplished by defining a theoretical particle that exits the gun with zero energy. A particle traveling at a constant velocity c has a cavity transit time of $t_{transit} = \tau/\alpha$. A particle that exits with zero energy will see an equal amount of positive and negative field and therefore it will have an emission time of $t_0 = \tau/2 \ - \tau/(2\alpha)$. The kinetic energy of particles exiting the gun is then calculated by solving Equation 7 for all particles with $t_0 \ < \frac{\tau}{2} - \frac{\tau}{2\alpha}$:

(7)

$$K_e(t_0) \ = \int_{t_0}^{t_0+t_{transit}} E(t)cdt$$

Note that this analysis assumes the kinetic energy is independent of the particle velocity. While this is unphysical it is a critical approximation for solving for the back-bombardment power. For the back-bombardment case, any particle that reaches zero energy before $t_{transit}$ would then stop, reverse direction, and travel back to the cathode. These particles arrive at the cathode at time $t_{bb} \ = \ 4(\tau/2 - t_0)$ after emission. Note that for the back-bombarded particles, the transit time is a function of the emission time, as some particles do not make it all the way across the gap before reversing direction. Substituting t_{bb} for $t_{transit}$, the kinetic energy as a function of injection time for back-bombarded particles can be found using Equation 7. These results

combined give the final kinetic energy of all particles as a function of injection time (left side of Figure 6). While this gives the final energy of all particles as a function of their emission time, it does not provide the energy deposited on the cathode surface in terms of absolute time. In order to compute the back-bombardment power, the kinetic energy deposited on the cathode as a function of time is required.

The first particle to reach cathode has zero energy and is emitted last at $t = \tau/2$. This particle does not gain any energy and arrives at the cathode at exactly the same time. Note that this is a theoretical particle that represents the boundary between the region where particles are emitted off the cathode and the region where there is a surface field preventing emission. The last particle to reach the cathode is emitted first, traverses the cavity twice, and arrives at the cathode with a kinetic energy of K_e^{max}, defined by Equation 8, at time $t = t_0 + 2t_{transit}$.

(8)

$$K_e^{max} = \int_0^{L_{gap}} E(z)dz$$

This gives a time domain for the energy deposited on the cathode of $\frac{\tau}{2} \leq t \leq \frac{\tau}{2\alpha} + 2t_{transit}$, with a range of $0 \leq K_e \leq K_e^{max}$. These points define the linear function that represents the kinetic energy deposited on the cathode as a function of time (right side of Figure 6).

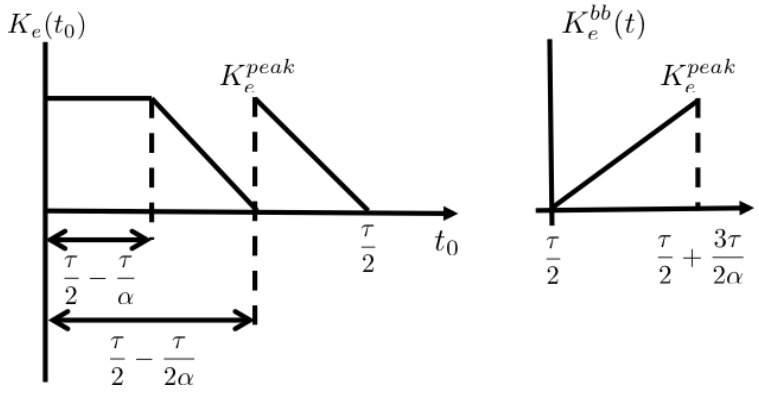

Figure 6: Left: Final kinetic energy as a function of injection time t_0 for all particles emitted from the cathode. Right: Final kinetic energy of the back-bombarded particles arriving at the cathode as a function of time.

To examine the validity of this model, the relativistic equations of motion (Equation 9) are solved numerically using the Runge-Kutta method for a gun with $\alpha = 8$, a peak field of 20 MV/m, and a RF frequency of 1.5 GHz.

(9)

$$\frac{dv}{dt} = \begin{cases} \frac{E_0 q}{m_0}\sin(\omega t)\left(\frac{1}{\left(1-\frac{v^2}{c^2}\right)^{-\frac{1}{2}} + \frac{v^2}{c^2}\left(1-\frac{v^2}{c^2}\right)^{-\frac{3}{2}}}\right) & |z| < \frac{\lambda}{\alpha} \\ 0 & |z| > \frac{\lambda}{\alpha} \end{cases}$$

This was used to compute the final kinetic energy as a function of injection phase and is compared with the analytical model in Figure 7.

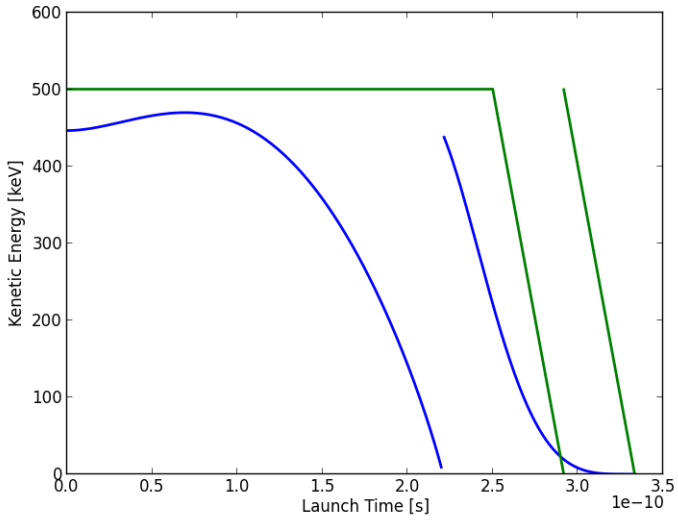

Figure 7: Comparison of Figure 6 with numerical solution, Blue: Numerical solutions to the relativistic equations of motion for the final energy of a particle emitted at some time t_0. Green: Final energy as a function of emission time as defined by Figure 6.

Upon inspection, these two curves appear to be very different. However, when computing back-bombardment power, only the area under the curve to the right of the discontinuity is of importance. This is because the region to the left of the discontinuity represents particles that exist the gun and therefore do not contribute to the back-bombardment heating. A visual inspection of the region to the right of the discontinuity clearly shows that the linear model of kinetic energy deposited on the cathode should be a reasonable approximation when computing back-bombardment power.

Integration of the kinetic energy as a function of time (right side of Figure 6), gives the energy deposited K_e^{dep} on the cathode per RF period in terms of the peak kinetic energy (Equation 8),

(10)

$$K_e^{dep} = \frac{3}{4\alpha f} K_e^{max}.$$

For a pillbox cavity $K_e^{max} = E_0\lambda/\alpha$. Because most cavities have complicated geometries and their axial field maps are computed using numerical codes, analytical solutions to Equation 8 are not always possible. Irregularities in the geometry can introduce field profiles that do not have a single analytical expression describing their behavior. In many cases these field profiles can be described as a sum of spatial harmonics however it is often a simpler process to integrate the field numerically using the field map itself. The use of a Riemann sum and normalizing to the peak energy gain of a pillbox cavity gives the scaling K,

(11)

$$K = \sum_{i=0}^{N} \frac{E(i\Delta z)}{E_0 N}$$

Here $\Delta z = \lambda/\alpha\, N$, N is the number of data points along the field map (determined by the field map), and E_0 is the peak value of the axial field. This gives a scaling that takes into account the spatial variation in the field. In more general terms, this is the integral of the spatial field normalized to the peak field multiplied by the gap length. Multiplying K_e^{dep} by the RF frequency and the beam current, and substituting $E_0 cK/\alpha f$ for K_e^{max}, yields the time average back-bombardment power

(12)

$$P_{ave} = \frac{3IE_0}{4\alpha^2 f} TK$$

Here I is the beam current and T is the transit time factor for a pillbox cavity [37]. The transit time factor is a common scaling measure used in accelerator physics to account for the time varying component of the RF field. Because we have chosen a square wave approximation, introduction of the unit-less transit time factor helps to account for this additional variation in the

fields. For a particle traveling at the speed of light in a pillbox cavity the transit time factor is easily computed as a function of the relative gap length:

(13)

$$T = \frac{\sin(\pi/\alpha)}{\pi/\alpha}$$

2.2.2 Comparison with simulations

A simulation study using SPIFFE was performed to verify the model given by Equation 12. Simulations were run using a variety of operating frequencies, fractional gap lengths, and peak fields. Two longitudinal field profiles were used: 1) a pillbox TM_{010} mode which is a good approximation for many applications, and 2) a longitudinal field map from a representative single-cell design [38, 39].

The fractional gap length $\alpha = \lambda_{rf}/L_{gap}$, represents the actual gap length normalized to the RF wavelength. For these simulation studies, the peak field was varied from 2 MV/m to 30 MV/m, the frequency was varied from 100 MHz to 2 GHz, and α was varied from 2 to 14. Typically the first cell in a gun has a fractional gap length of 4. Some configurations call for a longer first cell, with a fractional gap length approximately equal to 3. The analysis in this chapter is extended to a fractional gap length of 2 to include all possible gun configurations. While the simulations were run over a wide range of parameters, only a few representative data sets are presented in Figures 8-10 to indicate the trends. The first two parameters, frequency and fractional gap length, both have geometrical implications and therefore are addressed first. Figure 8 shows the back-bombardment power as a function of frequency for three values of α, and Figure 9 shows the back-bombardment power as a function of α for three frequencies.

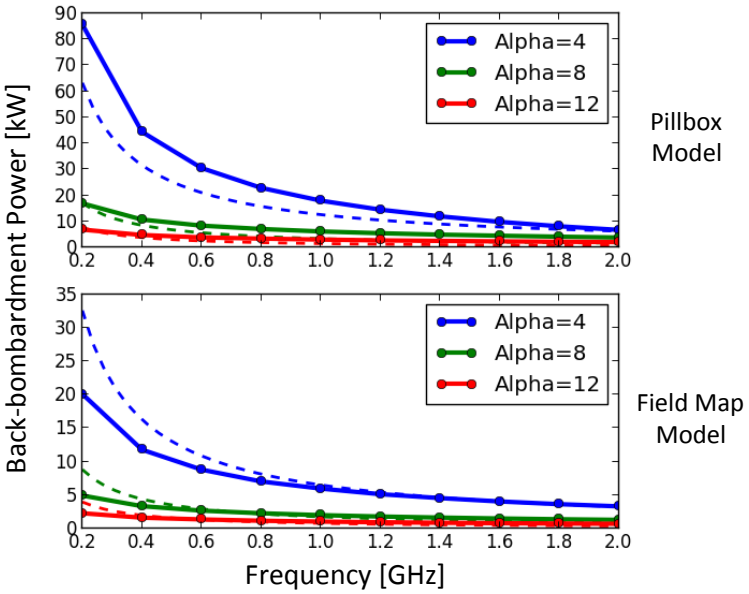

Figure 8: Comparison of Equation 6 and simulation, Top: Comparison of analytic theory (dashed line) with the simulation data (solid line) for a pillbox cavity. Bottom: Comparison of analytic theory (dashed line) to the simulation data (solid line) for the single-cell field map. The peak field for these comparisons is 20 MV/m.

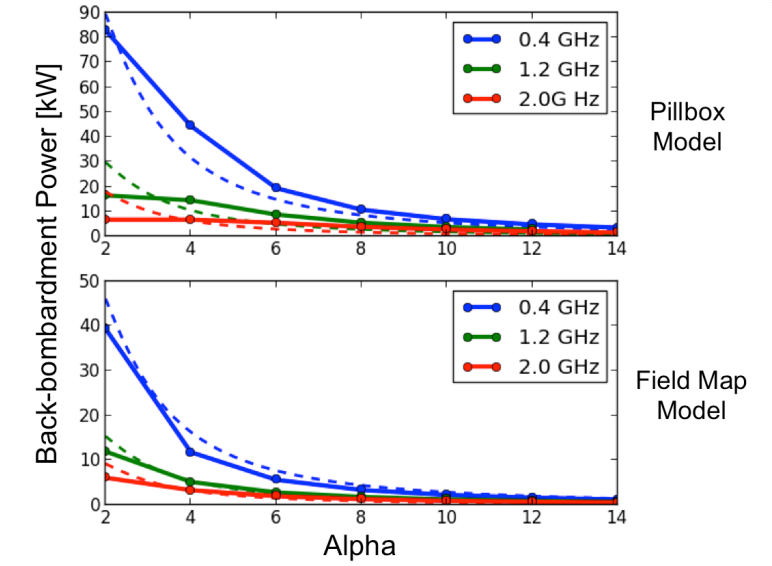

Figure 9: Comparison of Equation 6 and simulation, Top: Comparison of analytic theory (dashed line) with the simulation data (solid line) for a pillbox cavity. Bottom: Comparison of analytic theory for the single-cell field map (dashed line) to the simulation data (solid line) for the single-cell field map. The peak field for these comparisons was 20 MV/m.

It is clear by inspection of Figures 8 and 9, that the analytic model accurately predicts the trends for both the variation with frequency and the variation with fractional gap length. For the pillbox case in Figure 8 the analytic model deviates significantly from the simulation for low values of α and higher frequencies. This is likely because for long gap lengths relative to the RF wavelength, cases arise where particles get stuck in the cell during their emission period and then are ejected during the following period. These are treated as back-bombarded by the analytic model but do not actually reach the cathode. This does not happen for the field map because the field falls off towards the exit of the cavity.

The third free parameter in the gun design is the peak field. Figure 10 shows the back-bombardment power as a function of peak field for an RF frequency of 1 GHz.

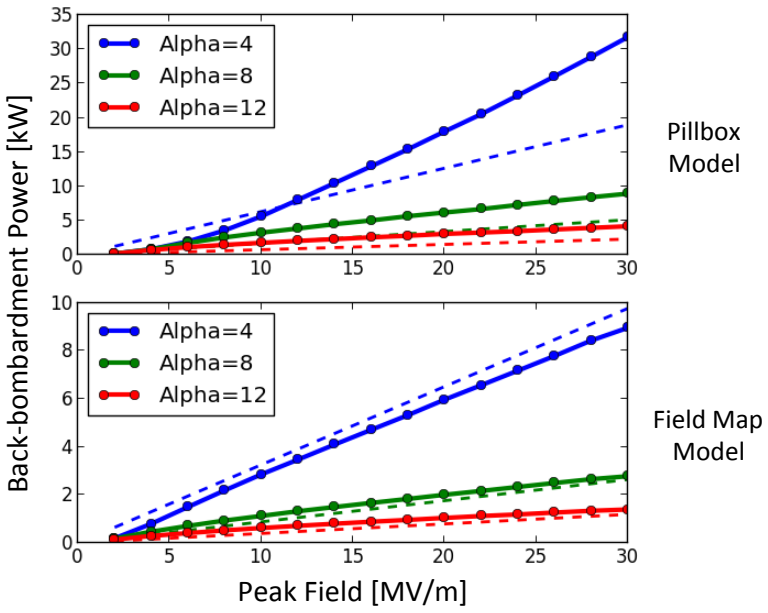

Figure 10: Comparison of Equation 6 and simulation, Top: Comparison of analytic theory for the pillbox cavity (dashed line) with the simulation data for a pillbox cavity (solid line). Bottom: Comparison of analytic theory for the single-cell field map (dashed line) to the simulation data for the single-cell field map (solid line).

Figure 10 shows a very good comparison for the field map case and a modest agreement for the pillbox case. The linear trend with field is accurately predicted for higher α, but there is a clear nonlinear variation with field for low values of α. As discussed previously the model tends to break down for low values of α, so this is not unexpected. Figures 8-10 show that frequency, fractional gap length, and peak field are fundamental parameters that govern the back-bombardment process and that Equation 12 qualitatively predicts how the back-bombardment power varies with these parameters.

2.3 Refinement of the constant velocity assumption

The initial model was developed using the assumption that the particles were traveling at the speed of light. In single-cell guns this is not a very accurate assumption and the peak velocity is typically significantly lower than the speed of light around $\beta = 0.8$, with an average velocity even lower. In order to correct for this two methods for approximating the particle velocity in the gun were explored. The first method assumes a constant acceleration, or linear velocity gain and uses the linear average velocity as the particle velocity. The second method assumes a linear energy gain and uses the average energy to compute the particle velocity. These two techniques were used to refine Equation 12 and the results are compared with simulations.

2.3.1 Derivation of the model with arbitrary constant velocity

As was stated earlier the particle velocity in the gun is assumed to follow the approximation where particles moving toward the exit have constant positive velocity and particles traveling towards the cathode have constant negative velocity. Before discussing how the effective velocity is computed, the analytic model is presented in terms of an arbitrary effective velocity. Equation 13 gives the velocity profile used for this analysis.

(13)

$$v_z(t) = \begin{cases} v_{eff} & \int_{t_0}^{t} E(t)dt > 0 \\ 0 & \int_{t_0}^{t} E(t)dt = 0 \\ -v_{eff} & \int_{t_0}^{t} E(t)dt < 0 \end{cases}$$

For the most part the back-bombardment power equation derived for an arbitrary constant velocity is the same for the derivation in the pervious section were the velocity was assumed to be the speed of light. The major difference is in the transit time. Equation 14 gives the particle transit time, which is a critical component to computing the back-bombardment power, in terms of an arbitrary effective velocity.

(14)

$$t_{transit} = \frac{\lambda}{v_{eff}\alpha}$$

Note that now the transit time is given in terms of the RF wavelength, the effective velocity, and the fractional gap length. If the velocity were the speed of light, this would reduce back to being only a function of the RF period and the fractional gap length. Equation 7 can then be solved as before however now the effective velocity is substituted for the speed of light. Equation 7 can be used as before to find the kinetic energy deposited on the cathode per RF period in terms of the maximum kinetic energy, Equation 15.

(15)

$$K_e^{dep} = \frac{3\lambda}{4\alpha v_{eff}} K_e^{max}$$

Multiplying K_e^{dep} by the RF frequency and the beam current, substituting $E_0\ \lambda K/\alpha$ for K_e^{max} and substituting c/f for λ yields the time average back-bombardment power, Equation 16.

(16)

$$P_{ave} = \frac{3E_0 I c^2}{4\alpha^2 f v_{eff}} TK$$

Here I is the beam current and T is the transit time factor for a pillbox cavity [37]. Note that there is an additional factor of the speed of light in the numerator. This is due to the reduced effective velocity, if the effective velocity approaches the speed of light, this factor will cancel out and we are left with the original back-bombardment equation. For a particle traveling at a constant velocity in a pillbox cavity the transit time factor given by Equation 17:

(17)

$$T = \frac{\sin(\pi c/\alpha v_{eff})}{\pi c/\alpha v_{eff}}$$

2.3.2 Calculating the effective velocity

With the back-bombardment power given in terms of some arbitrary constant velocity, the two methods for computing this velocity can be assessed. The first method for calculating the effective velocity assumes the electrons accelerate from rest to the maximum velocity with a constant acceleration and therefore the velocity is linear with position. The effective velocity is then calculated as the average value of this linear relationship.

In order to compute the linear average velocity the maximum final velocity of a particle leaving the gun is computed assuming it is accelerated from rest to the maximum kinetic energy given by Equation 8. In general the kinetic energy is defined by $K_e = (\gamma - 1)m_0c^2$, where $\gamma =$

$1/\sqrt{1 - v^2/c^2}$. Equation 8 is used to compute the final value of γ or γ_f which in turn can be used to compute the final velocity by $v_f = c\sqrt{1 - 1/\gamma_f^2}$. The linear average velocity is simply $v_{eff} = v_f/2$. It is important to note that this approach is non-physical because the velocity does not vary in a linear fashion due to relativistic effects. However in some of the gun configurations the electrons are not yet fully relativistic and this should better approximate the time-scales of the back-bombardment process in these regions.

The second approach to computing the effective velocity in the gun is to assume that the acceleration is not constant but that the energy gain is constant. This allows relativistic effects to be more directly taken into account, as the velocity does not in fact increase in a linear fashion. Kim [40] showed through the analysis of electron acceleration in RF guns that near the cathode in a long photocathode gun, γ increases linearly with position by Equation 18.

(18)

$$\gamma(x) \approx 1 + \frac{E_0 q}{2 m_0 c^2} \sin(\phi_0)\, z$$

For a single-cell gun this is a good approximation for the energy gain of particles that are not back-bombarded. The kinetic energy is related to γ linearly by $K_e = (\gamma - 1) m_0 c^2$. Therefore the average value of the kinetic energy should give a closer approximation to the true average velocity in the gun. Assuming that initially the particles are at rest, the average energy in the gun is simply $K_e^{max}/2$. The effective velocity is then computed from γ as before; Equation 19 gives this explicitly.

(19)

$$v_{eff} = c\sqrt{1 - \left(1 + \frac{qE_0\lambda}{2m_0c^2\alpha}\right)^{-2}}$$

To explore the validity of these two models the kinetic energy as a function of launch time is compared to the numerical solutions of the equations of motion as was shown in Figure 7, this result is shown in Figure 11.

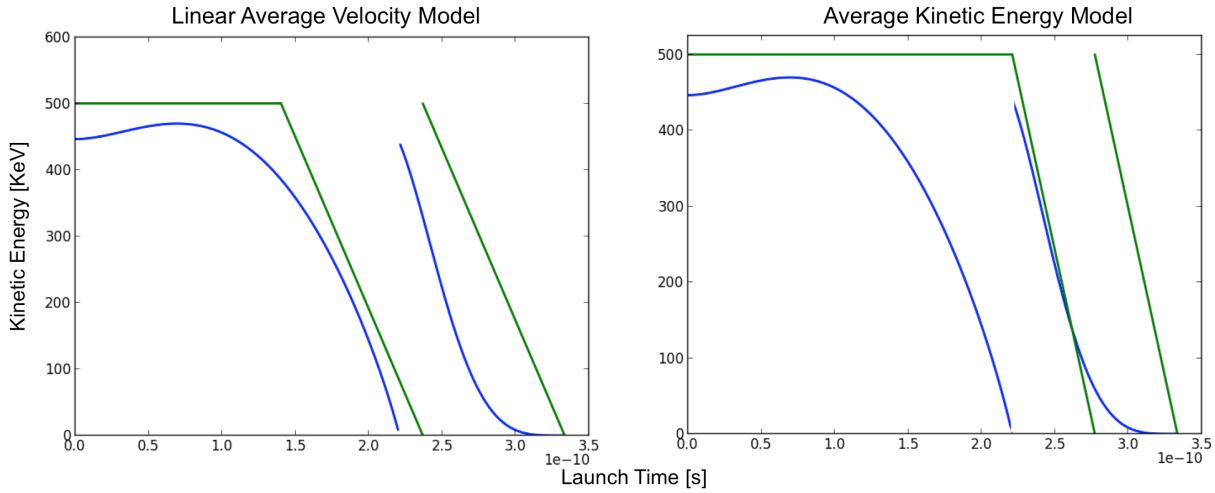

Figure 11: Comparison of numerical solution to relativistic equations of motion (Blue) with the linear model for kinetic energy using constant velocity (Green). Left uses the linear average velocity for the effective velocity and right uses Equation 19 to compute the effective velocity. The peak field was 20MV/m, the RF frequency was 1.0 GHz, and alpha was 8 for this comparison.

Figure 11 shows that both the models perform quite differently. While upon first inspection it appears as though the linear average model does a better job at predicting the time domain of the back-bombarded particles, it will over predict the back-bombardment power because the area under the curve to the right of the discontinuity is the important factor when computing the back-bombardment power. This indicates that the different models will be better for computing different aspects of the gun dynamics. For instance if one wanted to approximate the fractional energy spread, the average velocity may be better, but for computing back-bombardment power

the average energy may be better. In a later section the time domain prediction of these two models over the whole range of parameters is compared to evaluate this aspect of the prediction.

2.3.3 Comparison with simulations

Using both the methods for computing the average velocity, the results of Equation 16 are compared with simulation data over the same representative data that were shown in the previous section. Figure 12 shows the back-bombardment power as a function of frequency for three values of alpha.

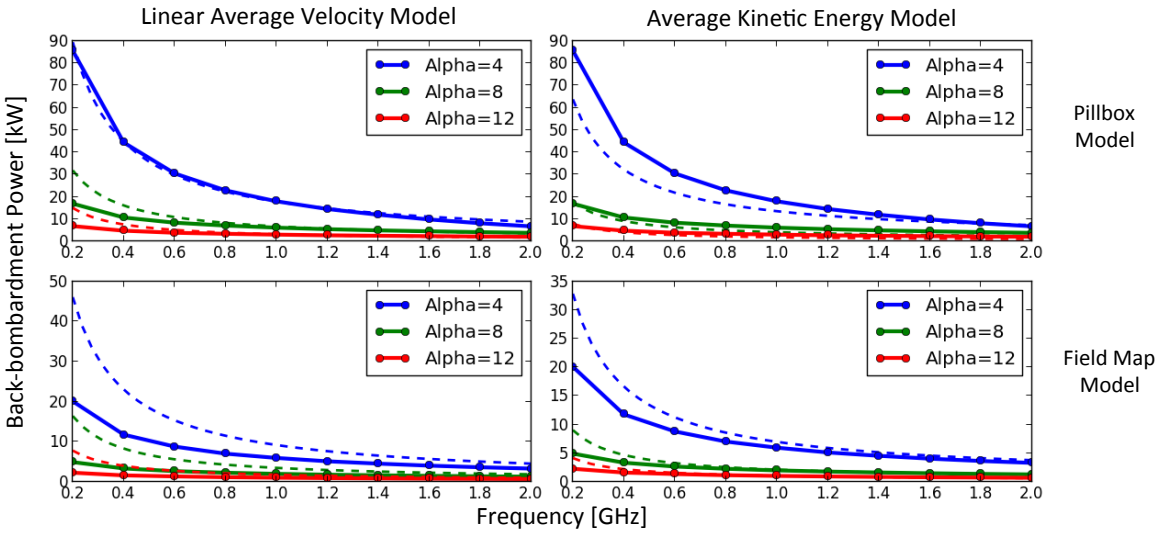

Figure 12: Comparison of Equation 17 and simulation as a function of frequency for three values of alpha. The peak field was 20MV/m for this comparison. Both linear average velocity and average energy velocity were used for this comparison.

This shows a good comparison for both the average velocity model and the average energy model. The average velocity model appears to better predict the dynamics in the pillbox, while the average energy model appears to predict the field map case slightly better. The trade-off between these two models is discussed in a later section. Figure 13 shows the back-bombardment power as a function of alpha for three values of frequency.

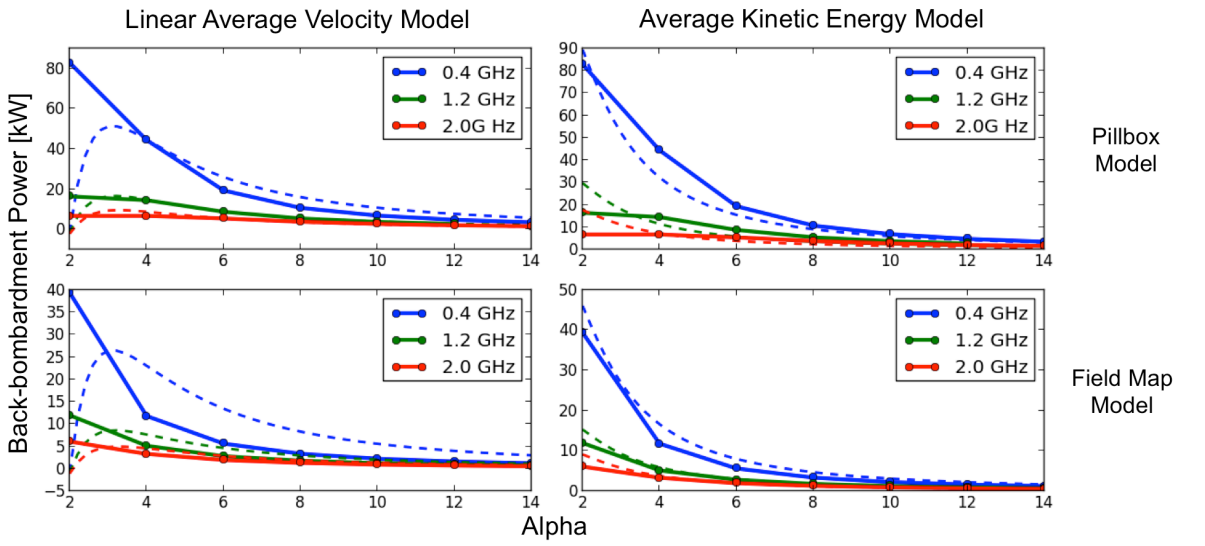

Figure 13: Comparison of Equation 17 and simulation as a function of alpha for three values of frequency. The peak field was 20MV/m for this comparison. Both linear average velocity and average energy velocity were used for this comparison.

This shows a very good comparison for the average energy model with a modest comparison for the average velocity model. Additionally the average velocity model breaks down significantly for values of alpha less than 4. This is likely due to the fact that for long gap lengths the velocities are highly variable and therefore a simple average velocity is not adequate to predict the physics. Additionally the transit time factor becomes an issue for long gap lengths and approaches zero. Figure 14 shows the variation in the back-bombardment power as a function of the peak field in the cavity for three values of alpha at a frequency of 1 GHz.

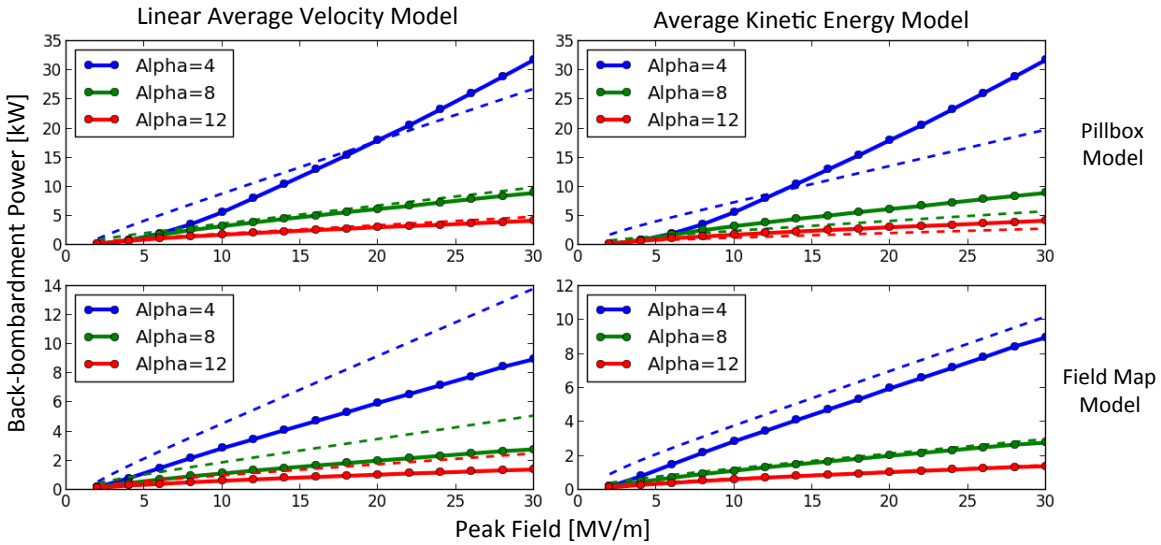

Figure 14: Comparison of Equation 17 and simulation as a function of the peak field in the cavity for three values of alpha at a frequency of 1GHz. Both linear average velocity and average energy velocity were used for this comparison.

Here, as with the variation in frequency, the average velocity is better for the pillbox case and the average energy is better for the field map case. The average velocity case is far poorer for the field map case while the average energy model is still in modest agreement for the average energy case. This indicates that the two methods may perform better under different conditions.

While using an average velocity is still not a physical representation of the dynamics in the gun it is useful for analyzing the back-bombardment power. Using a model that calculates an effective velocity based on the kinetic energy in the gun represents an improvement on the initial model as rarely are the particles traveling close to the speed of light in the first cell of an electron gun.

2.4 Refinement of the temporal field profile

Another possible improvement to the model is to reintroduce a sinusoidal waveform for the time varying component of the field instead of treating it as a square wave. This is made possible by

the constant velocity approximation. This is done in two stages, first by assuming a speed of light velocity (for simplicity) then by applying the arbitrary velocity analysis that was done in the previous section. These results will then be compared with simulation as before.

2.4.1 Sinusoidal analysis with speed of light velocity

To analyze the kinetic energy as a function of t_0 similar to the previous model, a time varying component of the field is substituted into Equation 6 to give Equation 20.

(20)

$$K_e(t_0) = \int_{t_0}^{t_0+t_{transit}} cE_0 \sin(\omega t) dt$$

This equation is solved in the same way as the square wave analysis using the transit time $t_{transit} = \tau/\alpha$, to give the result in Figure 15.

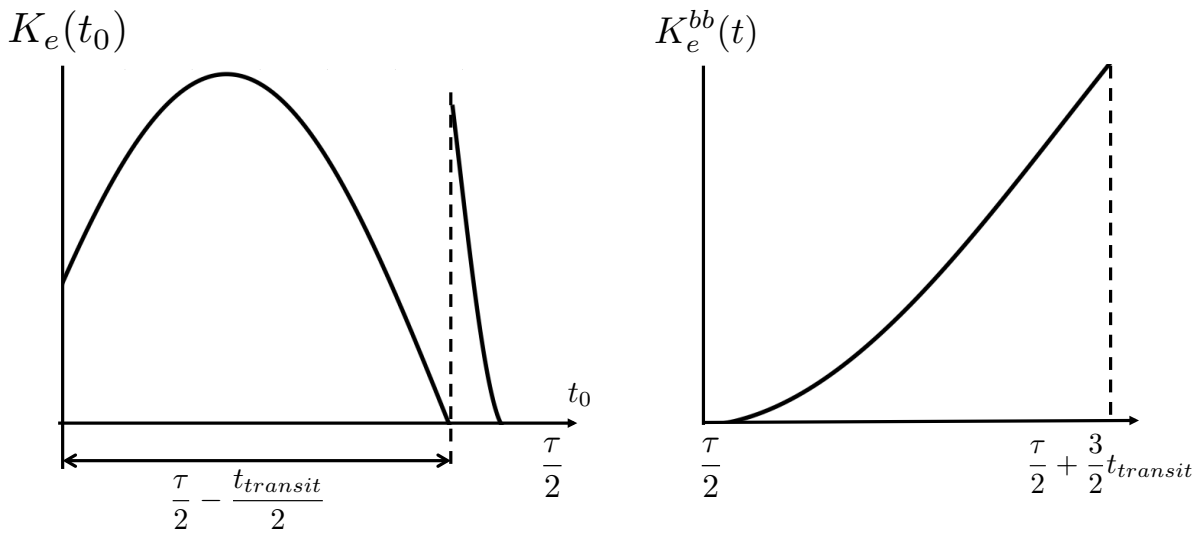

Figure 15: Theory with sine field and speed of light velocity Left: Kinetic energy as a function of injection time for all particles assuming an arbitrary constant velocity. Right: Kinetic energy as a function of time for the back-bombarded particles assuming an arbitrary constant velocity.

The addition of a sinusoidal field variation has given curvature to the kinetic energy as a function of emission time. This gives a more realistic distribution of kinetic energy for the particles that

make it out of the gun and adds a small tail onto the back-bombardment region. Note that the curvature in Figure 16 will vary significantly depending on the gap length and peak field. The fractional gap length and peak field used for this picture was 8 and 20MV/m respectively. As with before, this result can be compared to the numerical solutions of the relativistic equations of motion to examine the validity, shown in Figure 16.

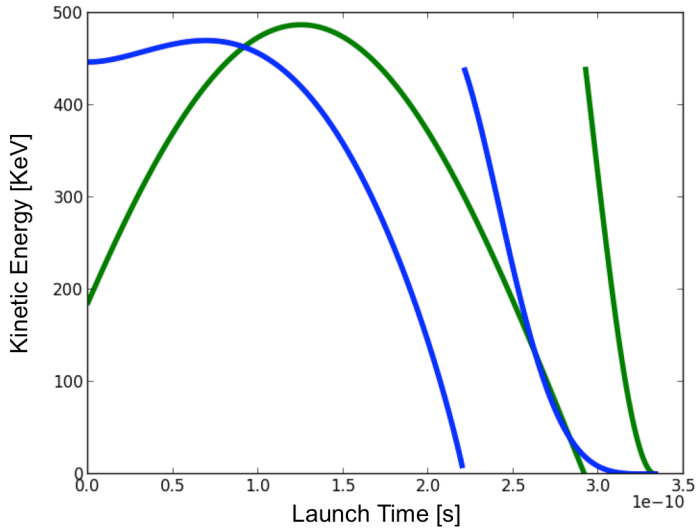

Figure 16: Comparison of numerical solution to relativistic equations of motion (Blue) with the result given by the left side of Figure 15 (Green). The peak field was 20 MV/m, the RF frequency was 1.0 GHz, and alpha was 8 for this comparison.

Figure 16 shows a better comparison for particles that exit the gun when compared to the square wave model. In the square wave model most particles exit at the peak kinetic energy while for the sinusoidal case only a small range of particles exit at the peak kinetic energy. Additionally the slight curvature in the back-bombardment region is similar to that of the numerical solutions. The time domain of this figure is similar to the time domain for the square wave analysis, which is expected because both assume the same speed of light constant velocity. Integrating the right side of Figure 15 gives the energy deposited on the cathode per RF period given for a sinusoidal field:

(21)

$$K_e^{dep} = \frac{E_0 c}{4\pi^2 f^2}\left(3\sin\left(\frac{\pi}{\alpha}\right) - \sin\left(\frac{3\pi}{\alpha}\right)\right)$$

Multiplying by the beam current and the RF frequency gives the time average back-bombardment power:

(22)

$$P_{ave} = \frac{I E_0 c}{4\pi^2 f}\left(3\sin\left(\frac{\pi}{\alpha}\right) - \sin\left(\frac{3\pi}{\alpha}\right)\right) K$$

Comparing Equation 22 with the previous model for back-bombardment power shows that the frequency and field relationships are preserved while the relationship with alpha is now slightly different. Consequently it is expected that the comparison with simulation will only be different for varying fractional gap length.

This new model is compared with simulation data in Figures 17-19. Figure 17 shows the variation of back-bombardment as a function of frequency.

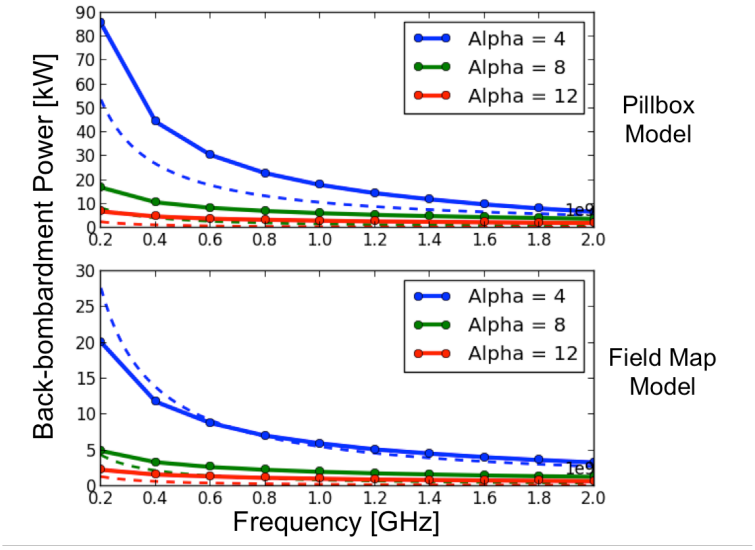

Figure 17: Comparison of Equation 22 and simulation as a function of frequency for three values of alpha. The peak field was 20 MV/m for this comparison.

This shows that the model agrees well with the simulation for predicting the variation in frequency, however the variation in alpha appears quite different and is predicted to fall off faster than the simulation. This assessment is verified by the comparison given by Figure 18.

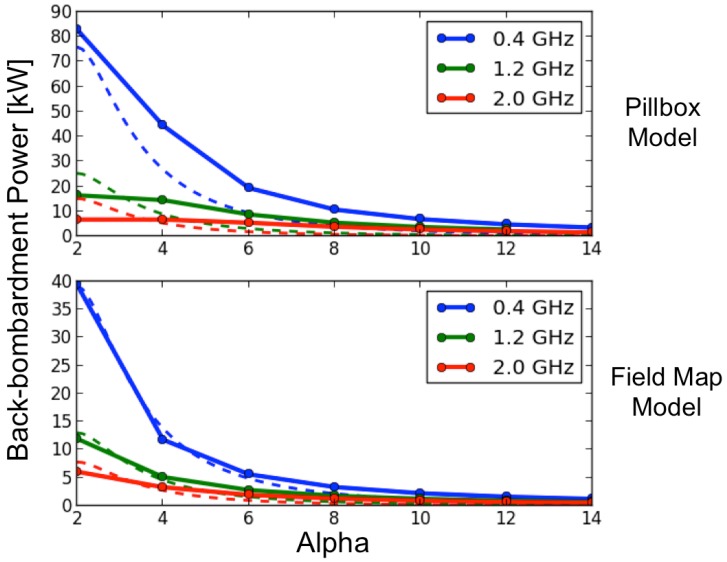

Figure 18: Comparison of Equation 22 and simulation as a function of alpha for three values of frequency. The peak field was 20MV/m for this comparison.

This shows that Equation 22 predicts a much faster fall-off of the back-bombardment power with the fractional gap length for the pillbox model. This is slightly more difficult to see for the field map model; however, it is still present and is very clear when looking at Figure 19, which shows the variation in the back-bombardment with the peak field.

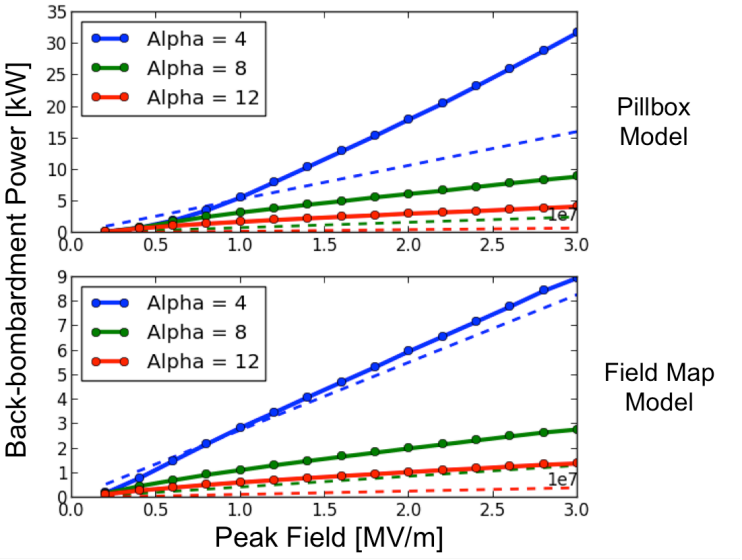

Figure 19: Comparison of Equation 22 and simulation as a function of the peak field in the cavity for three values of alpha at a frequency of 1GHz.

Figure 19 shows how the discrepancy in the variation with alpha drastically impacts how the back-bombardment is predicted. While the linear trend remains the same the slopes do not match as well as the previous model.

2.4.2 Analysis of sinusoidal field with arbitrary constant velocity

This model can be improved by re-introducing the average velocity models to Equation 20. Figures 20 and 21 show the kinetic energy as a function of the injection time and the kinetic energy deposited on the cathode as function of time for the sinusoidal time varying field with an effective velocity equal to the average velocity and the velocity of the average energy respectively.

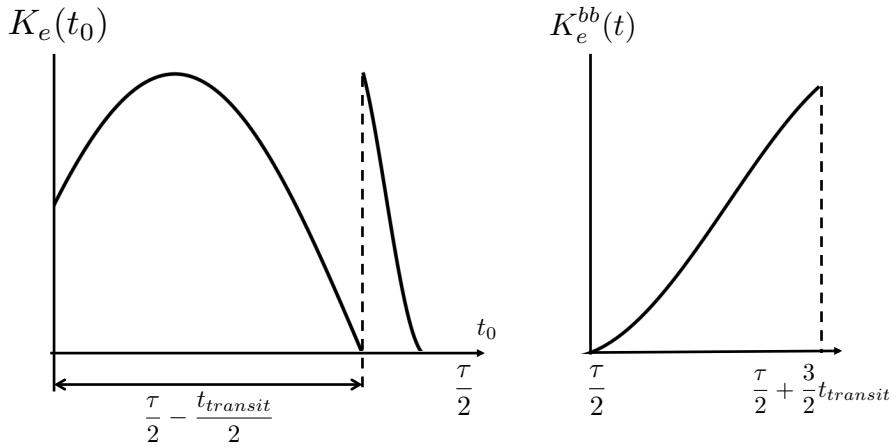

Figure 20: Left: Kinetic energy as a function of injection time using the linear average velocity for the effective velocity. Right: Kinetic energy deposited on the cathode as a function of time using the linear average velocity.

Note that the maximum energy deposited on the cathode from this model does not occur for the particle that is emitted first. This may seem counterintuitive but due to the long transit time resulting from greatly underestimating the average particle velocity, the particles emitted first end up seeing a second sign change of the RF field before depositing their energy on the cathode. This is a good example of how using the linear average velocity will underestimate the real average velocity of particles in the gun.

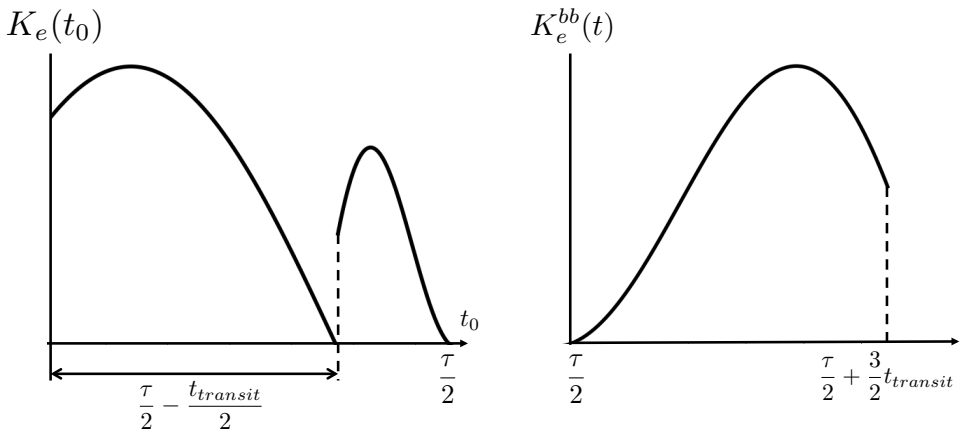

Figure 21: Left: Kinetic energy as a function of injection time using the velocity from the linear average energy for the effective velocity. Right: Kinetic energy deposited on the cathode as a function of time using the velocity from the linear average energy for the effective velocity.

These results, as with before, can be compared to the numerical solution to the equations of motion, given by Figure 22.

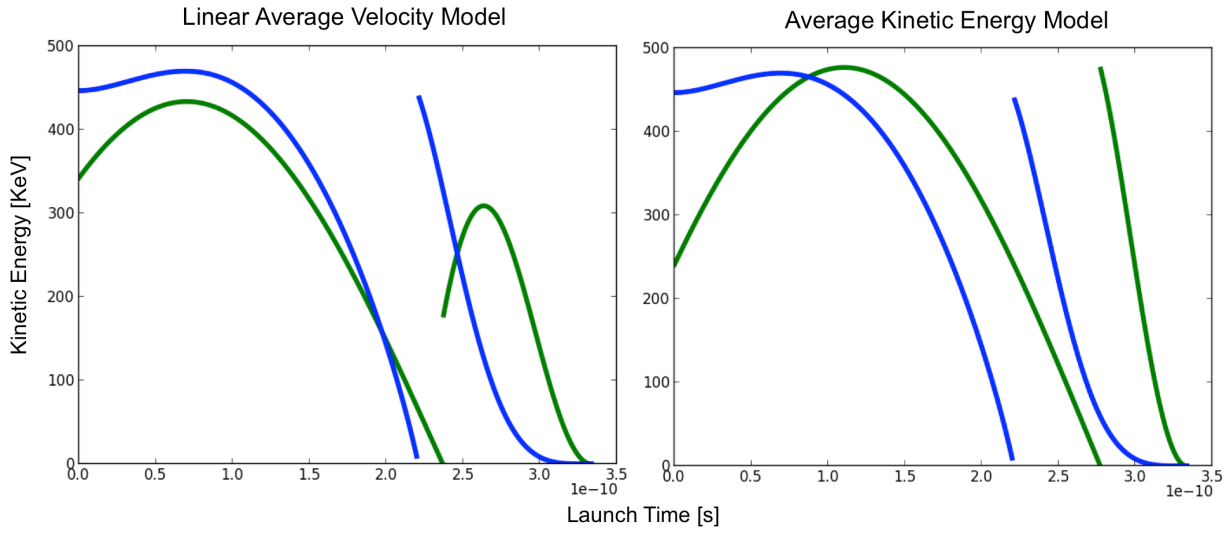

Figure 22: Comparison of numerical solution to relativistic equations of motion (Blue) with the results given on the right side of Figure 21 (left green) and Figure 22 (right green). The peak field was 20MV/m, the RF frequency was 1.0 GHz, and alpha was 8 for this comparison.

This shows that the linear average velocity model predicts more accurately predicts the shape of the beam that exits the cavity than the previous models. However the back-bombardment region

of this model (left side of figure 22) has a much poorer comparison to the numerical calculations. The average energy case better predicts the shape of the back-bombardment region. Because the area under the curve is the important factor when computing the back-bombardment power it is possible that the average velocity case still predicts the back-bombardment power with reasonable accuracy. Integrating the right side of Figures 20 and 21 gives the kinetic energy deposited on the cathode per RF period,

(23)

$$K_e^{dep} = \frac{E_0 v_{eff}}{4\pi^2 f^2}\left(3\sin\left(\frac{c\pi}{v_{eff}\alpha}\right) - \sin\left(\frac{3c\pi}{v_{eff}\alpha}\right)\right)$$

Multiplying the kinetic energy deposited per RF period by the beam current and the RF frequency gives the time average back-bombardment power Equation 24,

(24)

$$P_{ave} = \frac{IE_0 v_{eff}}{4\pi^2 f}\left(3\sin\left(\frac{c\pi}{v_{eff}\alpha}\right) - \sin\left(\frac{3c\pi}{v_{eff}\alpha}\right)\right)K$$

Figures 23-25 show the comparison of Equation 24 to the simulation data over a representative range of parameters. As before the variation with alpha and frequency are given first. This comparison shows a decent agreement between the simulation and the analytical model. Similar issues occur as the previous section for short gap lengths. For the variation with fractional gap length and frequency, the average velocity case is better for the pillbox cavity while the velocity from the average energy is better for the field map case. This is also the case for the variation of back-bombardment with the peak field, shown in Figure 25. Note that Equation 24 preserves the linear relationship with field and the rational relationship with frequency while the relationship to alpha is significantly different. This can be seen by close inspection of Figure 24, however the

variation in the slopes in Figure 25 show how using the sinusoidal field model greatly changes the predicted variation with the fractional gap length as compared to Figure 14.

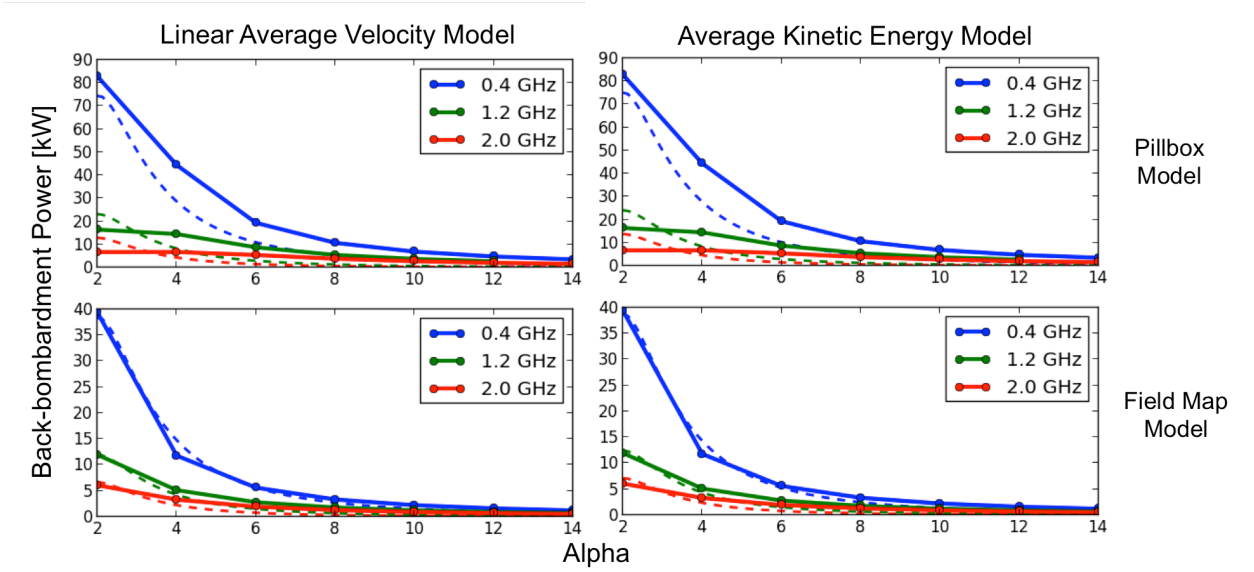

Figure 23: Comparison of Equation 24 and simulation as a function of frequency for three values of alpha. The peak field was 20MV/m for this comparison.

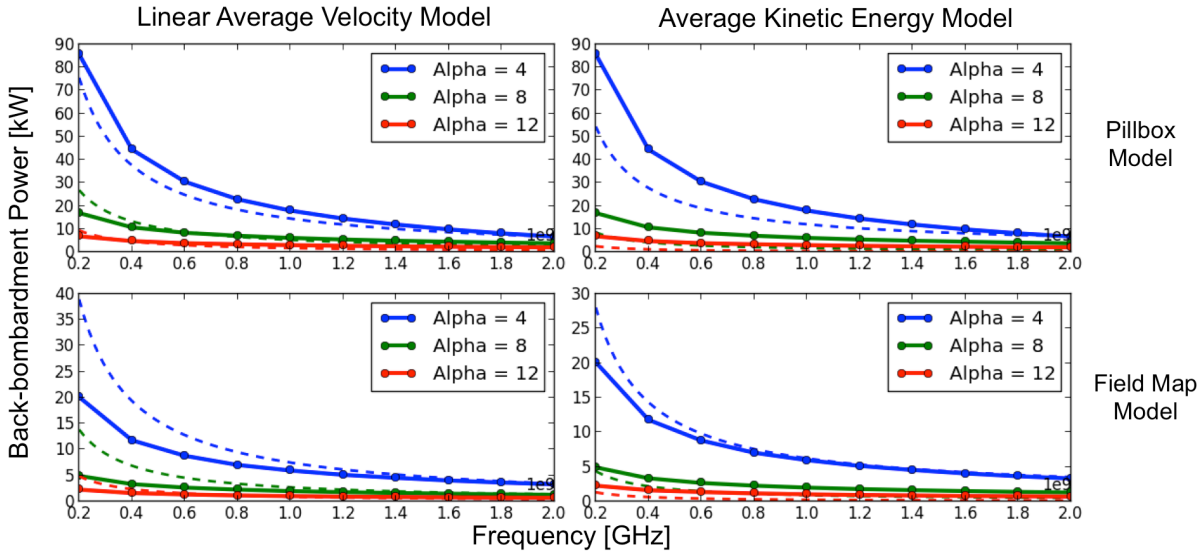

Figure 24: Comparison of Equation 24 and simulation as a function of alpha for three values of frequency. The peak field was 20 MV/m for this comparison.

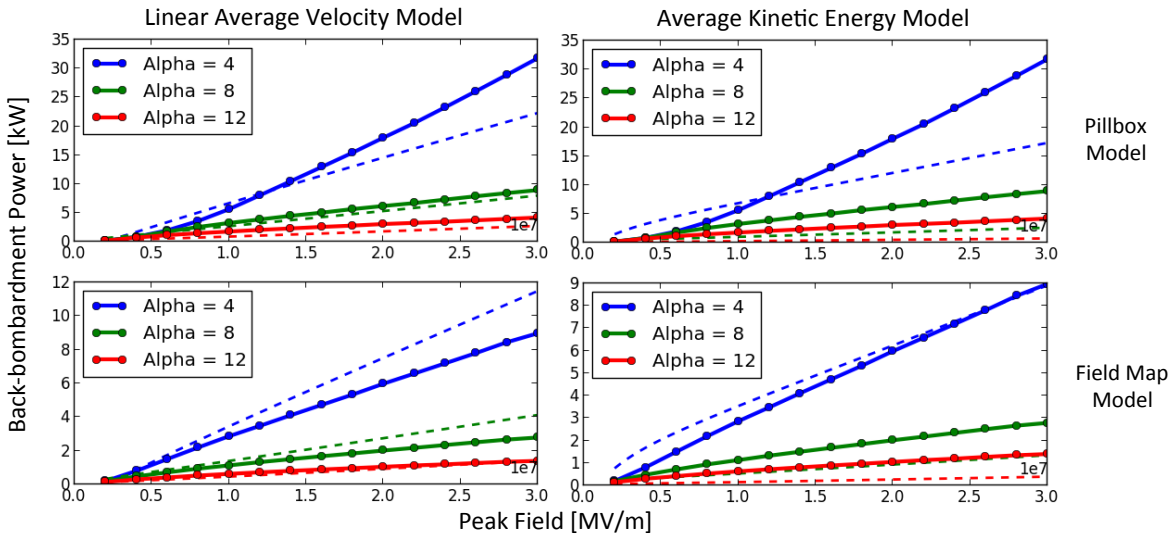

Figure 25: Comparison of Equation 24 and simulation as a function of the peak field in the cavity for three values of alpha at a frequency of 1 GHz.

2.5 Comparison analysis of models

While a visual inspection of the different models compared with simulation provides some intuition as to how well they predict the back-bombardment power it is necessary to have a quantitative analysis of these models to truly determine which method best approximates the back-bombardment power. This section compares all of the techniques analyzed in this chapter and determines under what conditions the model is no longer accurate. Using the best model to predict the back-bombardment power for some published measured data concludes this chapter.

2.5.1 Comparison of back-bombardment prediction

Using the simulation data and the developed theory to predict the back-bombardment power, the magnitude of the difference between simulation and the theory $D(\alpha, f, E_0) = |P_{ave}(\alpha, f, E_0) - P_{simulation}(\alpha, f, E_0)|$ was calculated for the simulation data obtained by varying alpha from 2 to 14 in increments of 2, varying frequency from 200 MHz to 2 GHz in increments of 200 MHz,

and by varying the peak field from 2MV/m to 30MV/m in increments of 2 MV/m. Table 1 gives statistics for $D(\alpha, f, E_0)$ for the pillbox cavity using both the square wave field and the sinusoidal field, for each of the three techniques used to calculate the effective velocity (speed of light, average energy, linear average velocity).

Table 1: Root mean squared (RMS) difference, normalized RMS difference, average difference, and peak difference of the respective analytical models and the simulation data for the pillbox cavity field profile.

Square Wave				
	D_{rms} [W]	D_{rmsn}	D_{ave} [W]	D_{peak} [W]
Speed of Light Velocity	277	0.00206	4080	118000
Average Energy	271	0.00206	3720	118000
Linear Average Velocity	930	0.00105	7450	390000
Sine Wave				
	D_{rms} [W]	D_{rmsn}	D_{ave} [W]	D_{peak} [W]
Speed of Light Velocity	366	0.00180	5360	159000
Average Energy	358	0.00180	4740	160000
Linear Average Velocity	917	0.000949	6880	387000

These data show that the linear average velocity is much poorer at predicting the back-bombardment power using either the sine wave or the square wave. The normalized RMS is slightly lower using the linear average velocity as compared with the other techniques, however this is likely due to the large increase in the peak difference using the linear average velocity. The difference in the statistics between using the speed of light velocity or the average energy velocity is not significant enough to say definitively that one method is better than the other for computing the back-bombardment power in the pillbox cavity. There are slight differences between the square wave temporal field profile and sinusoidal field profile; however, the differences are not significant enough to state that one model is better than the other. This is likely because the transit time factor was used to effectively add back in the time varying

component of the field. The same statistics were computed for the field map simulations, these are given in Table 2.

Table 2: RMS difference, normalized RMS difference, average difference, and peak difference of the respective analytical models and the simulation data for the short gap cavity field profile.

Square Wave				
	D_{rms} [W]	D_{rmsn}	D_{ave} [W]	D_{peak} [W]
Speed of Light Velocity	77.2	0.00229	1180	17600
Average Energy	80.3	0.00228	1370	18100
Linear Average Velocity	389	0.000439	4920	144000
Sine Wave				
	D_{rms} [W]	D_{rmsn}	D_{ave} [W]	D_{peak} [W]
Speed of Light Velocity	56.3	0.00229	1030	24700
Average Energy	55.2	0.00227	723	25500
Linear Average Velocity	366	0.000405	4010	142000

These data show that in general the model is much better at predicting the physics as compared to the pillbox cavity case. Additionally the sine wave has significantly better performance as compared to the square wave. As with before, the linear average velocity is the poorest technique for computing the back-bombardment power with the highest RMS, average, and peak difference between the theory and the simulation. The normalized RMS difference deceases for the linear average; however, this is likely due to the increase in the peak difference between the simulations and the theory.

Tables 1 and 2 show that across the entire dataset the RMS, and normalized RMS, difference between the theory and the simulation is quite low, indicating that in general the model predicts the physics. However, large average and peak differences indicate that there are some regions where the model does not agree well with the simulation. Analysis of how the difference function varied with respect to the cavity parameters showed that no one variable determines whether the error will be low or not. Therefore the parameter, $\psi = \alpha f/E_0 = c/V_{gap}$, was

introduced. Here V_{gap} is the gap voltage of the gun defined by $V_{gap} = E_0 L_{gap}$. Observation of how the difference between simulation and theory varies as a function of ψ showed that $D(\alpha, f, E_0) \propto 1/\psi = V_{gap}/c$, with a sharp increase in D for $\psi > 200$. This indicates that designs with $\psi < 200$ will not agree as well with the theory derived. In other words, the error will increase drastically for designs with a gap voltage less than 1.5 MV. This is because for low voltage cases the particle velocities are quite low and varying with time making the constant velocity approximation no longer adequate. Tables 3 and 4 shows the same statistics as Tables 1 and 2, excluding designs with $\psi < 200$.

Table 3: RMS difference, normalized RMS difference, average difference, and peak difference of the respective analytical models and the simulation data for the pillbox cavity case for designs with $\boldsymbol{\psi < 200}$.

Square Wave				
	D_{rms} [W]	D_{rmsn}	D_{ave} [W]	D_{peak} [W]
Speed of Light Velocity	112	0.00887	2070	13600
Average Energy	101	0.00824	1670	13400
Linear Average Velocity	72.7	0.00674	1240	8870
Sine Wave				
	D_{rms} [W]	D_{rmsn}	D_{ave} [W]	D_{peak} [W]
Speed of Light Velocity	132	0.00987	2830	10900
Average Energy	105	0.00831	2250	9050
Linear Average Velocity	48.4	0.00575	822	6790

Table 3 shows that by filtering out the low gap voltage cases the RMS difference decreases greatly for each modeling technique. Additionally the linear average velocity model transitions from being the poorest method of computing the effective velocity to being the best method for computing the effective velocity for the pillbox cavity case. This is likely because for low gap voltages the velocity is very low and constantly changing, while for higher voltage cases the velocity is more consistent. Additionally the square wave performs better when using the speed of light and the average energy technique while the sine wave is a better method when used in

conjunction with the linear average velocity. Table 4 shows the comparison of the field map model with simulation for designs with $\psi < 200$ removed. This gives a slightly different overall picture of the theory performance.

Table 4: RMS difference, normalized RMS difference, average difference, and peak difference of the respective analytical models and the simulation data for the field map case for designs with $\boldsymbol{\psi < 200}$.

Square Wave				
	D_{rms} [W]	D_{rmsn}	D_{ave} [W]	D_{peak} [W]
Speed of Light Velocity	30.8	0.00531	440	5130
Average Energy	30.4	0.00517	588	4580
Linear Average Velocity	69.8	0.00655	1390	8770
Sine Wave				
	D_{rms} [W]	D_{rmsn}	D_{ave} [W]	D_{peak} [W]
Speed of Light Velocity	32.8	0.00510	753	3730
Average Energy	15.9	0.00500	333	2670
Linear Average Velocity	46.1	0.00563	894	6180

Here the sine wave analysis is comparable for the speed of light velocity, and better for both the average energy as well as the average velocity case. The average energy method performs the best using the sine wave analysis.

While the pillbox cavity is a good approximation for many applications the field map case will more closely resemble reality for a wide range of gun geometries. As a result, the model that compares best with the field map data is used as baseline analytical model for predicting back-bombardment power. This model uses the sinusoidal field, and the effective velocity computed from the average energy.

2.5.2 Comparison of time domain prediction

Because the constant velocity approximation is being used, the phase boundary between particles that are back-bombarded and particles that exit the gun will vary depending on which model is

used. In some cases the phase boundary is a useful metric independent of the back-bombardment power. In this section we compare the theoretical prediction of the phase boundary with the numerical result computed using the relativistic equations of motion. Using the constant velocity assumption, the theoretical prediction of this boundary is dependent completely on the particle transit time. The theoretical phase boundary is computed by

(25)

$$\phi_{bb} = 180\left(1 - \frac{1}{\alpha\beta}\right).$$

Here $\beta = v_{eff}/c$, and α is the fractional gap length. The value of β is determined by the different techniques for calculating the effective velocity in the gun. This is done for the speed of light method, the velocity of the average energy particle, and the linear average velocity. The back-bombardment phase boundary was computed over the same range of parameters as the simulation data, and the difference between the actual value and the theoretical value was computed, $D(\alpha, f, E_0) = |\phi_{bb}(\alpha, \beta) - \phi_{bb}^{numerical}|$. Table 5 provides some statistics for this difference function.

Table 5: Average difference, maximum difference, and peak difference between analytical and numerical solution for the back-bombardment phase boundary.

	D_{ave}	D_{peak}	D_{min}
Speed of Light Model	34	80	0.36
Average Energy Model	27	250	0.049
Average Velocity Model	30	405	0.10

These data show that on average each model has about 30 degrees of error in the back-bombardment phase boundary. This is quite significant; however, both the average energy and average velocity models have very large peak errors. These are associated with designs that have small values of alpha, and small peak fields. There is a slight correlation between both alpha and

the peak field, and $D(\alpha, f, E_0)$. This can be seen in Figure 26. Figure 26 shows the $D(\alpha, f, E_0)$ as a function of both peak field (left) and alpha (right).

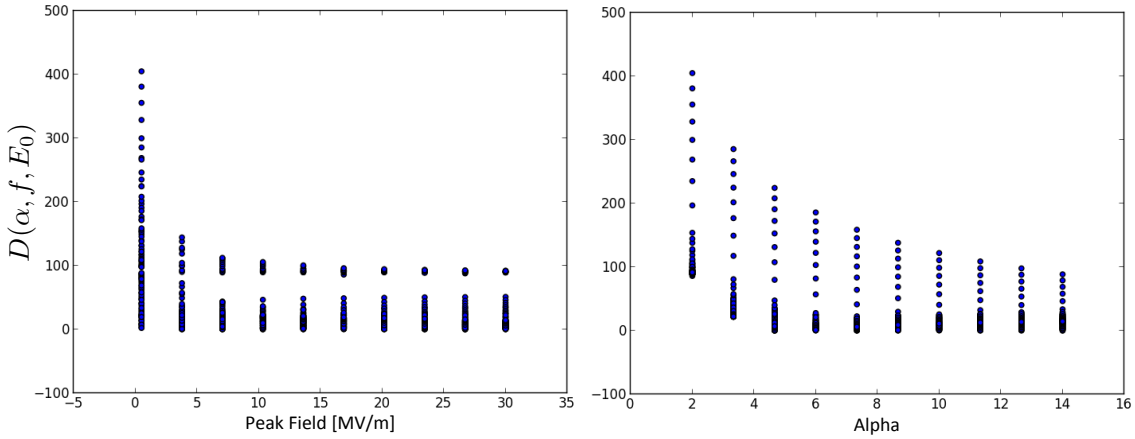

Figure 26: Difference between the predicted back-bombardment phase boundary and the numerical result ($D(\alpha, f, E_0)$) as a function of E_0 (Left), and α (Right).

Here we see that there is a strong correlation between peak field $D(\alpha, f, E_0)$. In other words cases with the largest error are all for cases with the smallest peak field. It was well established in the previous section that guns with a low peak field will not agree as well when computing the back-bombardment power because the constant velocity approximation is not sufficient. Because the constant velocity approximation is used to compute the phase boundary the same issues arise here. Additionally the largest peak errors occur for the long gap lengths. In order to determine how well the phase boundary can be computed, designs with $\alpha < 4$ and $E_0 < 5MV/m$ are filtered out and a the difference function is plotted again, Figure 27.

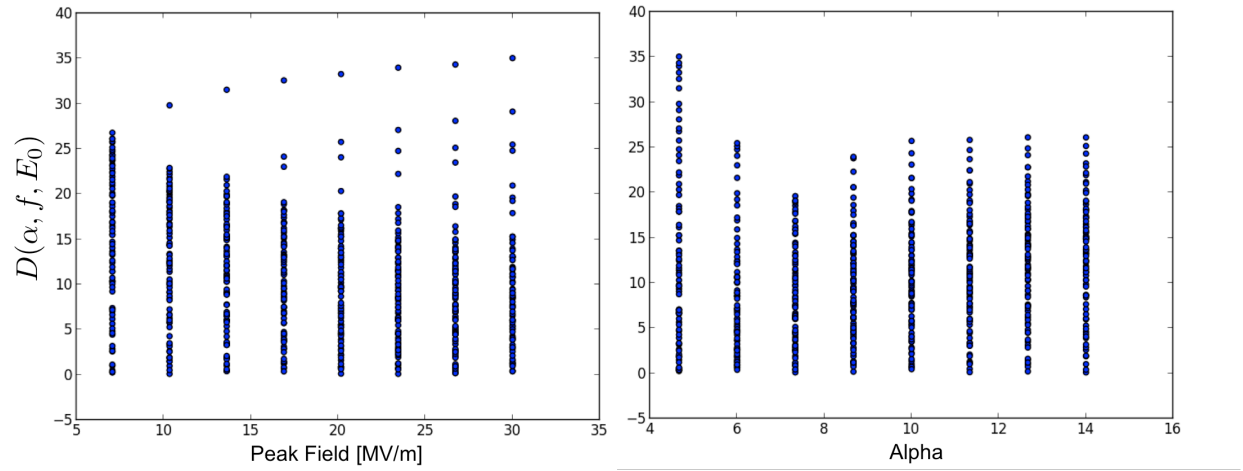

Figure 27: $\boldsymbol{D(\alpha, f, E_0)}$ as a function of $\boldsymbol{E_0}$ (Left), and $\boldsymbol{\alpha}$ (Right) with low field and low alpha designs removed.

This shows that by removing the outliers (designs with low peak field and low alpha) there is now very little visible correlation between the difference function and either alpha or peak field. Because there we have removed cases with very large peak error, these outliers will no longer weight the average so heavily. Table 6 shows the same statistics as Table 5 but with values of alpha less than 4 removed and peak fields less than 5 MV/m removed. While the statistics for the average energy case and the speed of light case are still roughly the same, except for the peak value being much lower, the linear average velocity model has significantly improved its ability to predict the phase boundary.

Table 6: Average difference, maximum difference, and peak difference between analytical and numerical solution for the back-bombardment phase boundary. Designs with values of $\alpha < 4$ and $E_0 < 5MV/m$ are removed.

	D_{ave}	D_{peak}	D_{min}
Speed of Light Model	33	74	3.5
Average Energy Model	26	48	3.5
Average Velocity Model	11	35	0.10

This shows that for computing the phase boundary of back-bombardment particles, the linear average velocity is best, but only under certain conditions. In general assuming a constant

velocity makes it difficult to accurately compute the boundary over a wide range of operating parameters. If an estimate is desired, the linear average velocity is best for designs with alpha greater than 4 and peak field greater than 5MV/m.

2.5.3 Comparison to measurement

The detailed comparison of the analytical results with the simulation results shows in general some very good comparisons. While this exercise is very valuable in the development of new analytic models it is necessary to benchmark these comparisons against some measured data where possible. A limited amount of data is available for back-bombardment power; however, one group did an experimental study of back-bombardment effects and these can be compared to the theory developed in this chapter.

The facility at the Institute of Advanced Energy in Japan [16] has a 4.5-cell gun operating at 2.85835 GHz. The particular experiment in question was run with a beam current of 500mA and a final energy of 4MeV. The gun was run in pulsed mode with a pulse length of 3μs and a repetition rate of 10Hz. These parameters do not give all information needed to predict the back-bombardment power, however using this information and some modest assumptions all the relevant parameters can be derived. The first derived parameter is the relative gap length. It is safe to assume that the first cell has an alpha of 4 at a maximum. It is likely longer, and therefore a lower alpha, but this information was not available from the paper. An alpha of 4 puts a lower bound on the back-bombardment power prediction. The second derived parameter is the peak field in the cell. While this was not given explicitly, the peak field can be calculated using the final kinetic energy and the length of the gun. 4.5 cells at 2.85835 GHz correspond to a gun length of approximately, 23.6 cm. With a final energy of 4 MeV, the average peak field in the

gun is approximately 17MV/m. Using the derived peak field, derived alpha, beam current, and frequency, the back-bombardment power for CW operation was calculated to be 46kW using Equation 24. However, the experiment was run pulsed with a low repetition rate. In order to account for this difference, the back-bombardment power must be scaled by the total amount of operational time per second. For a 3-microsecond pulse at 10Hz the scaling from CW mode to pulsed mode is $3x10^{-5}$, bringing the predicted back-bombardment power down to 1.4W. This assumes a K value for the experiment of 1, which is quite unrealistic for a real gun. A modest estimate of the K value is 0.75. Applying this to the back-bombardment power gives a predicted value of 1.0W. The experimental result published indicated a back-bombardment power of about 0.6W, which is slightly lower than the prediction. This is actually quite close considering the number of unknowns when comparing the two results and gives as quoted, better than an order of magnitude accuracy in computing the back-bombardment power with experimental values.

3. Space-charge effects on Back-bombardment in Single-cell Guns

In Chapter 2 the discussion was limited to beams that do not have any significant space-charge effects. However, for gun designs with high currents, space-charge forces will be far from insignificant and therefore it is necessary to study how the inclusion of space-charge forces will impact the back-bombardment process. This chapter begins with a simulation-based analysis that will develop intuition as to how the space-charge effects impact back-bombardment. This is followed by the development of simple analytical models that describe how the longitudinal space-charge field and the transverse space-charge field affect the back-bombardment process. The space-charge terms are then added into the equation for back-bombardment power and compared with simulation results.

3.1 Simulation of space-charge effects in a short gap gun

In this section the gun design used in the beginning of Chapter 2 was simulated under a wide range of beam currents in order to develop an intuitive understanding of how space-charge forces impact the back-bombardment process. Three simulation scans were run at a constant bunch charge while varying the frequency. Here the bunch charge is defined as the charge emitted per RF period. Because the frequency is being varied with a constant emitted charge per period, there is effectively an increase in the current density being output by the cathode. Space-charge forces are generally governed by the current density and therefore increasing the current density will increase the space-charge forces in the beam. Figure 28 shows the back-bombardment power as a function of frequency for three different bunch charges. While in the previous chapter the frequency and current were both shown to be independent variables of the back-bombardment, the dominating factor here is that by increasing the frequency the current is also increasing.

When comparing the theory developed in this chapter with these simulations the variation with frequency is included as well as the space-charge forces. While these initial simulations do not fully decouple the space-charge effects from the other varied parameters, they provide a starting point for studying how space-charge effects impact this process.

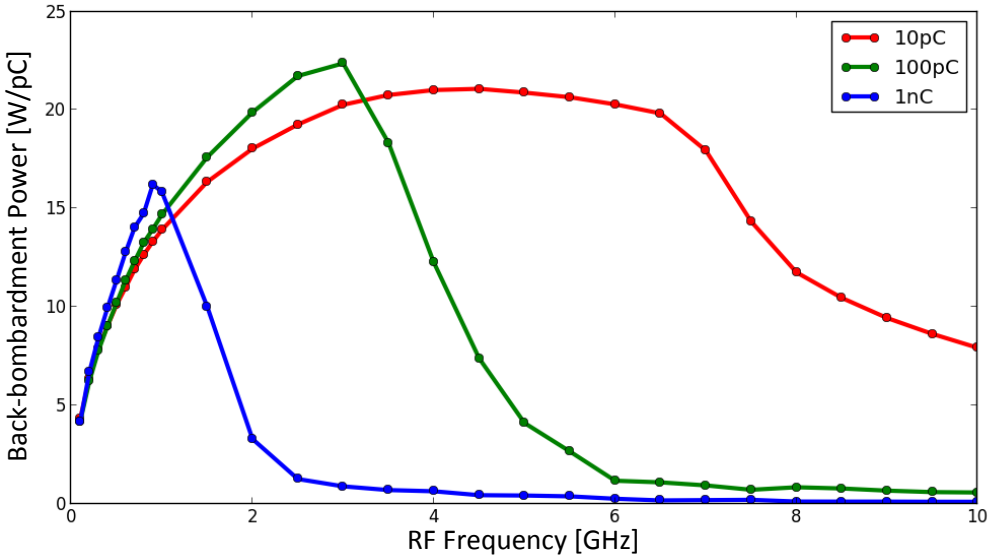

Figure 28: Back-bombardment power, normalized to the bunch charge, as a function of frequency for three bunch charges.

This shows that as the frequency increases the back-bombardment power steadily increases, followed by a sharp decrease and settling out to near zero. Because there is a constant bunch charge emitted per RF period, the increase in frequency corresponds directly to an increase in the current density. The previous chapter showed that the back-bombardment power is inversely proportional to the frequency; therefore, it is reasonable to state that this curve is dominated by the space-charge forces. In order to confirm that space-charge is the dominating factor, Child's law (Equation 26) can be used to predict the space-charge limiting current for a particular bunch charge as a function of frequency. Because the gun design has a short gap length and a transit

time factor of 0.96 it is operating as a quasi-dc gun which supports the use of Child's law as it is derived for DC guns.

(26)

$$J = \frac{4\epsilon_0}{9}\sqrt{\frac{2q}{m_0}}\frac{V^{\frac{3}{2}}}{d^2}$$

Here J is the output current density from the cathode, V is the gap voltage, d is the gap length, ϵ_0 is the permittivity of free space, q is the fundamental unit of charge, and m_0 is the mass of an electron. The effective frequency of the space-charge limit can be computed by making a few substitutions. The current density J is defined as the current per unit area on the cathode $J = I_c/A_c$. The current I_c is defined by the bunch charge divided by the emission time which is one half an RF period, $I_c = 2Qf$. The cathode area is written in terms of the cathode radius, which scales with frequency as well, by $A_c = \pi\, r_c^2$, where $r_c = r_0 f_0/f_{scaled}$. For these simulations r_0 is 2 cm, and f_0 is 100MHz. The gap voltage can be expressed in terms of the peak field and the gap length by $\mathrm{V} = E_0\lambda/10$, and in terms of frequency $V = E_0\, c_0/\,(10f)$. Additionally the gap length d is given in terms of the RF frequency by $d = c/(10f)$. Substituting all of these parameters into Child's law and solving for the frequency gives the effective space-charge limiting frequency for a constant emitted charge,

(27)

$$f_{scl} = \left(\frac{2\epsilon_0}{9}\sqrt{\frac{2q}{m_0}}\frac{100\pi r_0^2 f_0^2}{Qc^2}\right)^{\frac{2}{5}}\left(\frac{E_0 c}{10}\right)^{\frac{3}{5}}.$$

Note that Equation 27 was derived for the geometry given by Figure 2. This geometry had a fractional gap length α equal to 10. By substituting in α instead, a more general equation that can be applied to any gap length is given by Equation 28. Care must be taken when applying this

equation to longer gap lengths. The primary reason why Child's law is appropriate for these simulations is the high transit time factor and short gap length for the specific gun design in question. Guns with a longer gap length and a lower transit time factor do not behave as a quasi-DC gun and Child's law would not be appropriate for estimating the space-charge limiting frequency.

(28)

$$f_{scl} = \left(\frac{2\epsilon_0}{9}\sqrt{\frac{2q}{m_0}}\frac{\alpha^2\pi r_0^2 f_0^2}{Qc^2}\right)^{\frac{2}{5}}\left(\frac{E_0 c}{\alpha}\right)^{\frac{3}{5}}.$$

The result of this equation was used to predict the space-charge limiting frequency for the particular gun configuration in the simulations and is shown by the solid vertical lines in Figure 29. The dashed vertical lines shown in Figure 29 represent a numerical solution to child's law for a given gun configuration [34].

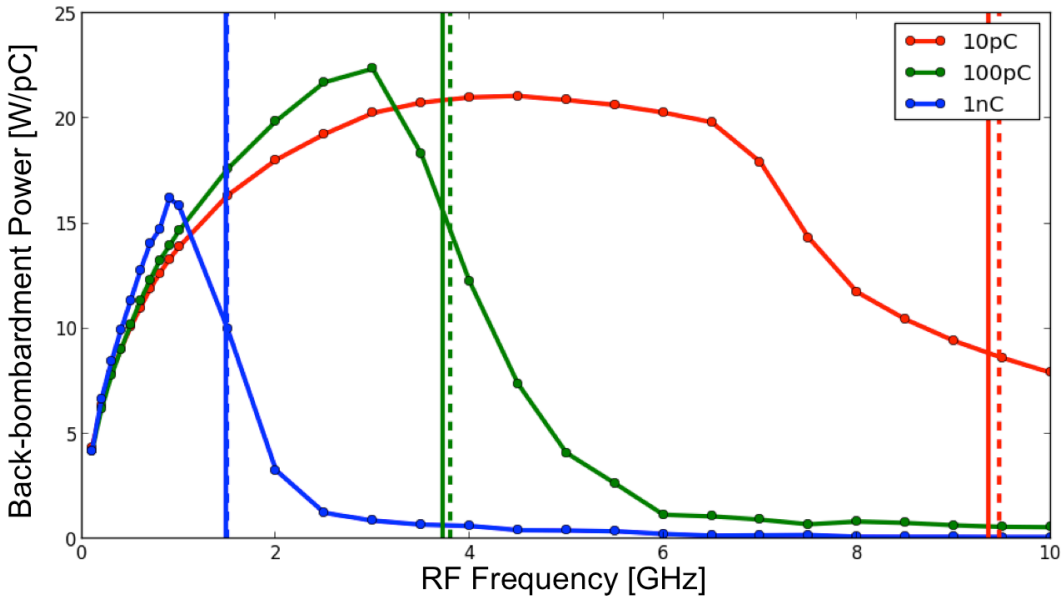

Figure 29: Back-bombardment power, normalized to the bunch charge, as a function of frequency for three bunch charges. Vertical lines indicate space-charge limit predictions using equations 26 and 27 [34].

As expected the exact solution and the numerical solution agree very well and lie within the transition region between normal and space-charge limited operation. However we know from the previous section that for the field map case the gap voltage will be slightly lower due to the spatial variation in the field. In order to correct for this, the field normalization factor used in the previous chapter was added into Equation 28 giving the result in Equation 29.

(29)

$$f_{scl} = \left(\frac{2\epsilon_0}{9}\sqrt{\frac{2q}{m_0}}\frac{\alpha^2\pi r_0^2 f_0^2}{Qc^2}\right)^{\frac{2}{5}}\left(\frac{KE_0c}{\alpha}\right)^{\frac{3}{5}}.$$

After applying the field normalization factor, the new space-charge limiting frequency can be calculated and compared with the simulations. Equation 29 was used to predict the vertical lines in Figure 30.

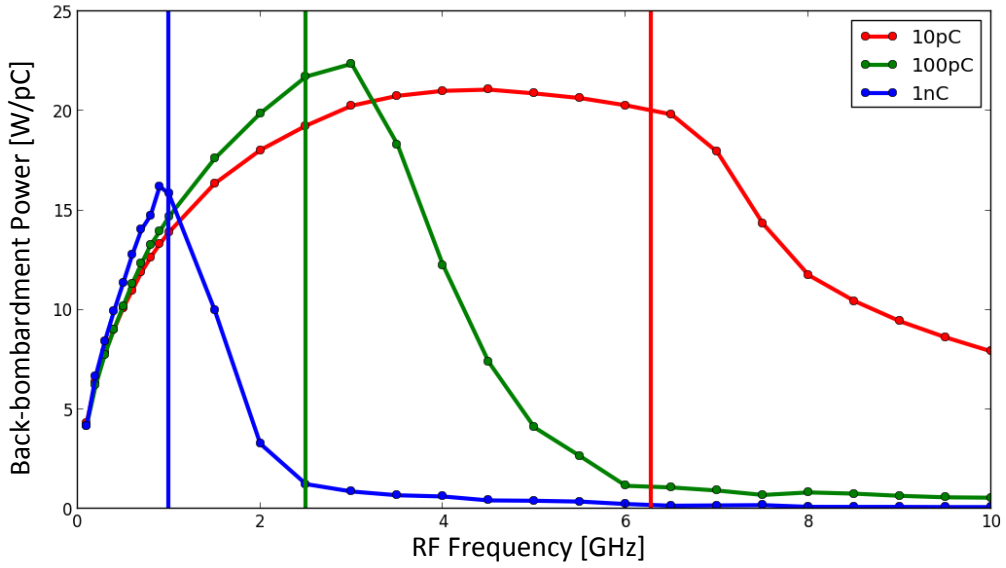

Figure 30: Back-bombardment power, normalized to the bunch charge, as a function of frequency for three bunch charges. Vertical lines indicate space-charge limit prediction using Equation 29.

This shows that the space-charge limit predicts the point in the curve where the back-bombardment power transitions from increasing to decreasing. This is a closer prediction to the exact location where space-charge effects take over instead of Equation 28 that predicts the middle of the transition region.

In DC guns, the onset of space-charge-limited operation is accompanied by the formation of a potential minimum and virtual cathode. This occurs because of the attractive force generated by the image currents on the cathode. As the beam charge/current increases the attractive force of this image current decelerates the forward propagating beam. When the charge/current is sufficiently large the conditions will be met to decelerate the beam completely and draw some current back towards the cathode. The location where the current is zero is the potential minimum and the back-streaming current due to the attractive force of the image currents creates a virtual cathode. This is expected to increase the number of electrons returning to the cathode [7]; however, Figures 28-30 show that the onset of space-charge brings with it a decrease in the back-bombardment power.

At first glance this seems counterintuitive, but it could be explained by the fact that not all back-bombardment electrons will have the same energy when arriving at the cathode. It was shown in the previous chapter that the back-bombarded electrons that gain the most energy from the RF field are those that make it almost all the way across the gap before reversing direction. These electrons have the longest distance to travel through the RF field on their way back to the cathode and therefore are able to gain more energy than electrons that are caught in the potential depression and reverse direction close to the cathode surface. As this gun is operating in a quasi-

DC mode we look for a similar virtual-cathode effect here by analyzing the effective transmission coefficient (Equation 30) as a function of position along the gun. Sampling the frequency scan data in the emission-limited, transition, and space-charge-limited regions provided several test cases in which to look for this virtual cathode like depression. Selecting three values of emitted charge, for three different frequencies, generated the nine test cases. The transmission coefficient was then computed at 100 locations along the axis of the gun using the relation,

(30)

$$T_{pct} = \frac{N_{forward}}{N_{backward} + N_{forward}}.$$

Here (T_{pct}) is the transmission coefficient, ($N_{forward}$) is the total number of forward moving particles seen at a particular axial location, and ($N_{backward}$) is the total number of backward moving particles at the same location. The resulting transmission coefficient data are shown in Figure 31. This clearly shows that as the gun transitions into the space-charge-limited regime (highlighted in red), there is a virtual-cathode-like depression in the transmission coefficient. This occurs at approximately 10% of the distance across the gap. The transmission ratio (Equation 31) as a function of position along the gun is also computed.

(31)

$$T_{ratio} = \frac{N_{forward}}{N_{emitted}}$$

While the transmission coefficient shows explicitly the location of the virtual cathode the transmission ratio shows explicitly that as the beam becomes more space-charge limited, fewer particles are able to exit the gun. This also shows that as the gun becomes space-charge-limited the overall output power decreases. Note that for the 1-nC, 8-GHz case the transmission ratio

increases about half way across the gap. This is because only one RF period was selected for post processing. Particles still moving forward at the end of the previous RF period will continue to move forward at the beginning of the next RF period, and will therefore contribute to the numerator in Equation 31. However, because they were emitted in the preceding RF period, they will not contribute to the denominator in Equation 31, and as a result will artificially increase the transmission ratio. This was certified by analysis of the particle trajectory data.

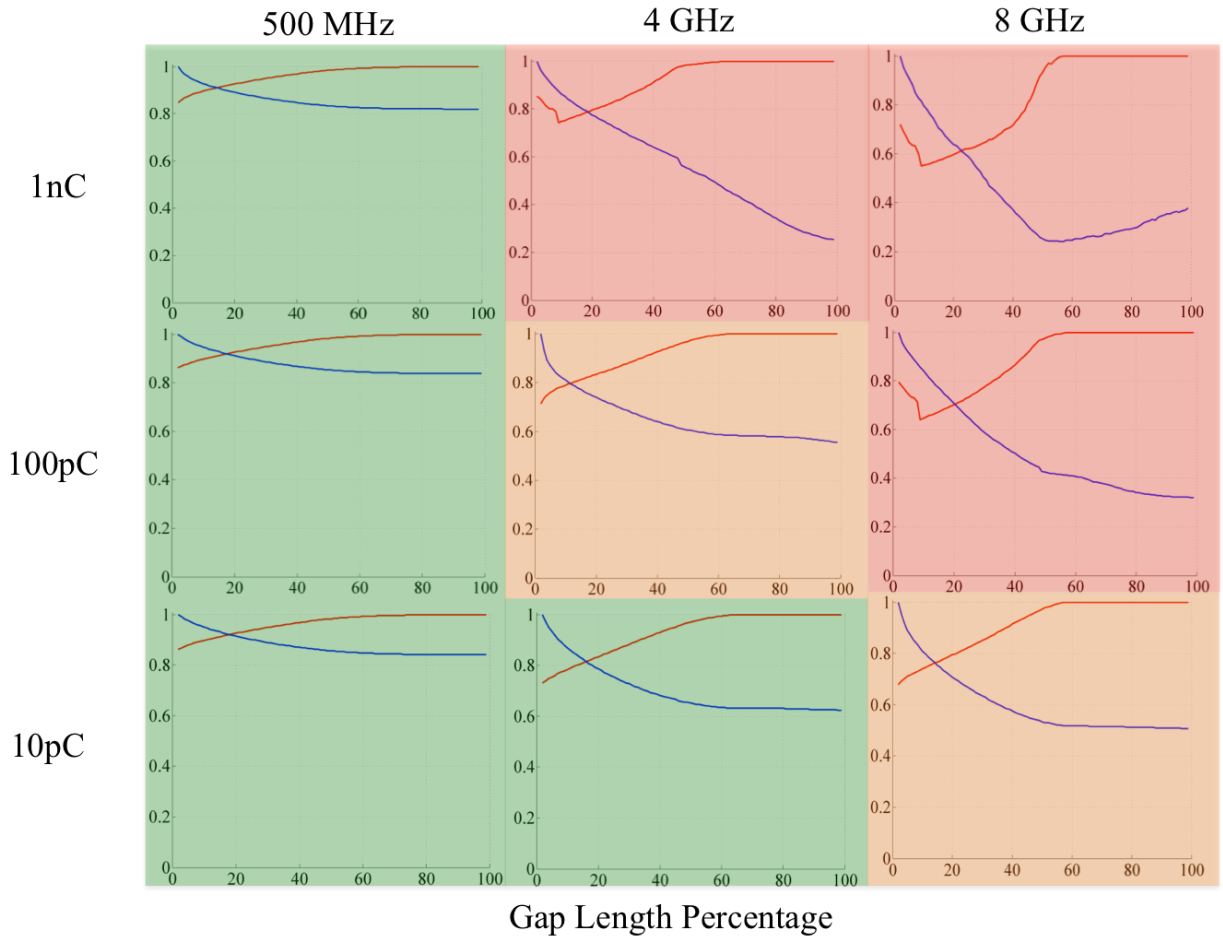

Figure 31: Transmission coefficient (red line) and Transmission ratio (blue line) of the gun as a function of position along the cavity axis, showing gun performance before (highlighted in green), during (highlighted in orange), and after (hightailed in red), the onset of space-charge effects [34].

For more information about how space-charge impacts back-bombardment, we examine the full particle trajectory information for a bunch charge of 100 pC and frequencies of 500 MHz, 4 GHz, and 8 GHz. This reveals how the gun transitions from the emission-limited regime to the space-charge-limited regime and gives context for the evolution of this process. Figure 32 shows four particle distribution snapshots in (r, z) space corresponding to RF phases of 90°, 180°, 270°, and 360° for each frequency. For the 500-MHz case the gun is operating in the emission-limited regime. This translates to a well-defined beam for the first two snapshots, which breaks up as the field reverses sign. At 4 GHz the gun is in the transition region between emission-limited and space-charge-limited operation. At 90° the virtual-cathode like effect is clearly seen, and in all cases a stronger radial defocussing is present due to the larger space-charge force induced by the higher beam current. In the 8 GHz gun the axial beam propagation is limited even further, and the radial defocussing of the beam due to space-charge is much more pronounced. Additionally the beam never becomes well developed and is now impacting the beam pipe. It is also important to note that backward propagating particles are present for 8 GHz at an RF phase of 180°; since the field has not yet reversed sign, these back propagating electrons are being "emitted" from the formation of the virtual cathode. Additionally it is important to note that radial space-charge forces deflect some backward streaming particles away from the cathode surface. These are not recorded as back-bombardment power as they do not strike the cathode surface. This is further support that space-charge is a fundamental factor in the back-bombardment process at high current.

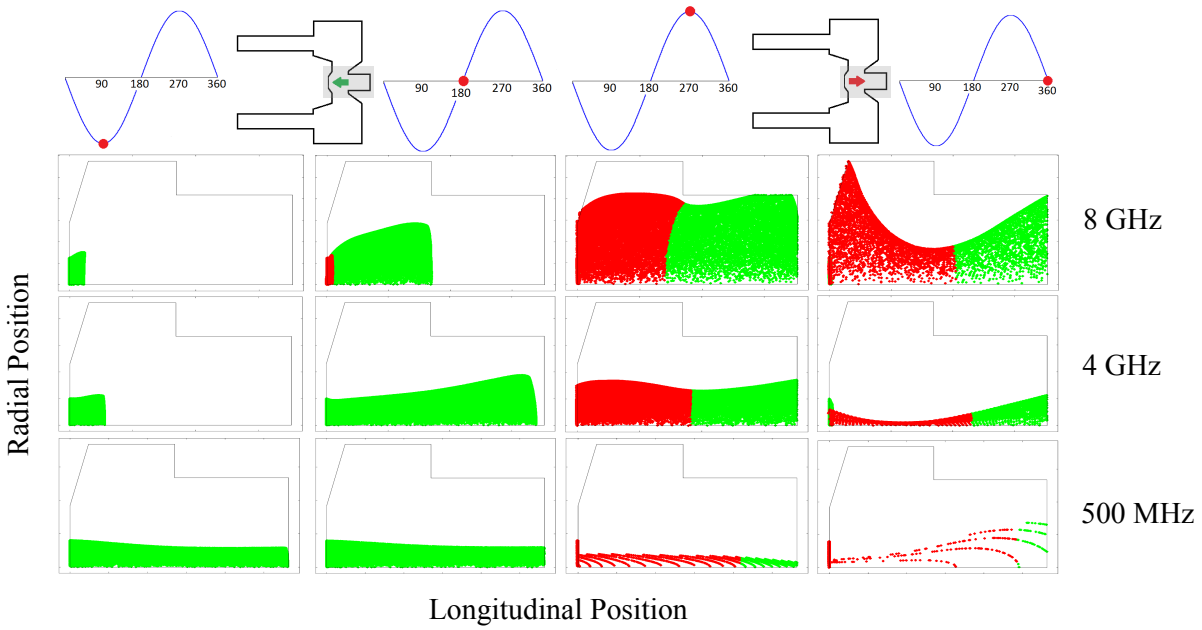

Figure 32: Snapshots of the particle distribution in (r, z) space at four time slices relative to the RF period occurring at 90°, 180°, 270°, and 360° for each frequency with a charge of 100pC. Forward propagating particles are indicated in green and backward propagating particles are indicated in red. The key above each column indicates the relative RF phase of the fields during the snapshot by a red dot on the sinusoidal wave, the region of the geometry where the particles are located is indicated by the grey box, and the field polarity is indicated by either a green or a red arrow representing acceleration or deceleration respectively. [34]

This has shown in a qualitative way that the longitudinal space-charge forces impact the back-bombardment process, but does not completely explain how the both longitudinal and transverse forces combined impact back-bombardment. Additionally this discussion has been limited to the analysis of simulation results without any discussion of analytical models derived from first principles. The development of a first principles model that also predicts these trends would provide significant support to the conclusions drawn about how space-charge forces impact the back-bombardment process.

3.2 A model for space-charge behavior

The development of a first principles model for the space-charge forces in the gun is split into two categories, the longitudinal space-charge force and the transverse space-charge force. While these two categories are not totally decoupled, they will initially be explained independently and then some coupling will be introduced later on. The longitudinal space-charge force impacts the back-bombardment process by decreasing the total effective accelerating field. The field created between the charge and image charge creates a field that partially cancels out the accelerating field and this decreases the total energy that can be deposited on the cathode. This effect is what creates the space-charge limiting current used to explain the results in the previous section. The transverse space-charge force is simply the Coulomb repulsion created by many charged particles trying to occupy a small space. This changes the effective area over which the beam deposits energy on the cathode because some electrons that are back-bombarded will be deflected away from the cathode surface and will therefore not contribute to the cathode heating. Additionally this coulomb repulsion leads to the coupling between the transverse and longitudinal space-charge force because as the beam radius increases, the current density decreases, which decreases the field intensity of the longitudinal space-charge force. After discussing these forces independently they will be included into the back-bombardment model and compared to simulation results

3.2.1 Longitudinal space-charge effects

In order to calculate the effect of the longitudinal space-charge field on back-bombardment, a simple model for this field can be obtained through direct solution to Maxwell's equation for the electric field, Equation 32.

(32)

$$\nabla \cdot \vec{E}_{sc} = \frac{\rho_{sc}}{\epsilon_0}$$

The current density J_z is defined by $J_z = v_{eff}\rho_{sc}$ and can be used to determine the longitudinal charge density in the gun. Here v_{eff} is the effective velocity as defined by the previous chapter.

(33)

$$\rho_z = \frac{J_z}{v_{eff}}$$

Neglecting the variation in the charge density in the radial direction greatly simplifies Equation 32. Assuming that the current density along the gun is constant results in a charge density that will also be constant and only a function of the effective velocity, the beam current, and the cathode dimensions, Equation 34.

(34)

$$\rho_z = \frac{I}{v_{eff}\pi r_c^2}$$

Substituting Equation 34 into Equation 32 gives the space-charge field as a function of beam current and the cavity geometry (Equation 35).

(35)

$$E_{sc} = \int_0^{\frac{\lambda}{\alpha}} \frac{I}{v_{eff}\pi r_c^2 \epsilon_0}\, dz = \frac{I\lambda}{v_{eff}\pi r_c^2 \epsilon_0 \alpha}$$

Equation 35 predicts that the space-charge field will increase linearly with the beam current for a particular series of gun parameters. If the space-charge field and the applied field are additive, then the back-bombardment power will have a quadratic variation with the beam current. This means that as the current increases the back-bombardment power will steadily increase but the quadratic variation will cause a maximum, after which the back-bombardment power will

decrease. It is important to note that this equation does not take into account the space-charge limit and therefore may not give a quantitatively accurate depiction of the space-charge effect but it does provide a simplistic analytic model that can be used to explain exactly how the longitudinal space-charge forces impact back-bombardment.

3.2.2 Transverse space-charge effects

The transverse space-charge forces will impact back-bombardment by decreasing the effective area of the beam that impacts the cathode. This is caused by the transverse defocusing of the beam by the increasing space-charge forces. The transverse defocusing will also indirectly affect the longitudinal field by reducing the current density of the beam and consequently reduce the longitudinal space-charge field. A common approach to analyzing the transverse defocusing of a beam due to the space-charge forces can be done by considering a DC beam at a constant velocity (Equation 36).

(36)

$$\frac{d^2r(z)}{dz^2} = \frac{qI}{2\pi\epsilon_0 m_0 c^3 \gamma^3 \beta^3}\frac{r(z)}{R^2}$$

This represents the radial acceleration of the beam as a function of position for some particle with radial position less than the beam radius. Note that this method produces a result that is not self-consistent, that is the radial force does not decrease as a function of z, just the particle position increases. For a beam at constant velocity, Equation 37 can be substituted into Equation 36 to simplify the expression.

(37)

$$K = \frac{qI}{2\pi\epsilon_0 m_0 c^3 \gamma^3 \beta^3}$$

Making this substitution and solving the ODE for $r(z)$ gives (Equation 38).

(38)

$$r(z) = R\cosh\left(\frac{K}{R}z\right)$$

While Equation 38 could be used to calculate the effective back-bombardment area of the beam as well as used to compute the subsequent decrease in the longitudinal space-charge field, the equation is not self-consistent and it will over predict the impact of space-charge forces for high currents. It is possible to make an approximately self-consistent model using Equation 36 but allowing the beam radius to also vary with position. This gives the following nonlinear ODE

(39)

$$r(z)\frac{d^2r(z)}{dz^2} = K$$

In order to solve Equation 39, $r(z)$ is approximated as a quadratic equation, Equation 40.

(40)

$$r(z) \approx r_0 + A_1 z + A_2 z^2$$

Substituting equation 40 into equation 39, and assuming that $r'(0) = 0$ gives the result in Equation 41. Note that because we have assumed that $r'(0) = 0$, $A_1 = 0$ as a result.

(41)

$$2A_2 r_0 + 2A_2^2 z^2 - K = 0$$

This assumes that the constant A_2 does not vary significantly with position. Using the quadratic formula the gives A_2. Substituting this result into Equation 41 gives the approximate solution to the beam envelope for a beam with constant K.

(42)

$$r(z) \approx \frac{r_0}{2} + \frac{\sqrt{r_0^2 + 2Kz^2}}{2}$$

The two models in Equations 38 and 42 will likely be valid under different conditions. In order to get an understanding as to which will be a better approximation of the beam radius, Equations 38 and 42 were compared with numerical solutions to Equation 39. Figures 33 and 34 give these results for four values of K, (0.01, 0.05, 0.1, and 0.5). This represents a wide range of space-charge magnitudes and provides a fairly general comparison.

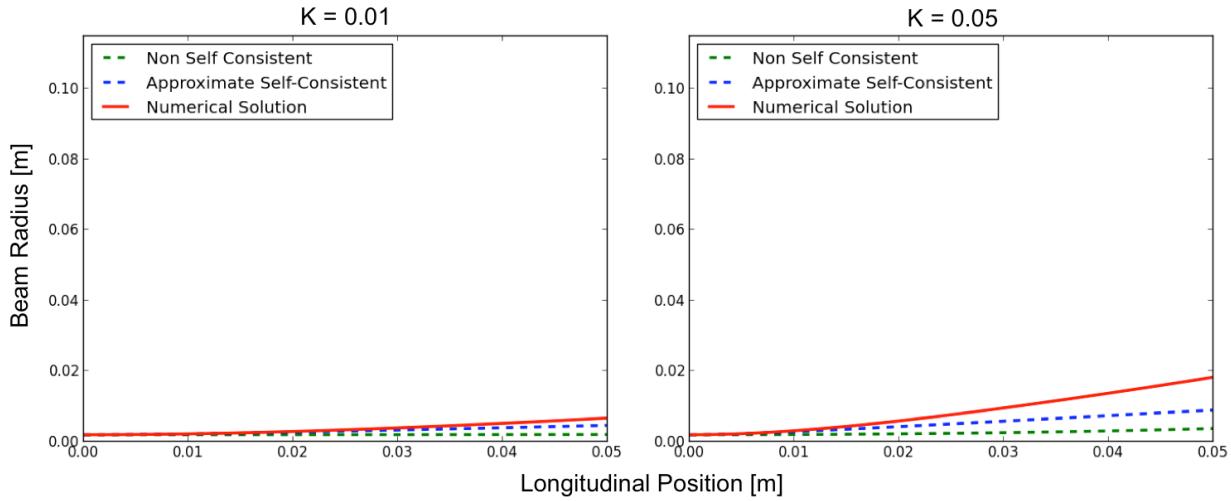

Figure 33: Comparison of numerical solution to Equation 39 (red) to Equation 42 (blue), and Equation 38 (green) for K=0.01 and 0.05. For these cases the fractional gap length was 6. The vertical axis is scaled to show the whole cavity for visual assessment of how much radial spreading is occurring due to space-charge.

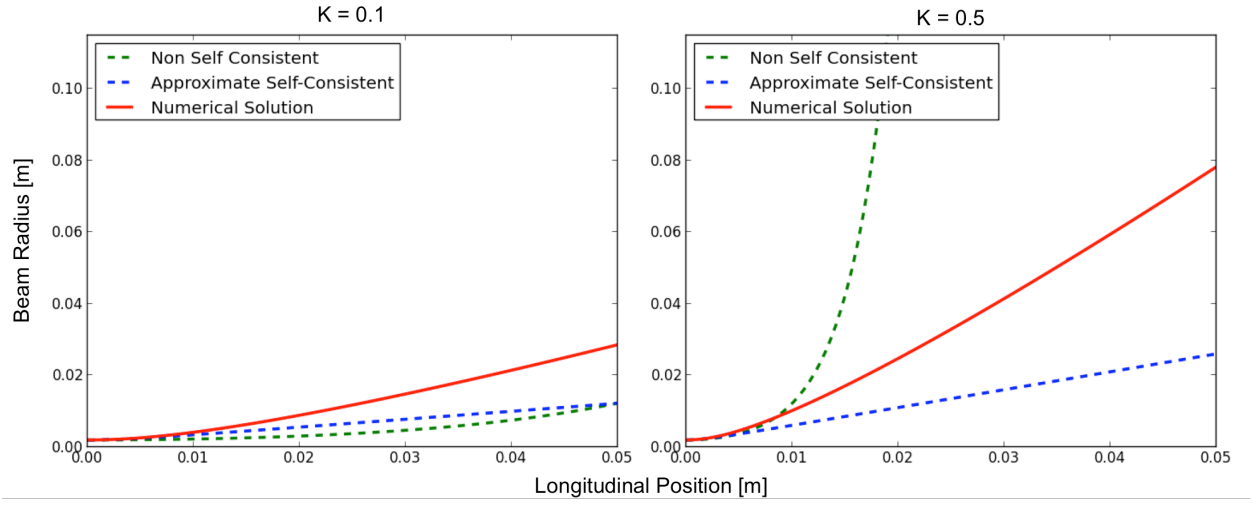

Figure 34: Comparison of numerical solution to Equation 39 (red) to Equation 42 (blue), and Equation 38 (green) for K=0.1 and 0.5. For these cases the fractional gap length was 6. The

vertical axis is scaled to show the whole cavity for visual assessment of how much radial spreading is occurring due to space-charge.

This shows that the self-consistent solution (Equation 42) is better than Equation 38 at predicting the beam radius as a function of position in almost every situation. In some cases where the space-charge is significant yet still modest (K~0.1), the beam radius at the end of the cavity is almost identically predicted by both Equations 38 and 42. For very large values of K (0.5) the beam radius is poorly predicted by both models, however it is important to note that Equation 39 was derived for the small angle approximation requiring the beam to stay near the beam axis. Clearly for large values of K, this is no longer applicable. Fortunately, other practical limitations would prohibit any machine from operating in a regime where the small angle approximation was no longer valid.

It is also important to note that these equations have all been derived for a constant energy beam. This represents a non-physical system because electrons are accelerated quickly off of the cathode and therefore the energy is far from constant along the gun. However, because the cathode emits continuously, there will be beam of all energies in the gun and taking the average energy represents a good first-order approximation for calculating the average beam radius change as a function of position along the gun.

3.2.3 Space-charge effects on back-bombardment

In order to compute the space-charge effects on back-bombardment both the transverse and longitudinal effects are added into the back-bombardment power equation. To add in the longitudinal space-charge effect, the peak RF field E_0 can be replaced by the total field E_{tot}. This total field is a function of the RF field and the space-charge field. Because the longitudinal space-charge field partially cancels out the RF field, the total field is simply the combination of

the RF field and the space-charge field, $E_{tot} = E_0 - E_{sc}$. This correction can be added to the back-bombardment power equation giving the result in Equation 43.

(43)

$$P_{ave} = \frac{I v_{eff}}{4\pi^2 f}\left(3\sin\left(\frac{c\pi}{v_{eff}\alpha}\right) - \sin\left(\frac{3c\pi}{v_{eff}\alpha}\right)\right)(E_0 - E_{sc})K$$

Substituting Equation 35 into Equation 43 gives the explicit relationship between the back-bombardment power and the beam current with the effects of longitudinal space-charge, Equation 44.

(44)

$$P_{ave} = \frac{I v_{eff}}{4\pi^2 f}\left(3\sin\left(\frac{c\pi}{v_{eff}\alpha}\right) - \sin\left(\frac{3c\pi}{v_{eff}\alpha}\right)\right)\left(E_0 - \frac{I\lambda}{v_{eff}\pi r_c^2 \epsilon_0 \alpha}\right)K$$

This shows that there is a quadratic variation of the back-bombardment power with the beam current. Looking at Figures 28-30 it is not hard to imagine why this is the case. As the output current increases the back-bombardment power will increase until a point where the space-charge fields begins to dominate over the accelerating field. Following this critical point the back-bombardment power will decrease until it reaches zero. It is important to note that Equation 44 predicts negative values for back-bombardment, once the total field reaches zero the back-bombardment power is forced to zero because there is a net zero field in the cavity. The space-charge field cannot create a negative back-bombardment power.

The transverse space-charge forces impact both the longitudinal space-charge field and the amount of beam that actually strikes the cathode. To compute the effect of the transverse space-charge force on the longitudinal field Equation 42 is substituted into Equation 35, which gives Equation 45.

(45)

$$E_{sc} = \int_0^{\frac{\lambda}{\alpha}} \frac{I}{v_{eff}\pi\epsilon_0 \left(r_0/2 + \sqrt{r_0^2 + 2Kz^2}/2\right)^2} dz$$

Here K is computed using the average energy as well as v_{eff}. It is possible to include relativistic effects through the use of Kim's approximation for the relativistic energy [40]; however, an analysis of this showed little to no improvement on the Equation 45 while introducing a large amount of complexity into the model. Additionally this approach added ambiguity as to what effective RF phase to use. Solving Equation 45 gives the effective space-charge field in the presence of radial defocusing:

(46)

$$E_{sc} = \left(\frac{4I}{v_{eff}\pi\epsilon_0}\right)\left[3L\sqrt{K}\left(r_0 - 2\sqrt{2KL^2 + r_0^2}\right) + \sqrt{6}(8KL^2 + 3r_0^2)\tan^{-1}\left(\frac{2L\sqrt{2/3}\sqrt{K}}{r_0}\right)\right.$$
$$\left. - \sqrt{6}(8KL^2 + 3r_0^2)\tan^{-1}\left(\frac{L\sqrt{2/3}\sqrt{K}}{\sqrt{2KL^2 + r_0^2}}\right)\right] / \left(9\sqrt{K}(8KL^2 r_0 + 3r_0^3)\right)$$

Here $L = \lambda/\alpha$, r_0 is the cathode radius, and K is the space-charge magnitude given by Equation 37. The space-charge field given by Equation 46 can then be substituted into Equation 43 to add the effects of the longitudinal space-charge field in the presence of transverse defocusing on the back-bombardment power.

To account for the transverse defocusing of the beam the effective area of the beam that is deposited on the cathode is calculated. Assuming that previously all the energy was deposited within the cathode radius r_0, the effective energy deposited would simply scale as a function of the actual beam radius returning to the cathode. Using Equation 42, the maximum radius of the

beam deposited on the cathode is calculated as though it traversed the cavity twice. This gives the maximum effective radius of the back-bombarded beam (Equation 47).

(47)

$$r_{max} = \frac{r_0}{2} + \frac{\sqrt{r_0^2 + 8K\left(\frac{\lambda}{\alpha}\right)^2}}{2}$$

The energy deposited on the cathode is related to the effective area of the beam that actually strikes the cathode. Therefore, to account for the transverse defocusing of the beam the ratio of the beam area at the cathode and the cathode area is computed using Equation 48.

(48)

$$R = \frac{r_0^2}{r_{max}^2}$$

This scaling can also be added to the back-bombardment power equation (Equation 43) to further account for the reduction in back-bombardment due to the transverse defocusing of the back-bombarded beam caused by space-charge forces Equation 49.

(49)

$$P_{ave} = \frac{I v_{eff}}{4\pi^2 f}\left(3\sin\left(\frac{c\pi}{v_{eff}\alpha}\right) - \sin\left(\frac{3c\pi}{v_{eff}\alpha}\right)\right)(E_0 - E_{sc}(K, L, r_0))KR$$

3.3 Comparison with simulations

Using Equation 49 and the simulation data presented earlier in this chapter, the back-bombardment power as a function of frequency for constant emitted charge per RF period is computed. Figure 35 shows the back-bombardment power per pico-Coulomb as a function of

frequency for three different bunch charges. The dashed lines give the analytic model while simulation results are given in solid lines.

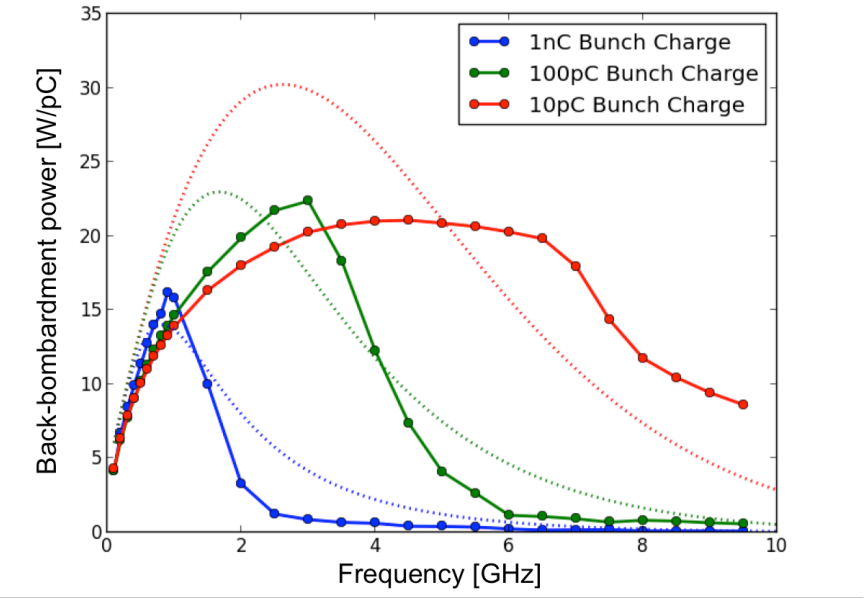

Figure 35: Comparison of analytic model for back-bombardment with space-charge effects and simulation data obtained on a short gap thermionic gun. Simulations were run for three different bunch charges.

Qualitatively this comparison is very good. The back-bombardment power steadily increases until it reaches a maximum. Once the space-charge effects become more prominent the back-bombardment power begins to decrease asymptotically towards zero. While the shape of the analytical models are slightly different than the simulation results and the peaks occur at slightly different locations the model does a decent job of predicting the physics of how space-charge is effecting the back-bombardment power. There are a number of assumptions wrapped up in these models that are not completely accurate, the main one being a constant velocity beam. While assuming the beam is at a constant velocity allows for exact solutions to the space-charge equations and approximations, it presents a major area where the model could be improved. This would potentially create a theory that better predicts the shape of Figure 35 in addition to making

a better prediction to the peaks. We have shown that Child's law for space-charge limiting current accurately predicts these peaks; therefore with some refinement we may be able to predict the behavior in a more precise manner. However, the models derived in this chapter do a good job of explaining how the space-charge forces impact back-bombardment power and we have shown good qualitative comparison with our simulation results. We have shown that the longitudinal space-charge force decreases the effective accelerating field in the gap while the transverse space-charge force defocuses the beam and decreases the effective area of the back-bombarded beam.

4. Back-bombardment in multi-cell guns

The previous two chapters have discussed the effects of back-bombardment in only single-cell guns. While single-cell guns represent a wide range of possible designs, having more than one accelerating cell is often desired. For the study of back-bombardment, the addition of more cells cannot decrease the base-line back-bombardment power as particles that don't make it out of the first cell are not impacted by the second cell. In many configurations the addition of more cells will increase the back-bombardment power; however, a second cell could be of great benefit to the longitudinal bunch profile and the average beam energy. Therefore, a couple classes of multi-cell guns are studied to understand how the back-bombardment power is increased by the addition of a second cell. This is broken up into three classes of multi-cell problems: n-cell, zero-mode guns, n-cell, pi-mode guns, and 2-cell guns that are independently phased and driven. In order to simplify the parameter space of the n-cell guns, the gap lengths are fixed for each cell. This is fairly typical for electron machines and aside from the first cell being varied slightly to optimize the beam dynamics, the other cells are usually a fixed length. Figure 36 shows a sketch of a three-cell gun with the fractional gap lengths shown. Additionally, the field directions are shown to indicate the zero-mode and the pi-mode in blue and red respectively.

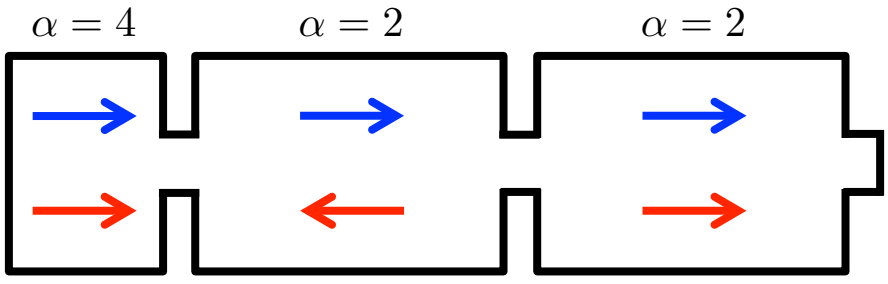

Figure 36: A sketch of a three-cell gun indicating the fractional gap lengths used to study back-bombardment in n-cell guns. The arrows indicate the field directions for the zero-mode (blue) and the pi-mode (red).

4.1 Back-bombardment power in n-cell, zero-mode guns

The simplest of the three classes of multi-cell gun problems is the n-cell, zero-mode gun. This configuration has no phase shift in the field between adjacent cells. In a zero-mode gun the back-bombardment power can only increase as the number of cells increases. This section uses a simple scaling, followed by 1-D particle pusher simulations, and concluded with 2.5-D PIC simulations to explain how the back-bombardment power will increase with the addition of more cells. Zero-mode guns represent a configuration that is not very practical from an accelerator design standpoint, however they are the simplest class of multi-cell guns so their analysis provides some initial insight into how back-bombardment is effected by the addition of more cells in the cavity.

4.1.1 Heuristic discussion of back-bombardment in zero-mode guns

Because there is no phase shift between cells in a zero-mode, multi-cell, gun the addition of more cells results in a field on axis that is fundamentally the same as a single-cell gun with a very long gap length. As was shown in Figure 36, the fractional gap length of the first cell is 4, while the additional cells have a fractional gap length of 2.

The addition of more cells introduces cases where particles are accelerated out of the first cell but do not make it all the way out of the gun and get trapped in different cells before being either eventually lost to the walls of the gun, are back-bombarded, or are kicked out of the gun. The particles that get stuck and back-bombard the cathode after the first period will increase the average back-bombardment power; however, the range of phases where this occurs is low and therefore the primary increase in the back-bombardment power for zero-mode guns is due to the addition of the second cell.

For a gap length that is arbitrarily long, the particles that back-bombard the cathode in the first RF period must see twice as much positive field as negative field. This corresponds to a fractional gap length of 2 in the single cell analysis. Even though this is not really the normalized gap length of the two-cell system, it can be used as the effective fractional gap length to compute the back-bombardment power due to the first RF period, which is the primary mode of back-bombardment in the multi-cell gun. In order to determine by how much the back-bombardment power will increase by the addition of the second cell in the zero-mode, we examine the ratio of the back-bombardment power in the two-cell gun to the back-bombardment power in the single cell gun. Everything else being the same, the ratio of the back-bombardment power in the two-cell gun to the single cell gun is simply, $P = (1/\alpha_2^2)/(1/\alpha_1^2)$, for the single cell gun $\alpha_1 = 4$, and for the multi-cell gun $\alpha_2 = 2$. This shows that by adding a second cell in the zero-mode we expect the back-bombardment power to increase by a factor of 4.

While this very rough heuristic estimate gives some insight into how much the back-bombardment power will increase with the addition of one or more cells, a detailed picture, unfortunately, cannot be determined through analytical equations. In order to study the back-bombardment power in multi-cell zero-mode guns in more detail, 1-D and 2.5-D simulations were run.

4.1.2 1-D simulations of back-bombardment in n-cell zero-mode guns

1-D simulations of a thermionic cathode in a n-cell zero-mode RF gun were run in order to both verify the estimated increase in the back-bombardment power and to study in more detail how this process occurs. These simulations numerically solve the relativistic equations of motion (Equation 50) for particles emitted from the cathode whenever the field is of the appropriate sign.

The particles are tracked through the geometry and those that return to the cathode are used in the calculation of the back-bombardment power.

(50)

$$\gamma \frac{dv}{dt} + v\frac{d\gamma}{dt} = \frac{q}{m}E(z,t)$$

$$\frac{dz}{dt} = v$$

For the n-cell zero-mode gun the field profile is approximated by a cosine squared function along the gun and zero outside the gun, this is given explicitly in terms of the number of cells, the RF wavelength, and the RF frequency by Equation 51.

(51)

$$E(z,t) = \begin{cases} \cos^2\left(\frac{2\pi z}{\lambda}\right)\sin(\omega t) & 0 < z < (n-1)\frac{\lambda}{2} + \frac{\lambda}{4} \\ 0 & z < 0, z > (n-1)\frac{\lambda}{2} + \frac{\lambda}{4} \end{cases}$$

Substituting Equation 51 into Equation 50 and using the Runga-Kutta technique these equations were solved for a wide range of peak fields and frequencies with a cell number ranging from 1 to 18. Here it is important to introduce a new parameter that will be referred to as the effective gun voltage, Equation 52.

(52)

$$V_{eff} = \frac{cE_{peak}}{f}$$

This parameter closely resembles the ψ parameter introduced in Chapter 2; however, it is subtly different in that it only considers the RF frequency and the peak RF field. This effective voltage shows how much accelerating power the gun will have. When analyzing the increase in back-bombardment power for the addition of more cells, the effective voltage is used to show how the

back-bombardment power will vary. The other parameter that is introduced is the back-bombardment ratio. The back-bombardment ratio is used to quantify how much the back-bombardment power has increased relative to a particular gun configuration. For some cases the reference case is a single cell gun and for some cases the reference case is a two-cell gun. It was estimated in the previous section that the back-bombardment power would increase by a factor of 4 when adding on the second half-cell. Figure 37 shows the ratio of the back-bombardment power in a 1.5 cell gun to a 0.5 cell gun as function of the effective cavity voltage.

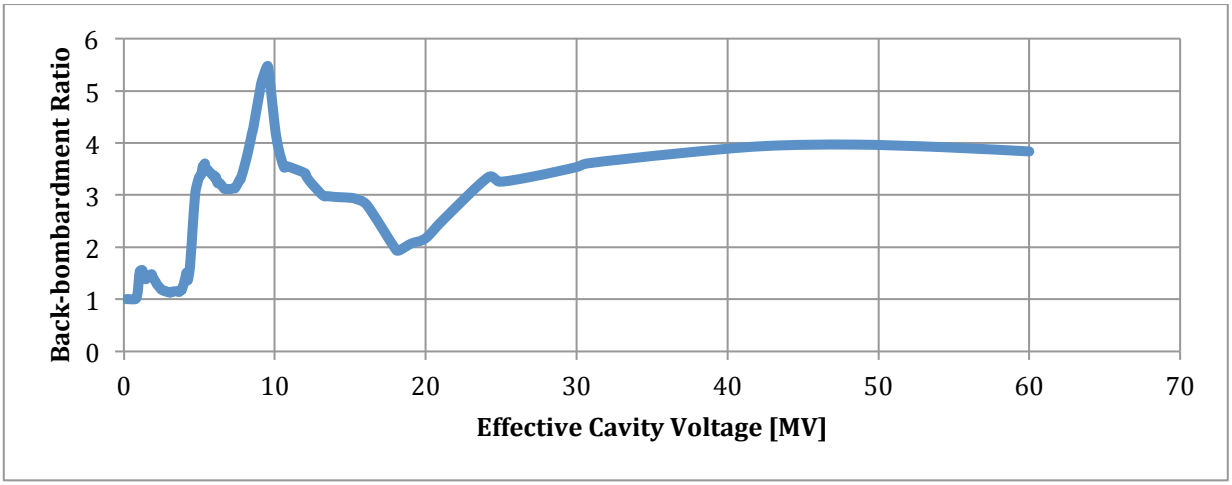

Figure 37: Ratio of the back-bombardment power in a 1.5-cell gun to a 0.5-cell gun as a function of the effective cavity voltage.

This shows some interesting behavior; at very low voltage the additional back-bombardment power due to the second cell ranges from zero to an up to 50% increase. At around 5 MV the increase in back-bombardment power jumps up to around 3. After that there is a minimum of double the back-bombardment power and a maximum of 5.5 times increase in the back-bombardment power, with an asymptotic value of 4. After 5MV the average increase in the back-bombardment power is about 3.5 times that of the single cell. The maxima and minima that occur in the region between 5MV and 25 MV are likely due to conditions where the particles have ideal velocities to either reduce or increase the number of back-bombarded electrons in the

second cell. Additionally the previous section discussed that the addition of the second cell would be the primary source of back-bombardment increase for zero-mode guns. To verify this the back-bombardment power ratio was computed using Equation 52 to show how the addition of more cells beyond the first two would further increase the back-bombardment power.

(52)

$$BB_{ratio} = \frac{P_{n-cells}}{P_{1.5-cells}}$$

Here $P_{n-cells}$ is the back-bombardment power computed for one RF period due to some number of cells greater than 1.5, and $P_{1.5-cells}$ is the back-bombardment power computed for one RF period due to 1.5 cells. Figure 38 shows the back-bombardment ratio for a 3.5 cell gun plotted as a function of the effective gun voltage.

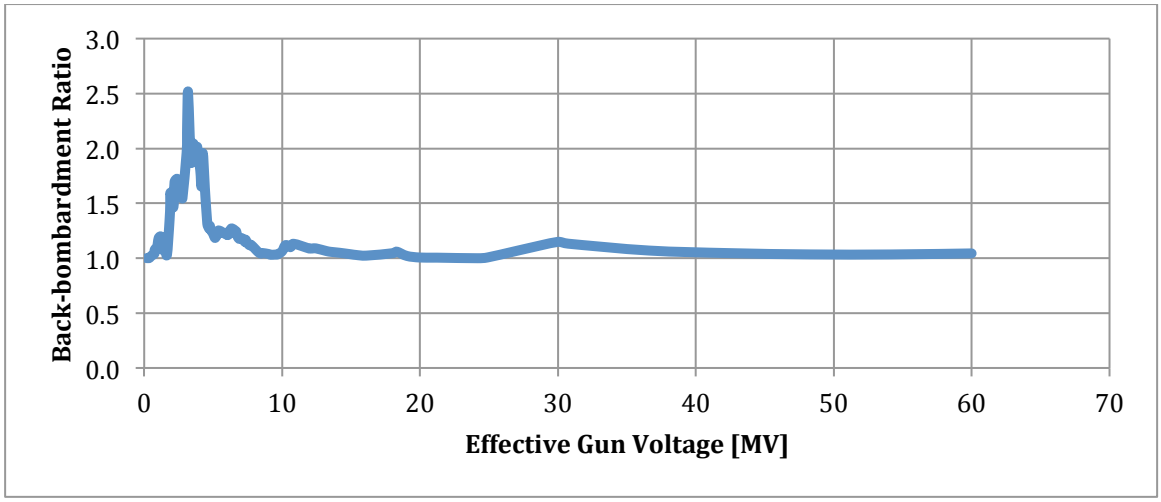

Figure 38: Ratio of the back-bombardment power in a n-cell gun to a 1.5-cell gun as a function of the effective cavity voltage.

This shows a spike in the back-bombardment ratio around 5MV. Figure 37 shows that even for the simpler 1.5 cell case, the back-bombardment ratio has odd behavior around 5MV. Outside of this region there is still an increase in the back-bombardment power; however, it is much smaller. The median increase in the back-bombardment power from a 1.5 cell gun to a 3.5 cell

gun is about 13%. Additionally for guns with an effective cavity voltage greater than 10, the back-bombardment power ratio is very close to 1 indicating as expected that there is no further increase in the back-bombardment power by increasing from 1.5 to 3.5 cells. Figure 39 shows the back-bombardment power ratio for guns with cell numbers ranging from 5.5 to 17.5, which shows similar behavior as Figure 37.

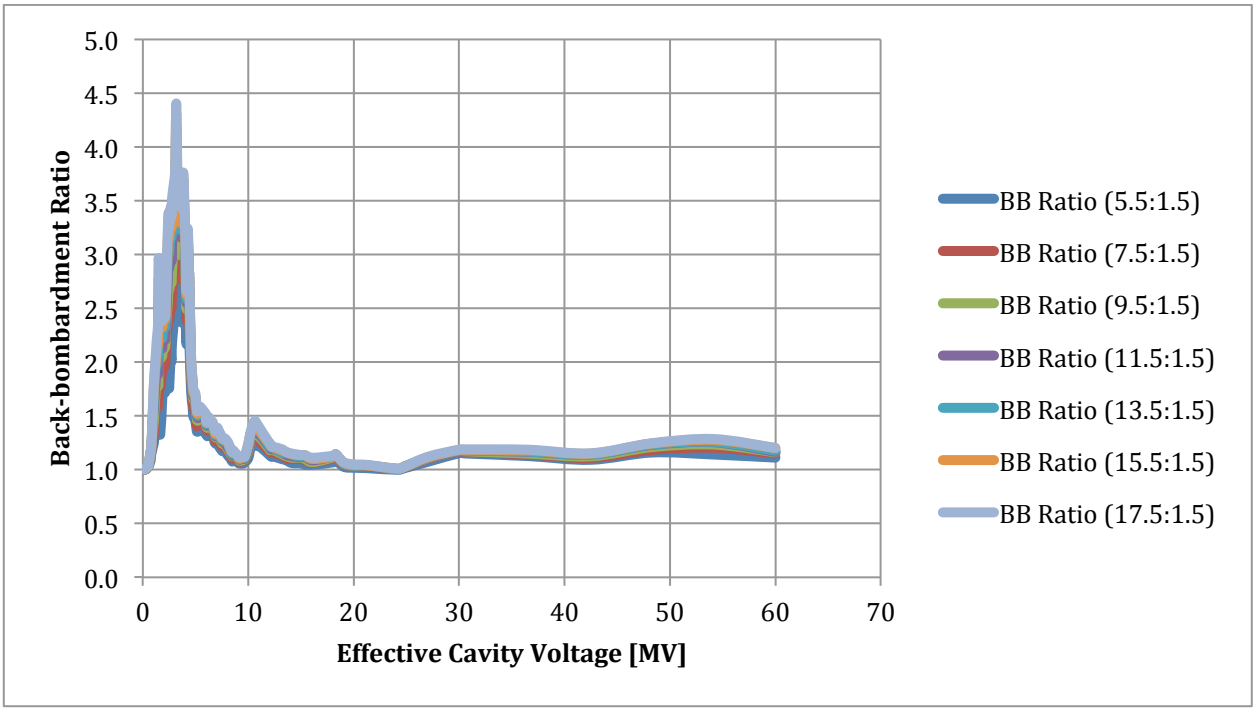

Figure 39: Back-bombardment ratio as a function of effective cavity ratio. Note that there is a spike in the back-bombardment power ratio around 2.5-5 MV, as is also seen in Figure 37.

These data show the same spike in the back-bombardment power at around 5MV and also show a fairly constant back-bombardment power ratio, close to 1, for gun voltages greater than 10 MV. The median back-bombardment power ratio helps to reduce the information shown in Figure 38 and 39 into a single figure of merit for each cell number. While this is not really a statistical analysis the median gives the middle of the range for the back-bombardment power increase. Figure 40 shows the median back-bombardment power ratio as a function of the cell number.

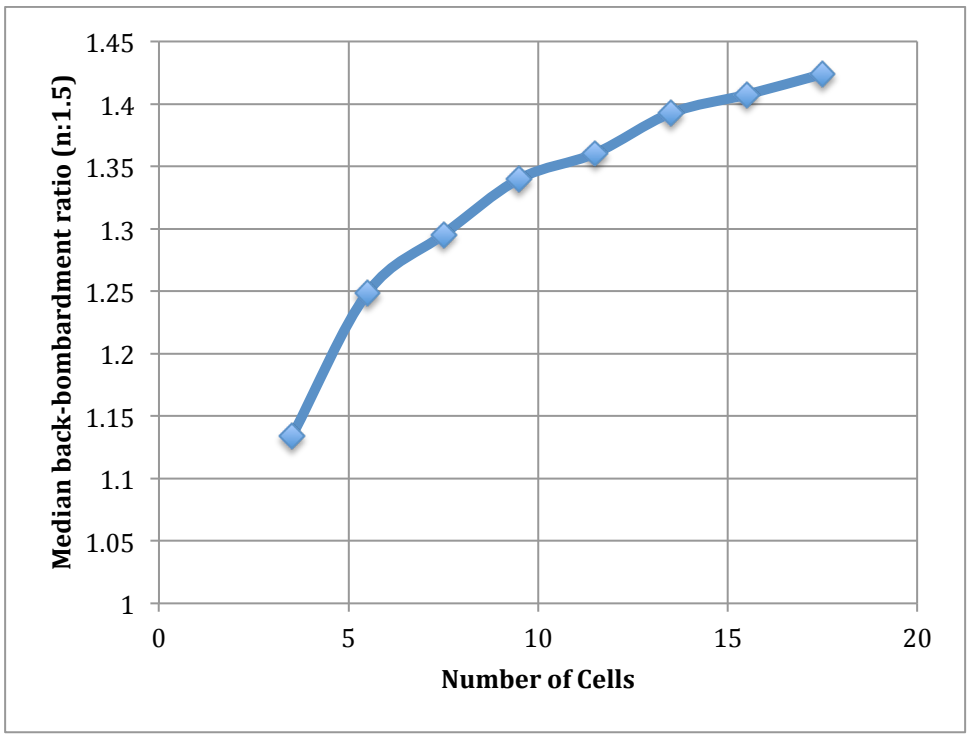

Figure 40: Median back-bombardment power ratio as a function of the number of cells. The median is taken over the whole range of effective voltages for a particular number of cells.

This shows a steady increase in the median back-bombardment power ratio as a function of the number of cells. Recall that the back-bombardment power ratio for these cases is being taken in reference to the 1.5-cell case; therefore, this is showing how the back-bombardment power increases further after the inclusion of the second accelerating cell. This steady increase is expected, as more cells means there are more particles that can get stuck and back-bombard the cathode, most of which can be at higher energy. Additionally it looks as though this increase is asymptotic as the number of cells increases.

4.1.3 2.5-D simulations of back-bombardment in n-cell zero-mode guns

In order to verify the 1-D simulations, 2.5-D particle-in-cell simulations were run using SPIFFE and using the same field profile given by Equation 51. For comparison purposes the median

back-bombardment power ratio was computed for the same range of cell numbers. This is then compared with the results of the 1-D simulations in Figure 41.

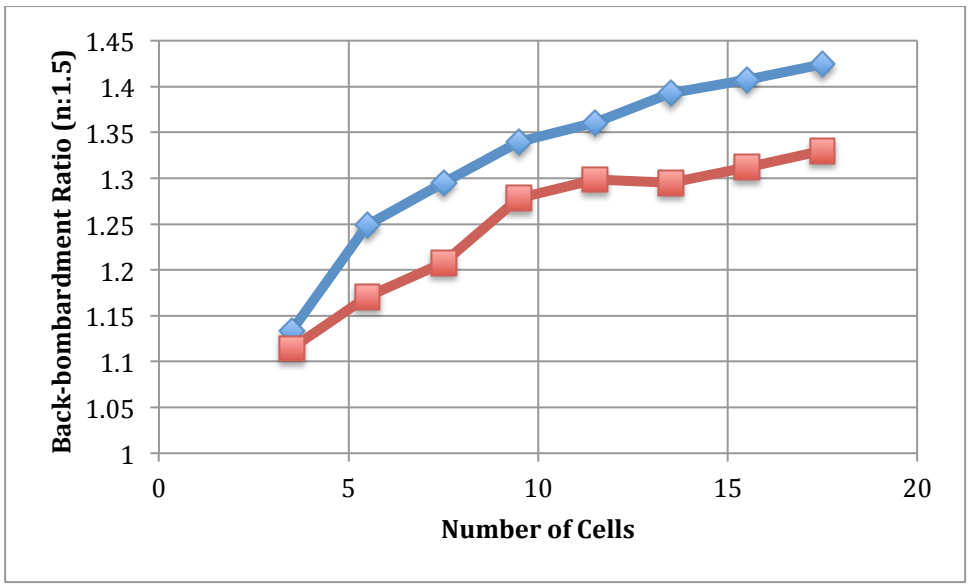

Figure 41: Median back-bombardment power ratio as a function of the number of cells, 1-D simulations are in blue, 2.5-D simulations are in red. The median is taken over the whole range of effective voltages for a particular number of cells.

This shows that the 1-D simulations and the 2.5-D simulations match relatively well. The 2.5-D simulations show data that is slightly noisier than the 1-D simulations; this is likely due to the number of simulations run. For the 1-D case 110 simulations were run for each cell number while for the 2.5-D simulations only 11 simulations were run for each cell number. This was done because the 2.5-D simulations are much more computationally intensive than the 1-D simulations. Even with this large difference in the number of simulations per number of cells, the data agrees relatively well showing that this trend is what should be expected when adding many cells operating in the zero-mode. Because the median increase in the back-bombardment power from the single cell gun to the two cell gun was around 3.5 and the increase in the back-bombardment power from the two-cell gun to the n-cell gun was between 0.1 and 0.45 this

shows that the back-bombardment power is increased primarily due to the second accelerating cell as expected.

4.2 Back-bombardment power in n-cell pi-mode guns

While it is interesting to see the effects of adding cells in the zero-mode gun configuration, this gun is almost never used, as it is not optimal for acceleration or for beam dynamics. A far more common mode of operation is the pi-mode. Unfortunately, when analyzing a pi-mode gun, not even a simple back-of-the-envelope calculation can be done to predict the increase in back-bombardment power due to the addition of more cells. Therefore, the results in this section are given for the simulation of n-cell pi-mode guns using both the 1-D code and the 2.5-D code SPIFFE.

4.2.1 1-D Simulations of back-bombardment in n-cell pi-mode guns

To analyze the back-bombardment power in a n-cell pi-mode gun, Equation 50 was solved numerically using the axial field profile given by Equation 53.

(53)

$$E(z,t) = \begin{cases} \cos\left(\frac{2\pi z}{\lambda}\right)\sin(\omega t) & 0 < z < (n-1)\frac{\lambda}{2} + \frac{\lambda}{4} \\ 0 & z < 0, z > (n-1)\frac{\lambda}{2} + \frac{\lambda}{4} \end{cases}$$

As with the previous section the addition of extra cells will only increase the back-bombardment power as the first cell fundamentally limits this process. Again the back-bombardment power ratio is used to characterize how the back-bombardment power will increase due to the addition of more cells. Figure 42 shows the back-bombardment power ratio of a 1.5 cell gun to the 0.5 cell gun as a function of the effective cavity voltage.

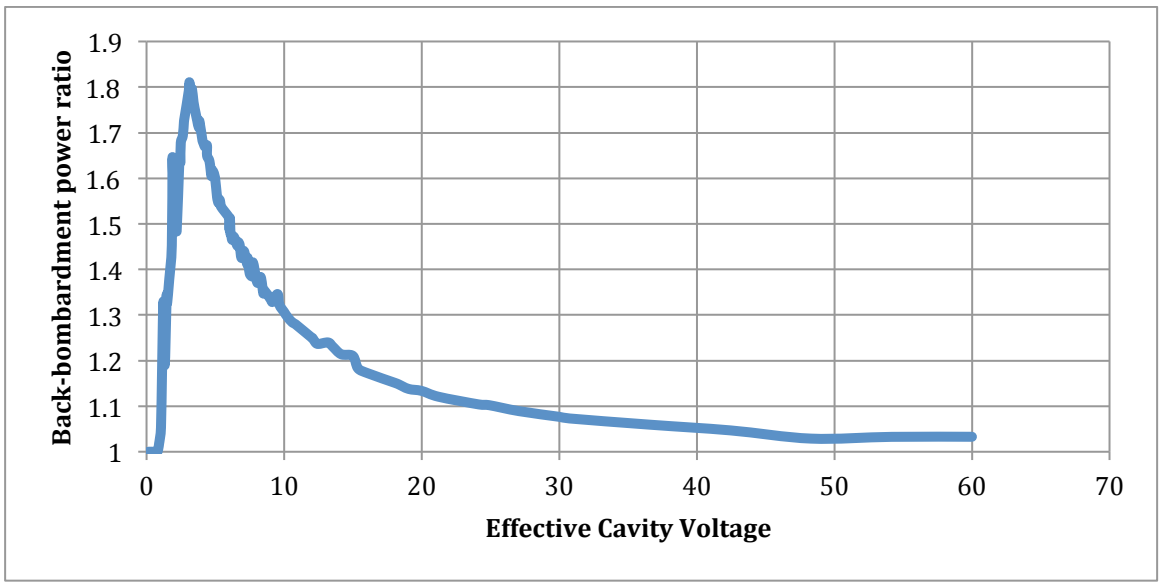

Figure 42: Back-bombardment power ratio of a 1.5 cell gun to a single cell gun as a function of the cavity voltage.

This shows that as the effective cavity voltage increases there is a spike in the back-bombardment power ratio that slowly decays towards unity as the effective cavity voltage increases. This is because for high voltages particles that enter the second accelerating cell will have enough energy to never decelerate back to rest and so eventually exit the gun. By adding more cells, the back-bombardment power ratio exhibits a similar trend; however, there is a general increase in the back-bombardment power that can be characterized by the median back-bombardment ratio. Figure 43 shows the median back-bombardment power ratio as a function of the number of cells with the reference case being the 1.5 cell gun.

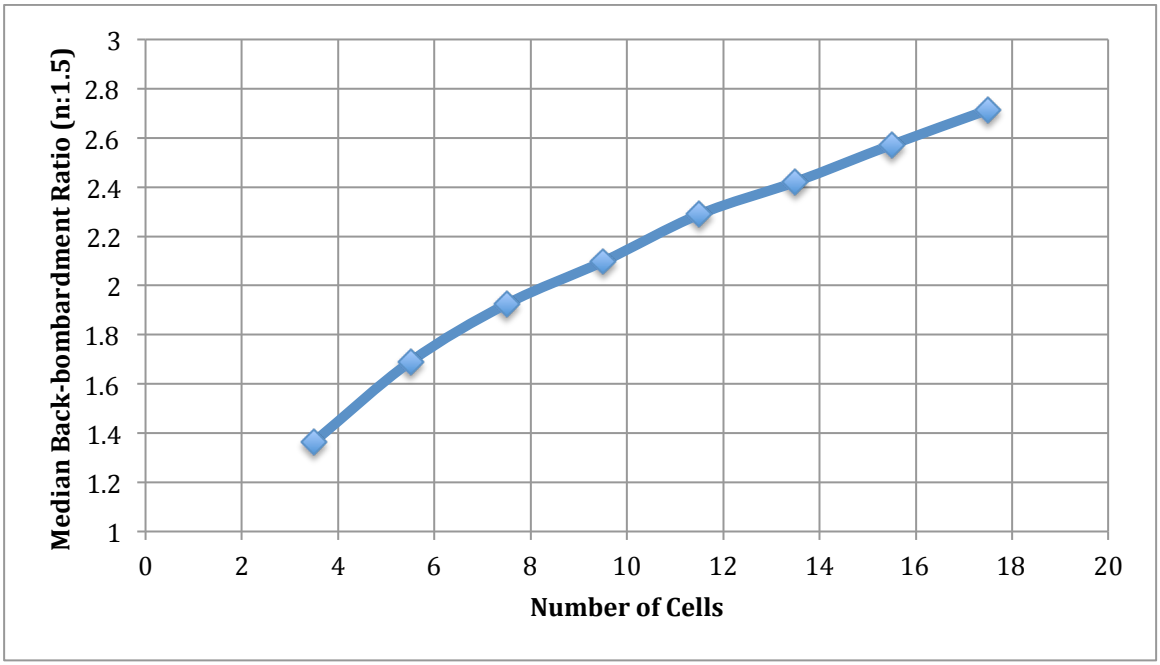

Figure 43: Median back-bombardment power ratio as a function of cell number. This ratio is computed against the 1.5 cell gun case similar to Figure 38.

Unlike the zero-mode gun, the primary mode of back-bombardment increase is not due to the second cell but due to the aggregate effect of some electrons being trapped in cells and gradually being sent back towards the cathode. This is evident in the steady increase in the back-bombardment power ratio that is shown by Figure 43. A comparison of the zero-mode guns with the pi-mode guns provides some information about the differences between these two configurations. Figure 44 shows the median back-bombardment power ratio as a function of the number of cells with a reference case of the single cell case.

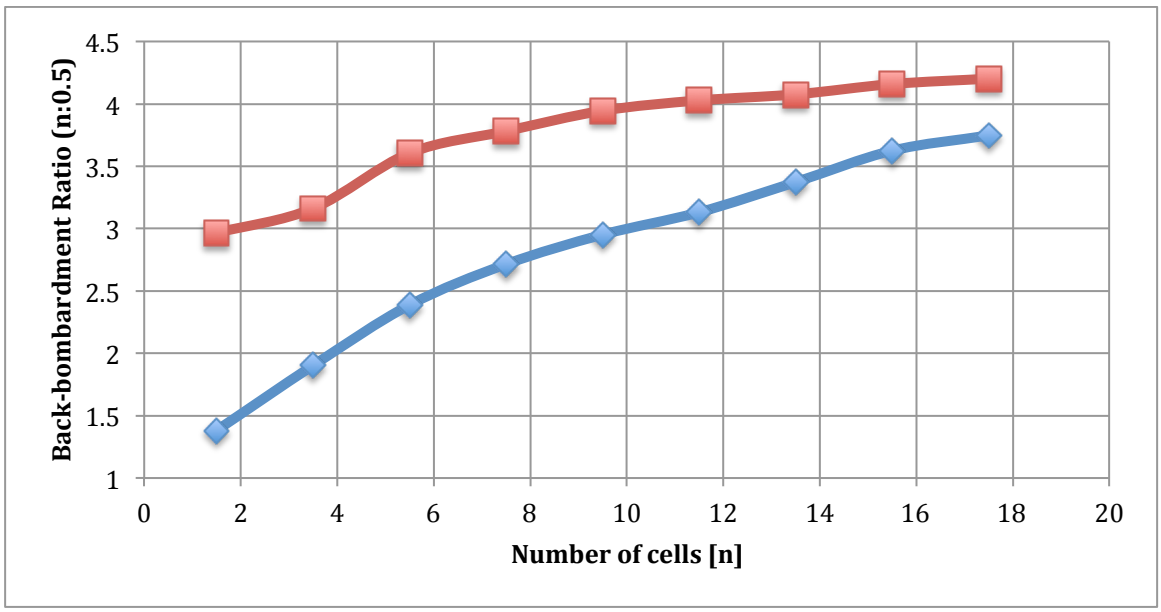

Figure 44: median back-bombardment power ratio of gun with n-cells compared to the single half cell. Red is the zero-mode gun, blue is the pi-mode gun.

This shows that in comparison the zero-mode gun has the biggest increase by adding the second cell, with a gradual increase after that. While in contrast the pi-mode gun shows a steady increase in the back-bombardment power ratio as a function of the number of cells. This comparison shows just how operating in the different cavity mode will impact the increase in the back-bombardment power.

4.2.2 2.5-D simulations of back-bombardment in n-cell pi-mode guns

As with the zero-mode gun, it is important to verify the 1-D simulation results with the 2.5-D SPIFFE simulations. These simulations were run over a subset of the parameters that the 1-D simulations were run over. The median back-bombardment power ratio was used as a figure of merit for the gun with a particular number of cells. The median back-bombardment power ratio was taken over a range of operating voltages. Similar to the zero-mode case, the 2.5-D simulations were run over a smaller subset of gun parameters and therefore the median will be a

little noisier than the median as seen in the 1-D simulations. Figure 45 shows a comparison of the median back-bombardment power ratio for the 1-D and 2.5-D simulations.

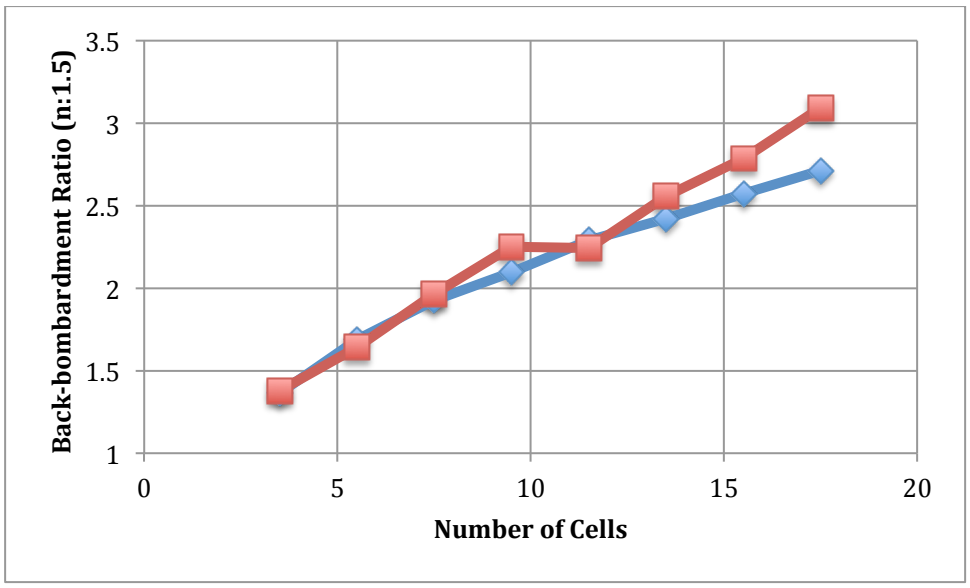

Figure 45: Median back-bombardment power ratio as a function of the number of cells, 1-D simulations are in blue, 2.5-D simulations are in red. The median is taken over the whole range of effective voltages for a particular number of cells.

This shows that in general the 1-D simulations accurately predict the increase in back-bombardment power as the number of cells is increased. The 2.5-D simulations show more of a linear increase in the back-bombardment power ratio that doesn't seem to roll off with high cell number. This is likely due to there not being an adequate number of cases for computing the median back-bombardment power ratio for these guns.

4.3 Back-bombardment in independently phased 2-cell guns

While zero and pi mode guns are easier to analyze from a modeling perspective, they do not accurately represent the full class of multi-cell guns that might be utilized with a thermionic cathode. In fact they represent a fairly narrow subset of gun designs that may be used for this type of cathode system. It may be far more advantageous to control the gap length, field strength,

and relative phasing of the two cells independently. Similar to the zero and pi-mode guns, the first cell will fundamentally limit how low the back-bombardment power can go. However, with the flexibility to drive the two cells independently it is possible to create a scenario where the back-bombardment power will not be increased. This would be done in order to create a better output beam, while the output beam parameters are not discussed here a longer accelerating gap would result in a higher peak energy, possibly a lower energy spread if there is some ballistic bunch compression, and possibly improve the beam emittance out of the gun [41]. The output beam properties are not discussed here, but the back-bombardment power is analyzed as a function of the free gun parameters. Because an analytic model of a gun with such flexibility in the field strength and the geometry parameters is not tractable, this analysis will be solely a simulation-based analysis. This simulation study was done using the 1-D technique used in the previous sections.

4.3.1 1-D Simulations of back-bombardment in 2-cell guns

The two cell cavities are simulated using a field profile that allows for independent phasing of the two cells, independent peak fields, and variable gap lengths, Equation 54.

(54)

$$E(z,t) = \begin{cases} E_1 \cos\left(\frac{\pi\alpha_1}{2\lambda}z\right)\sin(\omega t) & 0 < z < \frac{\lambda}{\alpha_1} \\ \mathrm{E}_2\cos\left(\frac{\pi\alpha_2}{\lambda}\left(z-\frac{\lambda}{\alpha_1}\right)\right)\sin(\omega t+\phi_r) & \frac{\lambda}{\alpha_1} < z < \frac{\lambda}{\alpha_1}+\frac{\lambda}{\alpha_2} \\ 0 & else \end{cases}$$

Equation 54 is then substituted into Equation 50 and the various particle trajectories are tracked through the gun. In this configuration there are many parameters that can be varied and therefore only a few representative data sets are shown to indicate some of the design trade-off trends. Choosing a value of 20 MV/m for the first cell's accelerating field and assuming the first cell is a

quarter wave cell (α=4), the field of the second cell was chosen to be integer multiples of the first cell's field, ranging from 20MV/m to 60MV/m. The second cell phase was then varied for four different cell-2 gap lengths. Figure 46 shows the back-bombardment power ratio for a gun with 2 cells where the second cell has a peak field of 60MV/m.

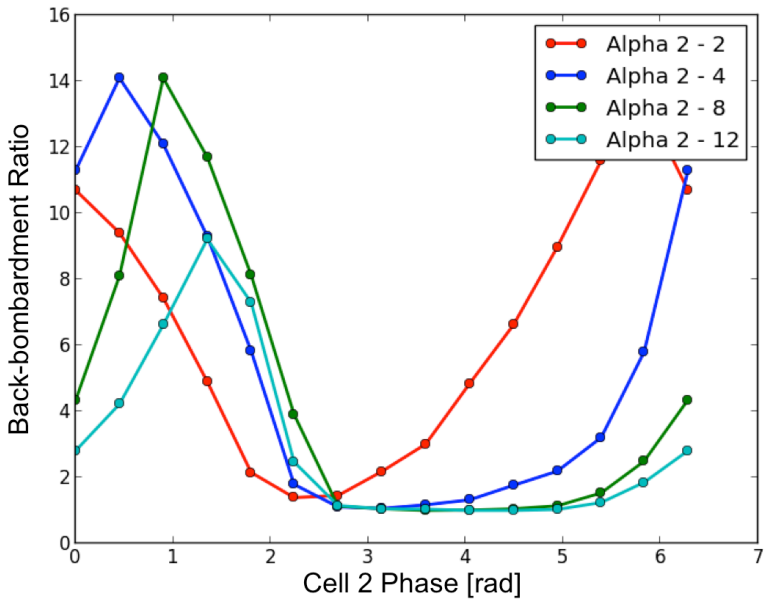

Figure 46: Back-bombardment power ratio as a function of cell 2's phase for four values of alpha2. The peak field of cell 2 was 60MV/m.

This shows that for a conventional 2-cell gun where the second cell is a full half wave cavity, ($\alpha = 2$), the zero-mode is almost the worst mode to operate in from a back-bombardment perspective. This is not a surprising revelation but it does confirm the results shown previously in this chapter. Additionally, the conventional 2-cell gun the pi-mode is a much better mode to operate in; however, a slight decrease in the phase of the second cell from pi radians to around 2 radians provides substantial improvement in the back-bombardment power ratio. One drawback of this case is the minimum is not very broad. This means that small changes in the phasing of the second cell would greatly increase the back-bombardment. To mitigate this effect increasing alpha will shorten the second cell. Figure 46 shows that as alpha2 is increased the minimum in

the back-bombardment power as a function of the second cell's phase becomes much more broad. This will come with a trade-off in the forward power as a shorter second cell results in a lower total acceleration voltage for the beam. Additionally as the second cell becomes asymptotically short the problem reduces back to the single cell problem. Note also that as the second cell length decreases, the optimal operating phase shifts to the right. Figure 47 shows the back-bombardment power ratio for the same configurations as Figure 46 however now the field in the second cell was decreased to 40 MV/m.

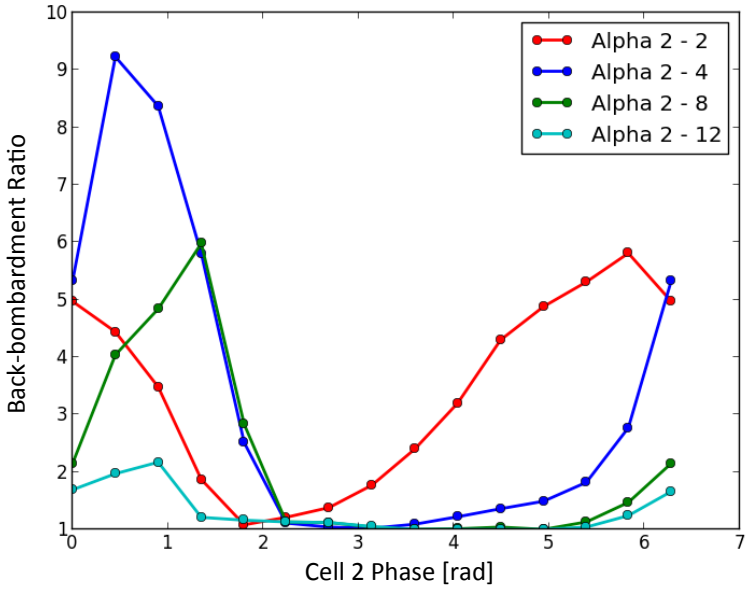

Figure 47: Back-bombardment power ratio as a function of cell2's phase for four values of alpha2. The peak field of cell2 was 40MV/m.

Figure 47 shows similar trends as Figure 46; however, by decreasing the field in the second cell the optimum-operating phase is even broader. Additionally the peak back-bombardment power ratio is lower as the total amount of accelerating field is lower. Further decreasing the field in the second cell will even further enhance this effect. Figures 48 shows the back-bombardment power ratio for the 2-cell gun where the second cell is operated at the same peak field as the first cell.

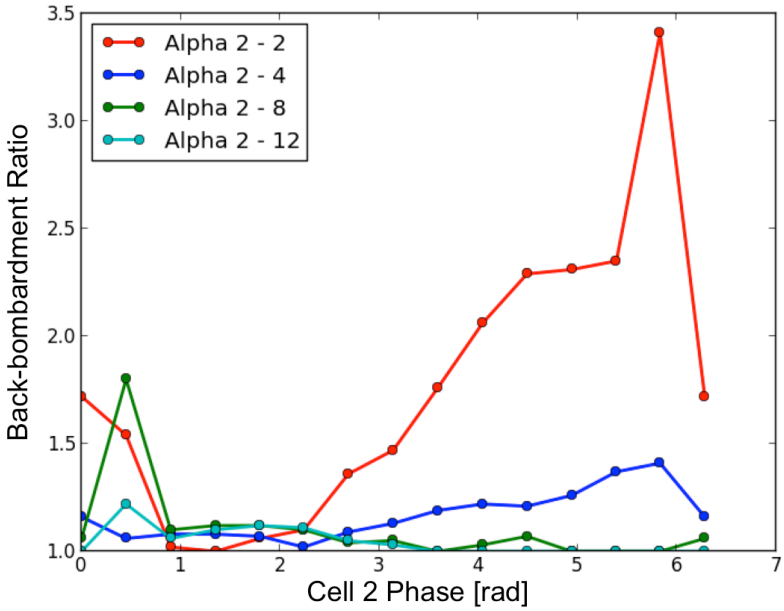

Figure 48: Back-bombardment power ratio as a function of cell2's phase for four values of alpha2. The peak field of cell2 was 20MV/m.

Figure 48 shows that for the classical 2-cell gun the optimum operating phase has shifted to the left. Additionally, for cases where the second cell is shorter than the classical 2-cell gun case the back-bombardment ratio is relatively low across the board. While this is an improvement, any increase in the back-bombardment power due to the addition of a second cell could be extremely detrimental. In order to examine the cases where the second cell is of equal length or shorter than the first cell an additional simulation was performed. Figure 49 shows the result in Figure 48 but without the case where the second cell has an alpha of 2.

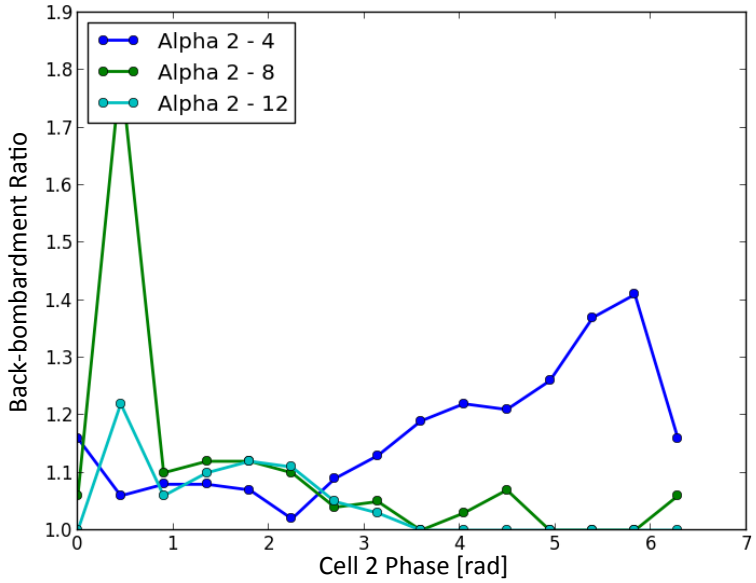

Figure 49: Back-bombardment power ratio as a function of cell2's phase for three values of alpha2. The peak field of cell2 was 20MV/m.

This shows that there is a nice broad range of phases that will not increase the back-bombardment power if the second cell is shorter than the first cell. Unlike the zero and pi mode guns, allowing for the phase and length of the second cell to vary can almost completely mitigate the increase in back-bombardment power due to the second cell. This allows for the second cell to possibly increase the total output power of the gun and even potentially decrease the total energy spread. The output beam dynamics are beyond the scope of this dissertation but with this knowledge in mind, one could optimize a cavity design that will not increase the back-bombardment power from the first cell while possibly improving the output beam.

If the back-bombardment process is fundamentally limited by the first cell, it may be possible to decrease the gap length of the first cell and add a second cell to help optimize the longitudinal phase space while simultaneously not increasing the back-bombardment power. 1-D simulations were performed with a gun that has an alpha of 10 in the first cell while the second cell had an

alpha that was 2, 4 ,8 ,or 12. As with before the phase of the second cavity was scanned while keeping the peak field constant. Figure 50 shows the back-bombardment ratio as a function of cell2's phase for four different gap lengths in the second cell.

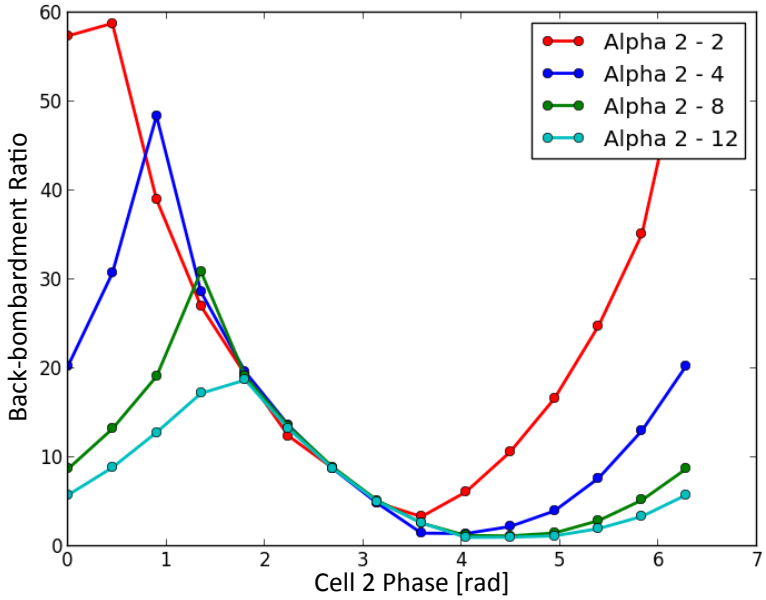

Figure 50: Back-bombardment power ratio as a function of cell2's phase for four values of alpha2. The peak field of cell2 was 60MV/m.

This shows that, as with the case where cell1's alpha is 4, there is a depression in the back-bombardment ratio at a phase that is different from that of a traditional mode. Additionally as alpha2 is increased the optimum phase range for the back-bombardment ratio broadens as with the previous results. Figure 51 shows the back-bombardment ratio as a function of cell2's phase for a peak field in cell2 of 40 MV/m.

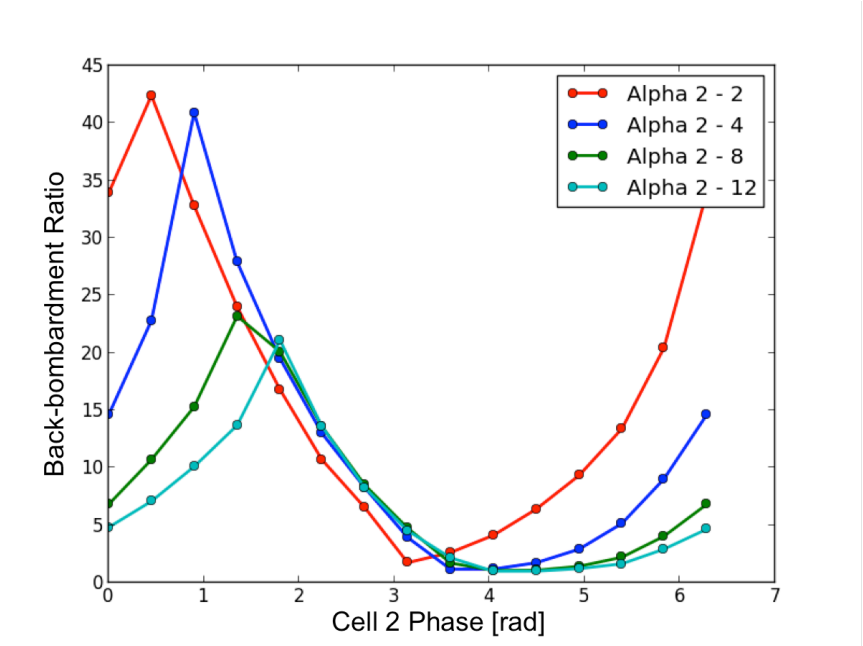

Figure 51: Back-bombardment power ratio as a function of cell2's phase for four values of alpha2. The peak field of cell2 was 40MV/m.

The decrease in the field shows a decrease in the global scale indicating that the back-bombarded electrons are at a lower energy. The shape of the plotted curves in Figure 51 are almost identical to the curves in Figure 50. Figure 52 shows the same results as Figures 50 and 51 but with a further decreased field in the second cell down to 20MV/m.

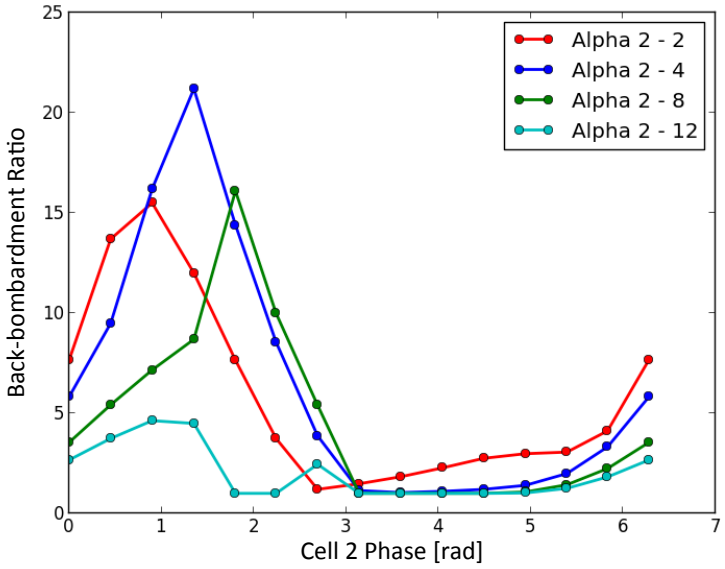

Figure 52: Back-bombardment power ratio as a function of cell2's phase for four values of alpha2. The peak field of cell2 was 40MV/m.

The minimum in the back-bombardment ratio as a function of phase has an even broader shape for this case indicating an even wider range of acceptable phases when operating in this configuration. Table 7 shows the optimum phase to not increase the back-bombardment power, for four different gap lengths and peak fields for the second cell.

Table 7: Optimum phase of the second cell if the first cell has an alpha of 4

	Alpha2 = 2	Alpha2 = 4	Alpha2 = 8	Alpha2 = 12
Cell 2 Field 20 MV/m	1.35	2.24	3.59	0.0
Cell 2 Field 40 MV/m	1.8	3.14	3.59	3.59
Cell 2 Field 60 MV/m	2.24	3.14	3.59	4.04

This shows how the optimum phase shifts as a function of both the peak field in the second cell and the second cell gap length. Note that only for a couple cases are the phases aligned with either of the standard operating modes. Additionally it is important to recall that for cases where the second cell is shorter than the first cell, the optimum phase range is broad and therefore these phases have some finite variation attached to them that will still not increase the back-

bombardment power. As with the figures where a shorter first cell was examined, Table 8 shows the same results as Table 7 but for a gun with a first cell gap length equal to one-tenth an RF wavelength. This represents a very short gap and therefore will have low back-bombardment power.

Table 8: Optimum phase of the second cell if the first cell has an alpha of 4

	Alpha2 = 2	Alpha2 = 4	Alpha2 = 8	Alpha2 = 12
Cell 2 Field 20 MV/m	2.69	3.59	3.14	1.8
Cell 2 Field 40 MV/m	3.14	3.59	4.04	4.04
Cell 2 Field 60 MV/m	3.59	4.04	4.49	4.04

This shows that in general for the short first cell, the second cell should not be phased in the classical manner and should be independently phased to reduce the increase in back-bombardment due to the second cell.

This chapter has shown that the introduction of additional cells operating in either the zero or pi-mode will necessarily increase the back-bombardment power. However, introducing a second cell that is independently phased from the first cell can be tuned to not further increase the back-bombardment power. This is an important revelation as the energy spread of an un-gated thermionic cathode RF gun is not suitable for use in many machines and will need to be chopped before being accelerated further. If a gun could be tuned to operate in this un-gated mode without increasing the back-bombardment power but while compensating for this energy spread, the need to adjust the beam parameters down-stream could be reduced.

5. A Back-bombardment mitigation technique

The previous three chapters gave an extensive analysis of back-bombardment in single-cell guns and an overview of how the addition of further accelerating cells will impact the amount of back-bombardment. This chapter transitions away from explaining how back-bombardment occurs and how it is affected by gun parameters to studying a novel technique for mitigating the effects of back-bombardment. This technique utilizes a time harmonic field in the cavity to change the temporal field profile. The discussion begins with an overview of how the technique works from a first principles standpoint, and then 1-D particle pusher simulations are performed to show how well the technique works in principle, this is followed by 2.5-D PIC simulations performed using SPIFFE.

5.1 Two-frequency gun for back-bombardment mitigation

The ideal waveform to completely mitigate the back-bombardment effect while not being a DC gun is a configuration where the accelerating field is on, then turns off and holds zero long enough for the last emitted particle to exit the gun before changing sign. This ideal waveform is a staircase function and is given as the dotted line in Figure 53. Because this function is nonphysical it must be approximated through use of a Fourier series. Equation 55 gives the Fourier series for the whole waveform.

(55)

$$E_z(t) = E_0 \sum_{i=0}^{\infty} \frac{2((-1)^n - \cos\left(\frac{n\pi}{3}\right)}{n\pi} \sin(n\omega t)$$

Taking the first two terms in this expansion, which avoids ringing and is the simplest initial approximation, gives the temporal field profile of the proposed system, Equation 56.

(56)

$$E_z(t) = E_0 \left(-\frac{3}{\pi}\sin(\omega t) + \frac{3}{2\pi}\sin(2\omega t)\right)$$

Because E_0 is somewhat arbitrary, the magnitude of the two frequencies can be normalized to the fundamental, and the opposite sign of the fundamental field can be rewritten as a phase shift. This transforms Equation 56 into Equation 57.

(57)

$$E_z(t) = E_0 \left(\sin(\omega t - \pi) + \frac{1}{2}\sin(2\omega t)\right)$$

Using equation 57 for the fields for the 1-D simulation and a fractional gap length of 10, the back-bombardment phase range for both the fundamental only case and the fundamental and harmonic case is shown in Figure 53. This was computed using a simple Newtonian model that allowed for a first approximation of the effect of adding the harmonic frequency.

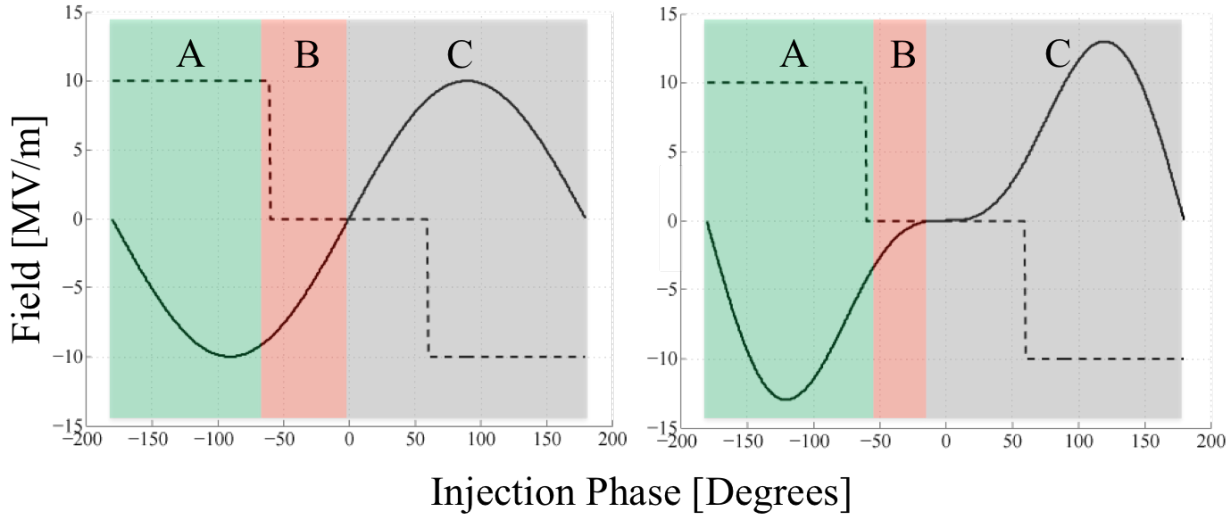

Figure 53: Left: Fundamental frequency only. Region A indicates the RF phase where particles will be accelerated out of the gun, Region B indicates the RF phase where particles back-bombard the cathode, and Region C indicates where no emission occurs because the surface field is preventing it. Right: Fundamental and second harmonic. The waveform now approximates the staircase function more closely and additionally shows the reduced size of Region B. Note: the ideal staircase field is shown with opposite polarity in order to make the graph less cluttered and thus more clear [34].

It is easy to see that the back-bombardment region denoted in Red in Figure 53 has decreased by the inclusion of the harmonic field. This shows that in principle this technique should reduce the back-bombardment power. While the full Fourier series should completely eliminate back-bombardment, the two-frequency approximation of this series is not necessarily optimized for power reduction and a different combination of phase and relative ratio may be better suited for back-bombardment mitigation; therefore, a more general equation for the two frequency fields is introduced,

(58)

$$E_z(t) = E_0 \left(\sin(\omega t) + H \sin(2\omega t + \phi_r)\right)$$

Here H is the relative strength of the harmonic field, also referred to as the harmonic field ratio, and ϕ_r is the relative phase of the harmonic field. Using the simple particle pusher model, and a 2.5 D SPIFFE simulation of a gun operating at 1.3 GHz, a fractional gap length of $\alpha = 10$, and a peak field of 10MV/m, the harmonic field ratio was varied from 0 to 2, and the relative phase was varied from 0 to 360. The back-bombardment power was computed for all cases and is shown in Figure 54 for both the 1-D simulations and the 2.5-D simulations.

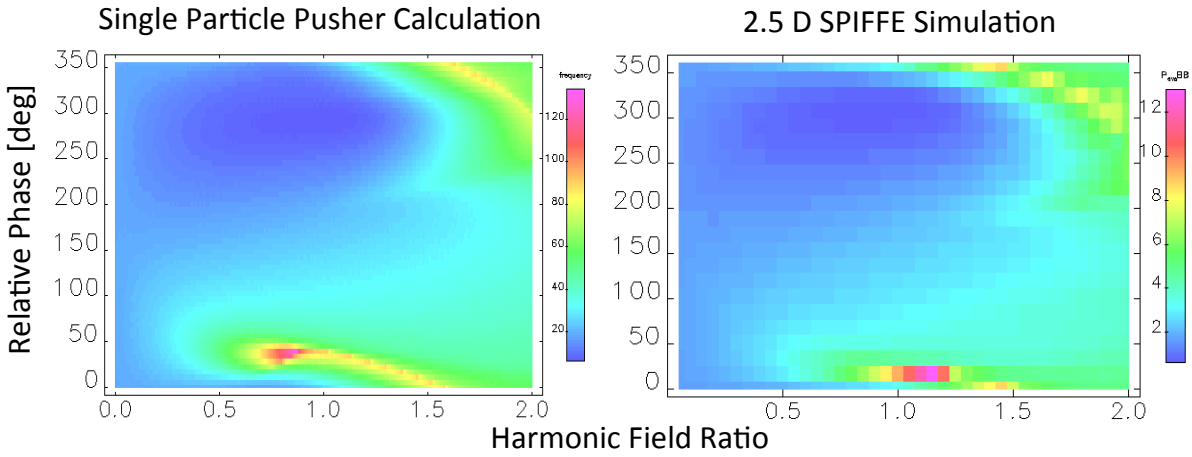

Figure 54: Comparison of 2.5-D simulations with 1-D particle pusher simulations of the two frequency gun. Both simulation runs varied the relative phase and relative magnitude of the harmonic field.

This shows that the optimal setting for the harmonic field and the relative phase is not the setting given by the Fourier series but is slightly offset in both phase and in field. While there is a well defined minimum in the back-bombardment power, if the relative phasing of the harmonic field is adjusted the back-bombardment power can increase drastically; therefore, care must be taken when operating this type of configuration to keep the harmonic field well tuned. It is also interesting to note that the 1-D simulations using the Newtonian model very closely resemble the 2.5-D particle-in-cell simulations. This indicates that the dominant process in showing how the harmonic field affects the back-bombardment is the classical Newtonian processes and the 1-D trajectory. Because the optimal set point for reducing the back-bombardment power is different than the Fourier series, it is interesting to look at the temporal field profile produced by this combination of relative ratio and phase. This is shown in Figure 55.

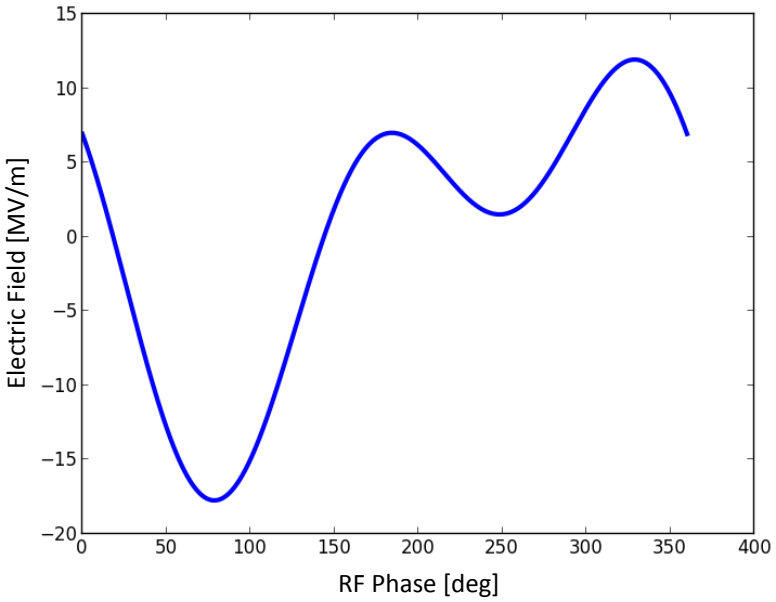

Figure 55: Temporal waveform that produces the optimal reduction in the back-bombardment power.

This shows that because of the specific relative ratio and the relative phase of the harmonic field, the peak negative field is larger than the peak positive field. While the field does not hold zero in the transition region between the positive and negative field like the approximation of the Fourier series, particles that are back-bombarded will see a lower peak field and therefore not have as much energy when returning to the cathode.

These first simulations were only for a specific case where the fractional gap length was 10. In order to get a boarder understanding of this process 1-D simulations were run with different gap lengths to look at the how back-bombardment power mitigation occurs for different gap lengths. Figure 56 shows the normalized back-bombardment power as a function of the harmonic field ratio and the relative phase for a gun with a fractional gap length equal to four.

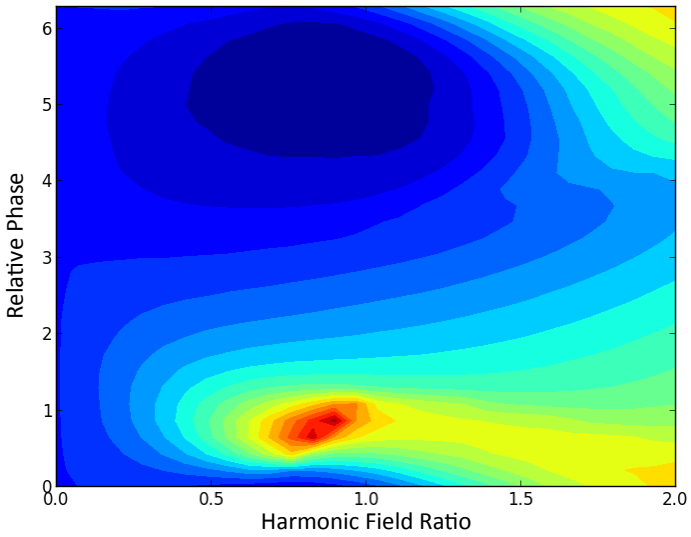

Figure 56: Back-bombardment power as a function of relative phase and harmonic field ratio for a RF frequency of 1GHz and a fractional gap length of 4.

This shows that the parameter space has the same general shape as the case shown above where the fractional gap length was 10. The minimum appears to be slightly broader and the optimum value or the field and phase is not exactly at the same place as when the fractional gap length was 10. Figure 57 shows the same results as Figure 56 however with a shorter gap length and alpha equal to eight. The important information here is the difference between Figure 57 and Figure 56. Note that the minimum is in roughly the same location in the parameter space but not exactly the same location and while the shape of the two parameter spaces is very similar, there is clearly a distortion of the contours toward a harmonic field of zero.

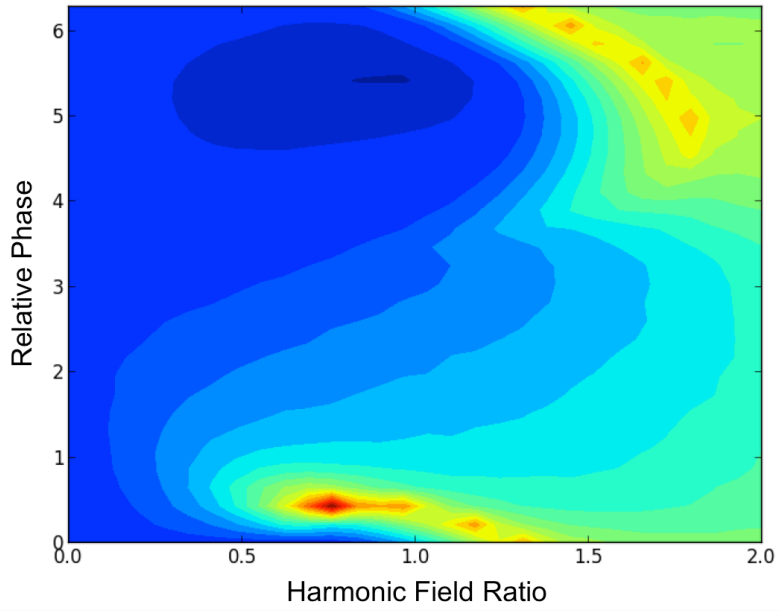

Figure 57: Back-bombardment power as a function of relative phase and harmonic field ratio for a RF frequency of 1GHz and a fractional gap length of 8

The even more extreme case is to look at a gun with a fractional gap length equal to 12. This is shown in Figure 58. This shows a similar trend as the difference between Figure 56 and 57; however, the shorter gap length has distorted the contours even further. It is interesting to note that as the gap length is shortened the minimum in the back-bombardment power is sharper. This is in contrast to the previous chapter, which showed that a shorter second cell increased the range of phases where back-bombardment would not be increased.

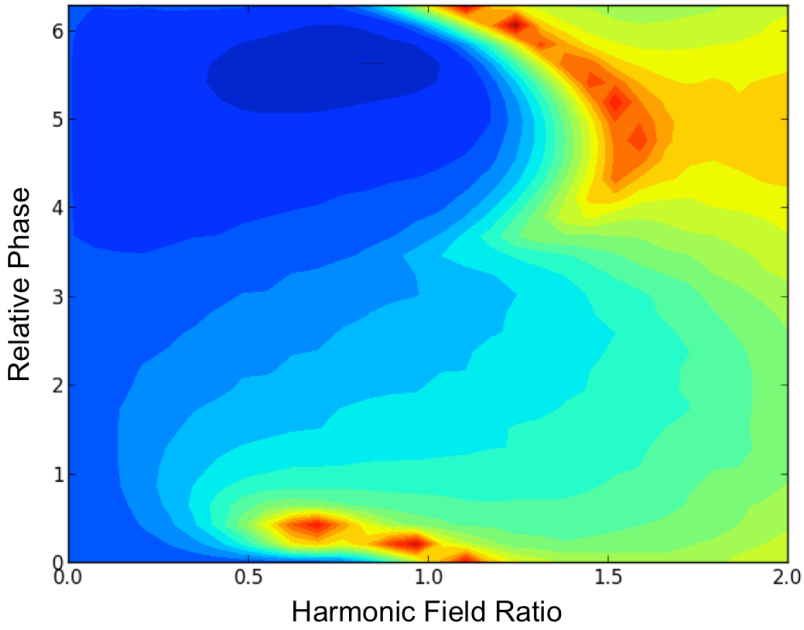

Figure 58: Back-bombardment power as a function of relative phase and harmonic field ratio for a RF frequency of 1GHz and a fractional gap length of 12

Figures 56, 57, and 58 show that the general shape of the parameter space of the harmonic field ratio and the relative phase is the same for each gap length; however, the optimum value for back-bombardment mitigation is not the same for each gap length. This indicates that the optimal setting for the harmonic field and relative phase will vary as the gun parameters are varied.

To study this, the harmonic field parameters were set to one of the optimal settings determined in previous simulations ($H = 0.90, \phi_r = 322^o$) and the fundamental operating frequency was scanned for a few values of effective gap length. This was done using the 1-D simulation technique. Figure 59 shows the percentage reduction in back-bombardment power as a function of operating frequency for five values of fractional gap length.

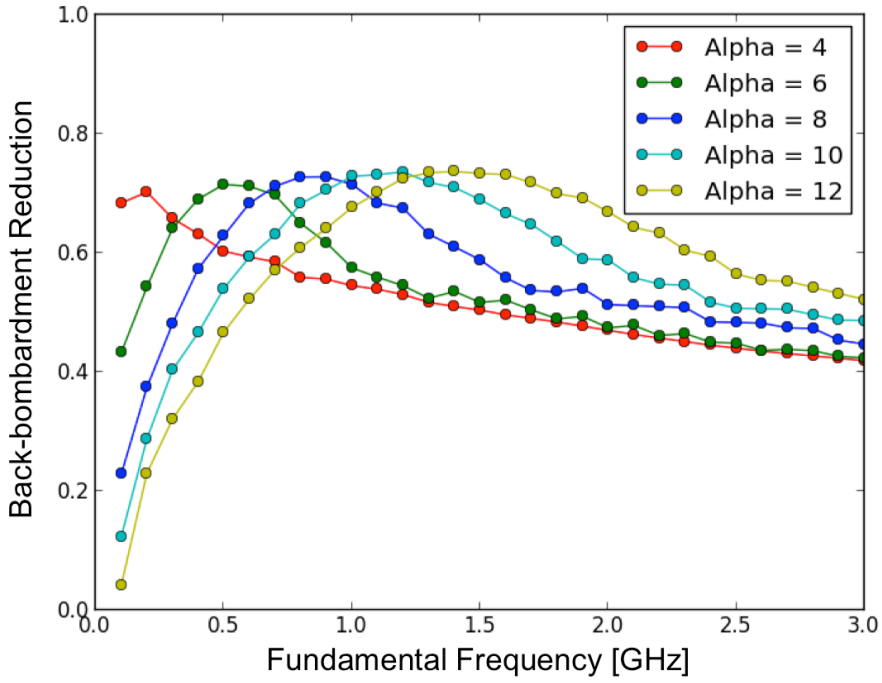

Figure 59: Back-bombardment percentage reduction as a function of the fundamental operating frequency for five values of fractional gap length.

This shows that as the gap length changes, the optimum operating frequency for the chosen harmonic field and relative phase also shifts. This confirms that for a particular frequency and gap length there will be a unique harmonic field and relative phase that optimally reduces the back-bombardment power. As the gap length is shortened the maximum in the back-bombardment reduction is broader. This is similar to the results for two cells where the shorter second gap length makes for a broader minimum in the increase in the back-bombardment power. The maximum decrease in back-bombardment power appears to be relatively constant at around 70%; however, there is even a steady increase in back-bombardment power reduction as the frequency is increased. This indicates that not only is it advantageous to run at higher frequency because of the single frequency back-bombardment power but there is a better reduction in the back-bombardment power when introducing a harmonic field with a higher

fundamental frequency. It is not immediately clear why this is happening however it has been well established that the back-bombardment decreases with an increase RF frequency. Because the harmonic frequency also increases with the increase in fundamental frequency there is likely a similar process causing the back-bombardment power to be decreased further.

5.2 Back-bombardment mitigation simulations

After studying back-bombardment mitigation through the 1-D simulations, 2.5-D simulations were used to verify the results and demonstrate the effectiveness of this technique. Additionally the beam current was varied to study in some regards how space-charge impacts the effectiveness of the harmonic frequency for back-bombardment mitigation. These simulations were performed on the short gap gun with an alpha of 10. For these simulations the frequency was varied while keeping the charge emitted per RF period constant. This translates to an increase in the beam current with frequency. Additionally these simulations were run for both the harmonic field off and with the harmonic field on for a set value of the relative phase and harmonic field ratio. Figure 60 shows the back-bombardment power as a function of frequency with both the harmonic field on and the harmonic field off. It also shows the percentage reduction in back-bombardment power as a function of frequency.

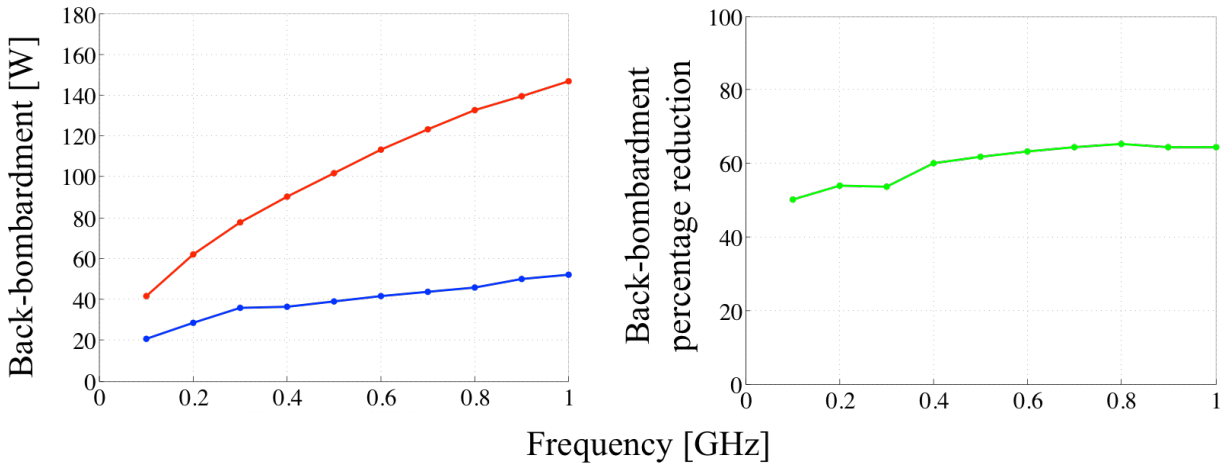

Figure 60: Left (Back-bombardment power as a function of frequency with harmonic field off (red) and harmonic field on (blue). Right: Percentage reduction in the back-bombardment power. Simulations were run with constant bunch charge [34].

This shows that as the baseline back-bombardment increases due to the increase in the beam current the reduced back-bombardment also increases. This indicates that as the back-bombardment power is reduced by some fairly regular percentage, shown by the right side of Figure 60. The average reduction in the back-bombardment power for these simulations is 60%. However, there is a slope to the back-bombardment reduction percentage as a function of frequency. Additionally the previous section showed that the optimum harmonic field and phase would vary with the gun parameters. If optimization methods were used in conjunction with the simulation code to find the harmonic field ratio and relative phase for each frequency, it is likely the maximum reduction in back-bombardment would more closely resemble the 70% seen in Figure 59. Furthermore, because the beam current is changing with frequency due to the constant bunch charge for simulations, it is possible that space-charge forces are limiting the ability of the harmonic field to reduce the back-bombardment power. In order to examine how space-charge impacts the ability of the harmonic field to mitigate back-bombardment more closely, the relative phase and harmonic field ratio were varied for three frequencies and three values of bunch

charge. The result of this scan is shown in Figure 61. Due to these simulations being computationally intensive, the parameter scan shown is fairly coarse.

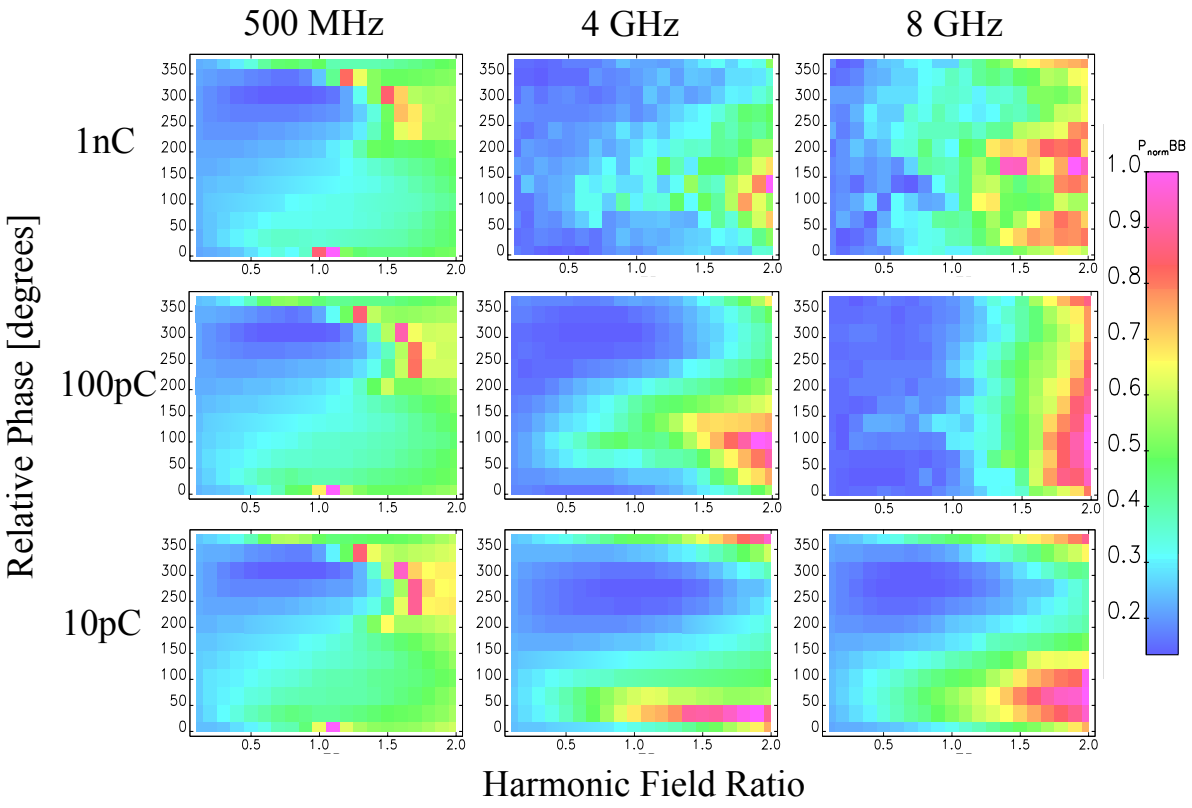

Figure 61: Back-bombardment mitigation simulations for different bunch charges and frequencies. The back-bombardment power for each plot was normalized to the peak its respective peak. As the gun transitions from the bottom left to the top right, the space-charge forces are increasing significantly and the gun becomes space-charge limited [34].

This shows that as the space-charge forces become more prominent, the ability for the harmonic frequency to reduce the back-bombardment power deteriorates significantly. The parameter space begins by looking very similar to that shown in Figure 54 to a more distorted parameter space as the space-charge increases. Once the gun has transitioned fully into the space-charge regime the parameter space is noisy and there is no minimum in the back-bombardment power. This indicates that for very high currents the space-charge forces will dominate over the

harmonic frequency and the back-bombardment process cannot be mitigated [34]. This chapter has shown how the harmonic field can be used to reduce the back-bombardment power by up to 70% in some cases, but this ability is greatly reduced in the presence of significant space-charge forces. However significant space-charge forces also leads to a decrease in the output current and becomes impractical for real world applications.

6. Conclusions

In conclusion, this dissertation was able to address each area of interest outlined in the introduction and shed new light on the back-bombardment process in thermionic cathode RF guns.

The first area of interest was that simple analytic models could be derived to predict how back-bombardment power varies as a function of the design parameters in single cell guns. In addition these models achieve better than order of magnitude accuracy when compared with simulation. Through the use of simplifications this was successful and the analytic model was compared with simulations. These comparisons showed that indeed the back-bombardment can be calculated to better than an order of magnitude using Equation 24. Equation 59 gives v_{eff}, and Equation 60 gives the general form of K.

(59)

$$v_{eff} = c\sqrt{1-\left(1+\frac{qE_0\lambda}{2m_0c^2\alpha}\right)^{-2}}$$

(60)

$$K = \frac{\int_0^{L_{gap}} E(z)dz}{E_0\lambda/\alpha}$$

Comparison with simulation showed that this model accurately predicts how back-bombardment varies as a function of the gun parameters. Additionally comparison with measured data produced an estimate to within a factor of 2 of the measured value. These results provide a new tool that can be used to assess the impact of back-bombardment on the initial design stages without the need to run beam simulations.

The second area of interest was to show that simple models could be used to estimate the space-charge fields acting on the beam and predict exactly how these forces will impact the back-bombardment process. It was shown that the longitudinal space-charge field calculated by Equation 46 would decrease the effective accelerating field acting on the back-bombarded beam. Additionally the space-charge defocusing will decrease the effective area over which the back-bombarded beam deposits its energy. This scaling, given by Equation 48, can be computed using Equation 47 and then be applied to the back-bombardment power equation. Including the space-charge field given by Equation 46 and the scaling given by Equation 48, a more complete picture of the back-bombardment power that includes the effects of space-charge was derived. When compared with simulation this result was shown to predict the general behavior of the back-bombardment process and shed light on the specific details of why the back-bombardment power behaves the way it does under the influence of space-charge forces. The inclusion of these effects gives the complete equation for back-bombardment power in single cell guns as a function of all the relevant beam parameters, Equation 49.

The third area of interest was to study how the back-bombardment process was impacted by the introduction of more than one cell. In many applications multiple cells are used to increase the accelerating power of the gun and therefore this addition was needed to generate a more complete picture of back-bombardment in practical applications. This was studied through extensive 1-D and 2.5-D simulations of multi-cell guns. These simulations showed that the back-bombardment power is fundamentally limited by the back-bombardment power due to the first accelerating cell. However, 2-Cell designs exist where the second cell is independently powered and independently phased to not further increase the back-bombardment from the 1-Cell case.

These designs may have advantageous consequences for the output beam dynamics and should be considered when designing a RF thermionic cathode gun system.

The last are of interest was to study how back-bombardment could be mitigated through the introduction of a harmonic field that changes the temporal field profile. This was studied extensively through both 1-D and 2.5-D simulations. These simulation studies showed that an optimum harmonic field and relative phase reduce the back-bombardment power by up to 75%. Additionally, simulation studies showed that the optimal operating point for the harmonic field varies depending on the fundamental frequency and the gap length. Simulations were also performed that show the effects of space-charge on the ability for the harmonic field to mitigate back-bombardment. This showed that as space-charge begins to become more and more prevalent it dominates over the effect of the harmonic frequency and there is no compensation for the back-bombardment process.

This dissertation has shed new light on the fundamental physics of the back-bombardment process and provided useful design tools for designing these types of guns. The equations derived here can be used to optimize initial gun design and examine the trade space before running detailed simulations. Additionally the equations derived here can be used to develop a multi-physics model of the back-bombardment process that shows how the surface temperature of the cathode and consequently the output current will increase over time. These models could be used to predict the run-away condition that occurs and would provide the tools necessary to evaluate the limitations of this type of system. This dissertation also showed that a 2-cell design could be tuned to not increase the back-bombardment power. This would be potentially useful

because the second cell could increase the average energy of the beam leaving the gun and could also provide compensation to the longitudinal phase space. The output beam was not studied in this dissertation but this work would be a good area to move into for designing a practical system. The design tools developed in this dissertation will be highly useful to the development of these guns and as such significantly contributes to the field of accelerator physics.

References

[1] J. Andruszkow et al. *First Observation of Self-Amplified Spontaneous Emission in a Free-Electron Laser at 109 nm Wavelength Phys*. Rev. Lett. 85, 3825-3829 (2000)

[2] EXFEL http://www.xfel.eu/

[3] F. Sanibale et al., Proceedings FEL conference, Nara, August 2012, Jacow http://www.lbl.gov/publicinfo/newscenter/tabl/2010/february/02-26-10/index.html

[4] M.E. Courpie et al. The LUNEX5 project ,Proceeding FEL conf. Nara, Aug. 2012

[5] See for example, H. Iijima, C. Shonaka, M. Kuriki, D. Kubo, and Y. Masumoto. *A Study of Lifetime of NEA-GaAs Photocathode at Various Temperatures* IPAC Proceedings (2010)

[6] See for example, J Grames et. al *Measurements of Photocathode Operational Time at Beam Currents up to 10 mA using an improved DC High Voltage GaAs Photogun* American Institute of Physics, 978-0-7354-0423-6/07

[7] See for example, C. A. Marques and C. C. Motta. Microwave and Optoelectronics Conference, IMOC. Proceedings of the SBMO/IEEE MTT-S International (Volume 2), 2003

[8] Karl R. Spangenberg. *Vacuum Tubes* McGraw-Hill Electrical and Electronic Engineering Series, 1948

[9] J.R. Harris and P.G. Oshea. IEEE Transactions Electronic Devices 53. 2824-2829. (2006)

[10] H.P. Bluem, D. Dowell, A.M.M. Todd and L.M. Young. *High Brightness Thermionic Electron Gun Performance* 2011 Proceedings of ERL2011 Tsukuba, Japan

[11] Y.-E Sun, J. W. Lewellen, and D.W. Feldman. *Photothermal Cathode Measurements at the Advanced Photon Source*. Proceedings of LINAC 2006, Knoxville, Tennessee USA.

[12] M. Borland et al *Pulsed Laser Heating of Thermionic Cathodes in RF Guns* LINAC 2010

[13] See for example, N.D. Arnold et al. Nuclear Instruments and Methods in Physics Research. A 475 28–37, (2001)

[14] C.B. McKee et al., *Computer Simulations of Cathode Heating by Back-Bombardment in the Microwave Electron Gun* Nuclear Instruments and Methods in Physics Research A 296 717-719, (1990)

[15] Toshiteru Kii et al. *Evaluation of Thermal Effects Due to Back-Streaming Electrons in the IAE RF Gun,* NIM A 483 (2002) 310–314

[16] Toshiteru Kii et al. *Experiment and Analysis on Back-Bombardment Effect in Thermionic RF Gun,* NIM A 475 (2001) 588–592

[17] See for example, K. Masuda et al., *Transient beam loading effects due to back-streaming electrons onto a thermionic cathode in an RF gun* Nuclear Instruments and Methods in Physics Research A 483 315-320, (2002)

[18] See for example, H. Zen et al., *Beam Energy Compensation in a Thermionic RF Gun by Cavity Detuning*, IEEE Trans. Nucl. Sci. 56 (2009) 1487-1491

[19] Zhou Xu et al. *Theoretical Study on the Transient Process in a Microwave Gun With a Thermionic Cathode* NIM A 407 (1998) 53-56

[20] M. Borland *A High Brightness Thermionic Microwave Electron Gun*, SLAC-402 UC-414 (A)

[21] Y Huang and J. Xie *Measures to Alleviate the Back Bombardment Effect of Thermionic RF Electron Gun* IEEE 0-7803-0135-8/91

[22] Y. Kim et al., *Commissioning of S-Band RF Gun and LINAC for the Mark-III FEL Facility at Duke University* Proc. FEL2006, pp. 411-414.

[23] Hongxiu Liu*, Simulation Studies on Back Bombardment of Electrons in RF Thermionic Guns,* NIM A302 (1991) 535-546

[24] H. Hama et al *3-D Simulation Study for a Thermionic RF Gun Using an FDTD Method,* NIM A 528 (2004) 371–377

[25] T. Kii, et al. *Reducing Back-Bombardment Effects Using Thermionic Cathode In IAE RF Gun.* Proceedings of the 2004 FEL Conference, 443-446

[26] Toshiteru Kii et al. *Improvement of Electron Beam Properties by Reducing Back-Bombardment Effects in a Thermionic RF Gun,* NIM A 507 (2003) 340–344

[27] Sanghyun Park, *Thermionic RF Gun and LINAC Pre-Injector for SPEAR3,* Proceedings of LINAC2002, Gyeongju, Korea

[28] C.B. McKee, and John M.J. Madey *Optimization of a Thermionic Microwave Electron Gun*, NIM A304 (1991) 386-391

[29] V.A. Kushnir et al. *Simulations of Beam Performances of the Two-Cell RF Gun,* EPAC 1996

[30] E. Tanabe et al. *A Novel Structure of Multi-Purpose RF Gun*, LINAC 1998

[31] B. Anderberg et al *A New 3 GHz RF Gun Structure For MAX-Lab,* EPAC 2000, Vienna, Austria

[32] V.A. Kushnir, *High Frequency Electron Guns: Current Status,* NSC KIPT, Kharkov, Ukraine

[33] J.M.D. Kowalczyk et al. *Laser Cooling to Counteract Back-Bombardment Heating in Microwave Thermionic RF Guns*, FEL2013, New York, NY, USA

[34] J. Edelen et al, *Electron Back-bombardment and mitigation in a short gap thermionic cathode RF Gun* IEEE Transactions in Nuclear Science, Volume 61 Issue 2

[35] M. Borland. *SPIFFE (Space-charge and Integration of Forces For Electrons)* Argonne National Lab
http://www.aps.anl.gov/Accelerator_Systems_Division/Accelerator_Operations_Physics/manuals/spiffe_V3.2/

[36] J. Billen. *Poisson Superfish Codes*, Los Alamos National Laboratory, Copyright 1985-2005

[37] K. Wille, The Physics of Particle Accelerators an Introduction (Oxford University Press, New York, 2000)

[38] S. Biedron, J.W. Lewellen, and J. Noonan. Private Communication to the High Energy Laser Joint Technology Office. December 2005

[39] J. Edelen, S. Biedron, J. Harris, S. Milton, and J.W. Lewellen. *A Two Frequency Gun for High Current Thermionic Injector Systems*, Proceedings of the 2013 NA-PAC

[40] Kwang-Je Kim, *RF and Space-charge Effects in Laser Driven RF Electron Guns* Nuclear Instruments and Methods in Physics Research A275 (1987) 201-208

[41] J.W. Lewellen *Energy Spread Compensation of a Thermionic Cathode RF Gun.* Proceedings of the 2003 PAC.

[42] J. P. Edelen et al, *Theory and simulation of backbombardment in single-cell thermionic-cathode electron guns,* Physical Review Special Topics – Accelerators and Beams (Volume 18 – Issue 4), April 2015

[43] J. P. Edelen et al, *An improved analytical model of electron back-bombardment in thermionic-cathode RF guns,* Proceedings of the 2015 IPAC